Experimental investigation of oscillations in space plasma thrusters via data-driven analysis techniques

by

Davide Maddaloni

A dissertation submitted in partial fulfillment of the requirements for the degree of Doctor of Philosophy in

PhD program in Aerospace Engineering

Universidad Carlos III de Madrid

Advisor(s):

Mario Merino
Filippo Terragni

Tutor:

Mario Merino

November 2024

A mia madre, a mio padre, ed a mio fratello.

ACKNOWLEDGEMENTS

First of all, I would like to express my gratitude to my supervisors, Mario Merino and Filippo Terragni, for rendering this thesis possible, and for their mentorship throughout these four years. Secondly, I would like to thank Jaume, for being a guide in the lab, and Adriàn, for the invaluable work with HYPHEN. Finally, I want to express my gratitude to Eduardo and Pablo for leading the EP2 research group.

I also would like to thank Victor Désangles and Federico Boni for welcoming me during my three months in Palaiseau. Thank you for devoting so much of your time to all the work behind the scenes that was required for me to be there and to perform our research activities; Chapter 4 of this thesis would not have been possible without you. My deepest gratitude to all the researchers of the DPHY group at ONERA for the warm welcome during my three months in Palaiseau. I never felt out of place.

My sincere gratitude goes also to Andrea Ianiro and Stefano Discetti, without whom I possibly wouldn't even be here to begin with. Grazie mille per aver accolto me e Iacopo in quel lontano ottobre del 2019, seppur con qualche riserbo. Grazie per averci guidato con mano mentre facevamo i nostri primi passi nell'ambito della ricerca. Grazie Andrea per esserti fidato di me, te ne sono estremamente riconoscente.

A seguire, grazie anche al miglior coinquilino del decennio, Iacopo. Dopo quasi ben dieci anni, magari questa è l'opportunità migliore per ringraziarti. Ci conosciamo dal 2013, fa strano a pensarci. Dopo quel giorno, in un modo o nell'altro ti ho sempre avuto attorno, sia in casa che all'università, sia a Napoli che a Madrid. Sei un collega prezioso, un caro amico e un coinquilino premuroso. Spero di poter condividere di nuovo un appartamento (o una intera residenza universitaria) con te in futuro, chissà.

Mil gracias a todos mis colegas del departamento para hacer el despacho un lugar más feliz. Thanks to Diego and Célian and, for some time, Matteo 2 for literally bearing with me every single day, every single hour. Thanks to Marco, Matteo 1, Davide (2), Simone, Alberto 1, Alberto 2, Borja, Tatiana, Andrés, Guillermo, for bearing with me mostly only at lunch. Leganés habría sido un lugar mucho peor sin nuestras conversaciones durante las comidas. And on top of that, thanks for bearing with me so many times also outside of the workplace, even though at this point I suspect you enjoyed my company, at the end of the day.

And thanks to Diego, Matteo 1, Matteo 2, Davide (2), Simone, Qihong, Marco, Giuseppe, Gianni, Natasha (I can't write that s with the hat), Yuma, Olympia, Luigi, Pablo (2) and Alicia, for the precious moments spent playing games together. I look forward to playing more games with (some of, not all games can be played with this many people) you. Muchas gracias Pablo (1), para ser mi compañero de viaje, de baile, de ténis, y de comidas. Ultimately, I wish I could thank personally every single person that played a role, as minor as it can be, during these four years of my life, many of whom I gradually lost touch with. Thanks to all of you.

Thanks to Paridhi, my other half. You have been such an invaluable part of this journey, that I could never be done thanking you for it. You manage to be as supportive as you possibly can whether you are here or not. As small as you may look, you have been carrying me on your shoulders relentlessly for so long now, and it is only fair to say that a big piece of this is thanks to you. Part of the person that I am today is your doing, and I owe you so much.

Dulcis in fundo, grazie ai miei genitori. Grazie di essere sempre stati i migliori genitori che potessi desiderare, da molto prima che iniziassi questo percorso. È quasi superfluo dire che senza di voi non sarei qui, ma è molto più vero di quel che possa sembrare. Il vostro supporto e rispetto per le mie scelte è stato uno scoglio inamovibile che mi ha permesso di raggiungere questo punto con la tranquillità che avete sempre lottato per farmi avere. Grazie a mio fratello, perchè essere mio fratello è difficile. Ciononostante, non hai mai mollato, e spero tu non lo faccia mai. Sei molto più simile a me di quanto credi.

Alla prossima,

Davide

This work has been funded by:

- the Madrid Government (Comunidad de Madrid) under the Multiannual Agreement with UC3M in the line of Fostering Young Doctors Research (MARETERRA-CM-UC3M), and in the context of the V PRICIT (Regional Programme of Research and Technological Innovation).
- the European Research Council (ERC) under the European Unions Horizon 2020 research and innovation programme (Starting Grant ZARATHUSTRA, grant agreement No 950466).

PUBLISHED AND SUBMITTED CONTENT

Journal papers:

- **Maddaloni D.**, Domínguez-Vázquez A., Terragni F., Merino M., "Data-driven analysis of oscillations in Hall thruster simulations". Plasma Sources Science and Technology. 2022, May 3; 31(4):045026. Doi: 10.1088/1361-6595/ac6444 (included in Chapter 2).
- **Maddaloni D.**, Bayón-Buján B., Navarro-Cavallé J., Terragni F., Merino M., "Experimental characterization of low-frequency fluctuations in the magnetic nozzle of a Helicon Plasma Thruster". Plasma Sources Science and Technology. (submitted) (included in Chapter 3)

Conference papers:

- **Maddaloni D.**, Domínguez-Vázquez A., Merino M., Terragni F., "Data-driven analysis of breathing mode and ion-transit mode in 2D hybrid Hall thruster simulations". In AIAA Propulsion and Energy 2021 Forum, p. 3398. August 9-11, 2021, Online event. Doi: 10.2514/6.2021-3398.
- **Maddaloni D.**, Boni F., Désangles V., Bayón-Buján B., Merino M., Terragni F., "Experimental characterization of oscillations in the Magnetic Nozzle of an Electron Cyclotron Resonance Thruster". In 38th International Electric Propulsion Conference (IEPC-2024). June 23-28, 2024, Toulouse, France (included in Chapter 4).

Datasets:

- **Maddaloni D.**, Domínguez-Vázquez A., Terragni F., Merino M, "Data from: Data-driven analysis of oscillations in Hall thruster simulations". Zenodo. 2022, March 24. Doi: https://doi.org/10.5281/zenodo.6390700.

OTHER RESEARCH MERITS

- **Maddaloni D.**, Domínguez-Vázquez A., Merino M., Terragni F., "Data-driven analysis of breathing and ion-transit modes in 2D hybrid Hall thruster simulations". In ExB Plasmas Workshop 2022, Poster session. February 16-18, 2022, Online event.

- Merino M., Navarro-Cavallé J., Fajardo-Pena P., Inchingolo M., Jiménez P., Zhou J., García-Lahuerta D., Boyé C., **Maddaloni D.**, Terragni F., Ahedo E., "Electrodeless plasma thrusters and magnetized plasma expansions for space propulsion". In APS Annual Gaseous Electronics Meeting Abstracts 2022 (pp. EM2-007). October 3-7, 2022, Sendai, Japan.

- **Maddaloni D.**, Navarro-Cavallé J., Merino M., Terragni F., "Experimental investigation of oscillations in a magnetic nozzle". In 35th International Conference on Phenomena in Ionized Gases (ICPIG 2023). July 9-14, 2023, Egmond aan Zee, The Netherlands.

- Merino M., **Maddaloni D.**, Bayón-Buján B., Terragni F., Navarro-Cavallé J., "Data-driven analysis techniques for plasma space propulsion experiments and simulations". In International Conference on Research and Applications of Plasmas (PLASMA 2023). September 18-22, 2023, Warsaw, Poland.

- Merino M., **Maddaloni D.**, Ripoli M., Navarro-Cavallé J., Terragni F., Ahedo E., "Oscillations and instabilities in a propulsive magnetic nozzle". In APS Annual Gaseous Electronics Meeting Abstracts 2023 (pp. HR2-005). October 9-13, 2023, Ann Arbor, MI.

CONTENTS

LIST OF FIGURES

LIST OF TABLES

ABSTRACT

The main objective of this thesis is to contribute to the overall understanding of plasma oscillations taking place in devices employed for space propulsion. Oscillations are known to affect thruster performances by impacting particle cross-field transport and energy, for which reason the study of such phenomena is recently receiving increased attention by the community. To achieve this goal, appropriate data-driven algorithms are applied to data stemming from both numerical simulations and experiments. A data-driven approach, while still requiring expert knowledge for effective application, has the advantage of reducing the dependency upon a priori-assumptions, reducing in turn researcher bias and aiding the detection of features hidden within the data. However, data-driven techniques generally necessitate large amounts of data, something that became more accessible with the latest technological advancements of the last decades. In this thesis, data related to various thrusters employing different technologies are analyzed.

The first part of the thesis focuses on Hall Effect Thrusters (HETs), a mature technology that has been flying in space since the '70s. However, the physics of HETs is still to this day subject to extensive studies, mainly due to the open problem of anomalous transport. Simulation data for a representative HET plasma computed by a two-dimensional hybrid particle-in-cell/fluid code are postprocessed by means of both Proper Orthogonal Decomposition (POD) and Higher Order Dynamical Mode Decomposition (HODMD). The analysis detects two notorious axial oscillations taking place in this device, namely the breathing mode and the ion transit time (ITT) dynamics, interacting with each other. It is stressed how POD is unable to uncouple the two oscillations due to mode interplay, whereas HODMD successfully manages to handle this task. The two dynamics are reconstructed separately, and their different spatial structure and underlying mechanisms are highlighted. Results for both the breathing and ITT modes agree well with existing theories, with the former displaying a predominant standing wave structure, while the latter possesses a traveling structure, propagating downstream.

The subsequent chapters move onto the study of oscillations in newer technologies, namely Electrodeless Plasma Thrusters, for which the study of plasma oscillations is much less explored. These types of devices promise extended longevity and lower sensibility to the employed propellant, but their technological readiness level is still low with respect to other classical alternatives. It is expected that advancing the understanding of their physics may ultimately lead to an enhancement of their performance and overall efficiency. The two devices experimentally investigated in this thesis are the novel Helicon Plasma Thruster (HPT) and Electron Cyclotron Resonance Thruster (ECRT), both of them employing a Magnetic Nozzle (MN) to guide the expanding plasma.

Experimental campaigns performed on a prototype of HPT using Langmuir probes (LPs) allow to characterize oscillations $\leq$ 1 MHz taking place within the plume of this

device. Multiple LPs are employed to reconstruct the wavevector in space of the identified waves by using an adaptation of the Two-Points Power Spectral Density (PSD2P) technique. Additionally, coherence analysis and bi-coherence analysis are applied to infer the statistical significance of the observed oscillations and the level of quadratic non-linear interaction intrinsic to the data, respectively. The study detects a very-low frequency, explained by means of a breathing-like ionization-instability, and another, more broadband oscillation displaying azimuthal propagation, attributed to a parametric-decay instability.

A similar setup is used to collect data of oscillations between 5–100 kHz in the MN of an ECRT. An array of LPs is employed once again to reconstruct the wavevector in space, alongside a Curling Probe, collecting time-resolved measurements of the electron density, and a high-speed camera, recording the light emitted by the plasma in the source. The study similarly employs a combination of the PSD2P technique, coherence and bi-coherence analyses to postprocess the LP data, while also using POD to postprocess the data of the high-speed camera. The study allows to perform a complete characterization of the two oscillations observed, a low-frequency one, which is similarly attributed to an ionization mode, and another at a higher frequency, whose characterization is attempted according to recent literature.

RESUMEN

El objetivo principal de esta tesis es contribuir a la comprensión general de las oscilaciones de plasma que ocurren en dispositivos utilizados para la propulsión espacial. Es sabido que las oscilaciones afectan el rendimiento de los propulsores al impactar el transporte de partículas a través del campo magnético y su energía, por lo cual el estudio de dichos fenómenos está recibiendo una mayor atención por parte de la comunidad recientemente. Para lograr este propósito, se aplican algoritmos adecuados de tipo data-driven a datos provenientes tanto de simulaciones númericas como de experimentos. Un enfoque de tipo data-driven, aunque aún requiere conocimiento experto para ser aplicado de manera efectiva, ofrece la ventaja de reducir la dependencia por hipótesis restrictivas apriorísticas, permitiendo a su vez reducir el sesgo del investigador y ayudando a detectar características ocultas en los datos. Sin embargo, la técnicas data-driven necesitan grandes cantidades de datos, algo que se ha vuelto más acesible con los últimos avances tecnológicos de las últimas décadas. En esta tésis, se analizan datos relacionados con varios propulsores que emplean diferentes tecnologías.

La primera parte de la tesis se centra en Propulsores de Efecto Hall (HETs), una tecnología madura que ha estado en uso en el espacio desde los años 70. No obstante, la física de los HETs sigue siendo objeto de estudios extensivos hasta el día de hoy, principalmente debido al problema abierto del transporte anómalo. Los datos de simulación para un plasma representativo de HET, calculados mediante un código híbrido bidimensional de partículas en celda/fluido, se posprocesan a través de Descomposición Ortogonal Proper (POD) y Descomposición de Modos Dinámicos de Orden Superior (HODMD). El análisis detecta dos notorias oscilaciones axiales que ocurren en esto dispósitivo, concretamente el modo de respiración y el modo de tiempo de tránsito iónico (ITT), los cuales interactúan entre sí. Se enfatiza cómo la POD es incapaz de desacoplar las dos oscilaciones debido a su interacción, mientras que la HODMD logra manejar esta tarea con éxito. Las dos dinámicas se reconstruyen por separado, y se resaltan sus diferentes estructuras espaciales y mecanismos subyacentes. Los resultados para ambos modos, el de respiración y ITT, concuerdan bien con las teorías existentes, mostrando el primero una estructura predominante de onda estacionaria, mientras que el segundo posee una estructura viajera, propagándose río abajo.

Los capítulos siguientes pasan al estudio de las oscilaciones en tecnologías mas novedosas, especificamente los Propulsores de Plasma sin Electrodos, para los cuales el estudio de las oscilaciones de plasma está mucho menos explorado. Estos típos de dispositivos prometen una logevidad extendida y una menor sensibilidad a los propelentes utilizados, aunque su nivel de preparación tecnológica todavía se encuentra por debajo de otras alternativas clásicas. Se estima que avanzar en la comprensión de sus física pueda finalmente llevar a mejoras en sus rendimientos y eficiencias. Los dos dispositivos investigados de

manera experimental en esta tésis son el innovador Propulsor de Plasma Helicoidal (HPT) y el Propulsor de Resonancia de Ciclotrón Electrónico (ECRT), ambos utilizando una Tobera Magnética (MN) para guiar el plasma en expansión.

Campañas experimentales realizadas con un prototipo de HPT utilizando sondas de Langmuir (LPs) permiten caracterizar oscilaciones $\leq$ 1 MHz que tienen lugar en la pluma de este dispositivo. Se emplean múltiples LPs para reconstruir el vector de onda en el espacio de las oscilaciones identificadas mediante una adaptación de la técnica de Densidad Espectral de Potencia de Dos Puntos (PSD2P). Además, se emplean análisis de coherencia y bi-coherencia para evaluar la significancia estadística de las fluctuaciones observadas y el nível de interacción cuadrática no lineal intrínseco en los datos, respectivamente. El estudio detecta una oscilación de frecuencia muy baja, explicada mediante una inestabilidad de ionización similar a una de respiración, y otra oscilación de banda ancha que muestra propagación azimutal, atribuida a una inestabilidad de decaimiento paramétrico.

Un montaje similar se utiliza para recopilar datos de oscilaciones entre 5–100 kHz en la MN de un ECRT. Se emplea nuevamente una matriz de LPs para reconstruir el vector de números de onda en el espacio, junto con una Sonda de Curling, que recopila mediciones de densidad electrónica con resolución temporal, y una cámara de alta velocidad, que registra la luz emitida por el plasma en la fuente. El estudio emplea de manera similar una combinación de la técnica PSD2P, análisis de coherencia y bi-coherencia para posprocesar los datos de las LPs, mientras que la POD se utiliza para el procesamiento de los datos de la cámara de alta velocidad. El estudio permite realizar una caracterización completa de las dos oscilaciones observadas, es decir una de baja frecuencia, que se atribuye de manera similar a un modo de ionización, y otra a una frecuencia más alta, cuya caracterización se intenta de acuerdo con la literatura reciente.

RIASSUNTO

Il principale obiettivo di questa tesi è contribuire alla comprensione generale delle oscillazioni del plasma che si verificano nei dispositivi utilizzati per la propulsione spaziale. È noto che le oscillazioni influenzano le prestazioni dei propulsori, impattando il trasporto delle particelle attraverso il campo magnetico e la loro energia, motivo per cui lo studio di tali fenomeni ha di recente ricevuto una crescente attenzione dalla comunità. Per raggiungere questo scopo, vengono applicati algoritmi adeguati di tipo data-driven ai dati provenienti sia da simulazioni numeriche che da esperimenti. Un approccio data-driven, nonostante richieda ancora conoscenze esperte per essere applicato efficacemente, offre il vantaggio di ridurre la dipendenza da restrittive ipotesi aprioristiche, riducendo a sua volta il bias dell'investigatore e aiutando a individuare caratteristiche nascoste nei dati. Tuttavia, le tecniche data-driven necessitano di una grande quantità di dati, cosa che è diventata più accessibile grazie ai progressi tecnologici più recenti delle ultime decadi. In questa tesi vengono analizzati diversi propulsori che utilizzano tecnologie differenti.

La prima parte della tesi si concentra sui Propulsori a Effetto Hall (HETs), una tecnologia matura utilizzata nello spazio dagli anni '70. Tuttavia, la fisica degli HET è ancora oggi oggetto di studi approfonditi, principalmente a causa del problema aperto del trasporto anomalo. I dati di simulazioni per un plasma rappresentativo di HET, calcolati mediante un codice ibrido bidimensionale di particelle in cella/fluido, vengono postprocessati tramite Decomposizione Ortogonale Propria (POD) e Decomposizione dei Modi Dinamici di Ordine Superiore (HODMD). L'analisi rileva due note oscillazioni assiali che si verificano in questo dispositivo, ossia il modo di respirazione e il modo di tempo di transito ionico, i quali interagiscono tra loro. Si sottolinea come la POD non riesca a disaccoppiare queste due dinamiche a causa della loro interazione, mentre la HODMD riesce a gestire con successo questo compito. Le due dinamiche vengono ricostruite separatamente, e si evidenziano le loro diverse strutture spaziali e meccanismi sottostanti. I risultati per entrambi i modi, quello di respirazione e quello ITT, concordano con le teorie esistenti, con il primo che mostra una predominante struttura d'onda stazionaria, mentre il secondo possiede una struttura itinerante che si propaga verso valle.

I capitoli successivi si spostano allo studio delle oscillazioni in tecnologie più recenti, in particolare i Propulsori a Plasma senza Elettrodi, per i quali lo studio delle oscillazioni del plasma è molto meno esplorato. Questi tipi di dispositivi promettono una maggiore longevità e una minore suscettibilità dai propellenti utilizzati, anche se il loro livello di preparazione tecnologica è ancora inferiore rispetto ad altre alternative classiche. Si stima che il progredire nella comprensione della loro fisica possa portare infine a miglioramenti delle loro prestazioni e efficienze. I due dispositivi investigati sperimentalmente in questa tesi sono l'innovativo Propulsore a Plasma Elicoidale (HPT) e il Propulsore a Resonanza di Ciclotrone Elettronico (ECRT), entrambi i quali utilizzano un Ugello Magnetico (MN)

per guidare il plasma in espansione.

Campagne sperimentali condotte con un prototipo di HPT utilizzando sonde di Langmuir (LPs) permettono di caratterizzare oscillazioni ≤ 1 MHz che si verificano nel getto di questo dispositivo. Vengono impiegate varie LPs per ricostruire il vettore d'onda nello spazio delle oscillazioni identificate mediante un adattamento della tecnica di Densità Spettrale di Potenza a Due Punti (PSD2P). Inoltre, si impiegano analisi di coerenza e bi-coerenza per valutare la significatività statistica delle fluttuazioni osservate e il livello di interazione quadratica non lineare intrinseca nei dati, rispettivamente. Lo studio rileva un'oscillazione a frequenza molto bassa, spiegata tramite un'instabilità di ionizzazione simile al quella di respirazione, e un'altra oscillazione a banda larga che mostra propagazione azimutale, attribuita a un'instabilità di decadimento parametrico.

Un montaggio simile viene utilizzato per raccogliere dati di oscillazioni 5–100 kHz nella MN di un ECRT. Si utilizza nuovamente una matrice di LPs per ricostruire il vettore dei numeri d'onda nello spazio, insieme a una Sonda di Curling, che fornisce misurazioni della densità elettronica con risoluzione temporale, e una camera ad alta velocità, che registra la luce emessa dal plasma nella sorgente. Lo studio utilizza in modo simile una combinazione della tecnica PSD2P, analisi di coerenza e bi-coerenza per postprocessare i dati delle LPs, mentre la POD è utilizzata per il trattamento dei dati della camera ad alta velocità. Lo studio consente di eseguire una caratterizzazione completa delle due oscillazioni osservate, rispettivamente una a bassa frequenza, che viene attribuita similarmente a un modo di ionizzazione, e un'altra ad una frequenza più alta, la cui caratterizzazione viene tentata in base alla letteratura recente.

1. INTRODUCTION

1.1 Plasmas for space propulsion

Electric propulsion and chemical propulsion are not competitors, but rather complementary. Whilst the latter offers higher overall thrust but is limited in specific impulse due to the energy of the employed chemicals being finite, electric propulsion is technically not limited in exhaust velocities due to the fact that the acceleration takes place through external electric and/or magnetic fields. This allows to save propellant for longer missions, and therefore money. On the other hand, the higher thrust needed during launch requires the use of chemical propulsion [1,2].

Electric propulsion devices can be categorized into different types depending on how the acceleration of the plasma is achieved.

- *Electrothermal*: the plasma is heated electrically, increasing its pressure. This in turn leads the plasma to expand due to thermal dynamics and accelerate.
- *Electrostatic*: the non-neutral plasma is accelerated through the use of a voltage difference applied between two electrodes. The plasma plume often needs to be neutralized by means of a cathode.
- *Electromagnetic*: plasma acceleration is achieved through the interaction of strong magnetic fields, either externally applied or self-imposed, and the currents arising within the plasma.

This manuscript will focus on three types of devices: the Hall Effect Thruster (HET) [3,4]; the Helicon Plasma Thruster (HPT) [5–7]; and the Electron Cyclotron Resonance Thruster (ECRT) [8–11]. HETs are simultaneously characterized as both electrostatic and electromagnetic devices; in fact, while the acceleration of the ions essentially occurs through external application of an electrostatic field, the magnetic field is also critical to the thruster operation, confining electrons and allowing the electrostatic field to be maintained across the channel. HPTs and ECRTs, on the other hand, fall under the electromagnetic category, with the acceleration and expansion of the plasma being driven outwards by an externally applied magnetic field. Notably, the latter two belong to a newer class of electric propulsion devices known as Electrodeless Plasma Thrusters (EPTs), offering potential advantages over traditional and well-established technologies. The technicalities of each of these devices will be elaborated upon within the next subsections.

The plasmas typical of these applications are characterized by having a strong azimuthal relative drift between the essentially-unmagnetized ions and the well-magnetized

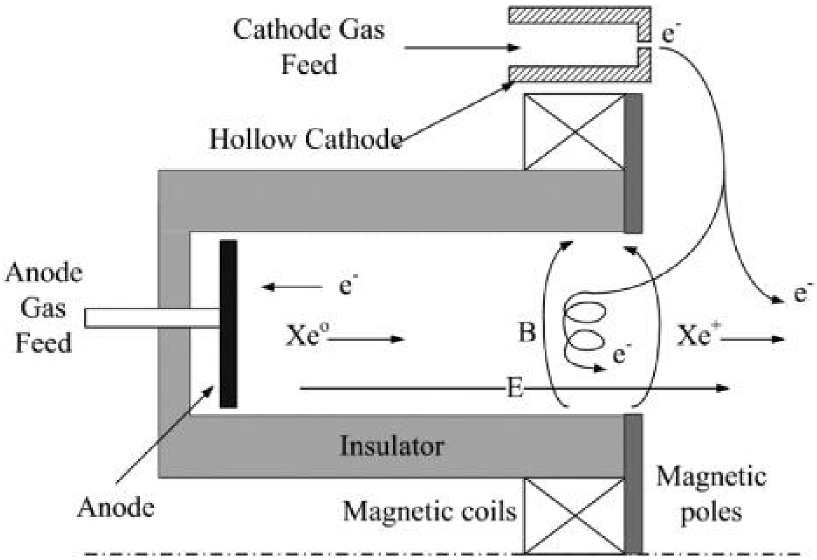

Figure 1.1: Schematic of a Hall Effect Thruster [14].

electrons. Electrons, due to their magnetization, are generally subject to a combination of various drifts, typically $\boldsymbol{E} \times \boldsymbol{B}$, ∇p_e, and $\nabla \boldsymbol{B}$ drifts, with p_e the electron pressure, $\boldsymbol{E}$ the electric field, and $\boldsymbol{B}$ the magnetic field. Ions, on the other hand, remain generally unaffected by such drifts. Overall, the plasma expanding in the plume of the devices studied in this work may be classified as an $\boldsymbol{E} \times \boldsymbol{B}$ discharge. An overview of the fundamental principles of low-temperature $\boldsymbol{E} \times \boldsymbol{B}$ plasmas is provided in Section 1.2.

1.1.1 Hall Effect Thrusters

HETs are among the most established and performing technologies for electric propulsion, and have been actively flying in space since the 70s [12, 13]. They use an axial electrostatic potential to accelerate ions to supersonic speeds. A schematic useful to picture the working principles of a HET is shown in Figure 1.1.

The gas, typically a heavy noble gas such as xenon or krypton, is injected through the anode at the back of the annular chamber and is then ionized by drifting electrons, trapped downstream within the chamber by a magnetic field $\boldsymbol{B}$ applied radially, perpendicular to the electric field $\boldsymbol{E}$. **Free electrons are injected with a cathode, with a significant portion of those flowing back into the chamber and being trapped by the magnetic field, while another portion of those moves downstream to neutralize the plume. The magnetic field $\boldsymbol{B}$ serves the double purpose of keeping the electrons in place and creating the $\boldsymbol{E} \times \boldsymbol{B}$ electron drift, which in turn ionizes the neutrals through bombardment of the trapped electron population.** Ions are created and, being unaffected by the magnetic field due to the plasma being partially magnetized, they are accelerated by the electrostatic potential and eventually escape, generating thrust. The plume is neutralized through the use of an external cathode, which injects electrons. The majority of those are indeed used to neutralize the jet, whereas a smaller portion flows back into the chamber and feeds the drifting electron population, naturally subject to diminishment in time due to recombination and wall losses.

HETs typical efficiencies sit around 60-70% [15, 16] but, despite that, extensive research is still carried out to this day in order to improve their design and the predictive capabilities of simulation tools. More specifically, for instance, the phenomenon of anomalous transport, which will be discussed more in detail later, is still one of the major unanswered questions regarding the operation of these devices.

1.1.2 Electrodeless Plasma Thrusters

Currently, the vast majority of deployed electric propulsion devices employ electron-emitting electrodes in varying capacities, including the aforementioned HETs. Electrodes that are constantly exposed to the plasma suffer from degradation due to sputtering or thermal erosion [17, 18]. Electrode erosion impacts the thruster longevity, and can ultimately affect overall efficiency [18–20]. Furthermore, the use of neutralizer electrodes in these devices requires inert and pure propellants to avoid contamination and degradation of the electron-emitting inserts, preventing the use of alternative propellants both in the thruster unit and the neutralizer [21, 22].

At the power levels currently employed in thrusters (several kW), electrode erosion has not caused serious issues. However, as the demand for more powerful thrusters increases, grids, walls and cathodes will be exposed to more intense fluxes of ions as larger masses of propellant are accelerated, rendering electrode erosion a crucial limiting factor [23]. Electrodeless plasma thruster (EPT) technologies are motivated by advantages such as reduced propellant sensitivity and elimination of neutralizers. In EPTs, energy is transferred to the plasma through body forces, and the absence of a cathode promises both increased lifetime and reduced sensitivity to the purity of the propellant. Nevertheless, the technological readiness level of EPTs is still low in general, as are the demonstrated thrust efficiencies [5, 24, 25].

Numerous EPTs are presently in the developmental phase, with most of them existing at the prototype stage [5, 24, 25]. These thrusters exhibit diverse operational characteristics, contributing to the formation of a broad and varied family of technologies. HPTs and ECRTs are two of such instances. The difference between them lies essentially within the way they ionize the neutrals, which are typically injected through a backplate or from the side walls of the chamber. In the case of HPTs, radiofrequency helicon waves are used to ionize the propellant, whereas ECRTs use microwaves exciting the propellant at the electron cyclotron resonance frequency. In both cases the propellant is a heavy noble gas, but, as mentioned above, the absence of electrodes in direct contact with the plasma allows for a wide range of alternative propellants to be used, such as alkali metals or even water [26].

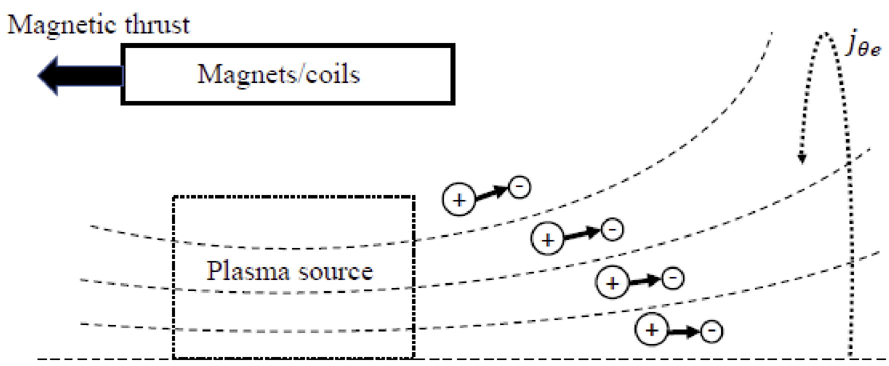

Figure 1.2: Schematic of a Magnetic Nozzle [30]. Due to the axisymmetry, only the top part of the sketch is shown here.

1.1.3 Magnetic Nozzles

Even though the ionization process takes place in different ways, thrust generation in both HPTs and ECRTs is rather similar. In fact, both types of devices employ a divergent magnetic field $\boldsymbol{B}$ downstream from the plasma source, which confines and accelerates the plasma. This geometry is often referred to as Magnetic Nozzle (MN) [27, 28]. A schematic useful to picture the working principles of a MN is shown in Figure 1.2.

The expansion along the magnetic field lines then takes place similarly to a deLaval nozzle, in which particles are expanded downstream thermally. The electrons, being fully magnetized, follow the $\boldsymbol{B}$ field lines performing gyromotions around them, whereas the ions, heavier and unmagnetized, simply tend to expand axially. Azimuthal electron currents interact with the applied magnetic field resulting in a radially-confining and downstream-accelerating force, while an ambipolar electric field $\boldsymbol{E}$ arises in the expanding plasma to maintain charge neutrality. Such force confines electrons and accelerates ions axially, generating thrust. Ions, being massive and little magnetized, eventually detach from the magnetic field lines, which swirl back upon themselves, and the plasma expands into vacuum.

It is noteworthy that HPTs and ECRTs are not the only existing examples of devices employing MNs to generate thrust. With their efficiencies sitting at relatively low values, these devices remain unappealing for industry standards. Presently, their efficiency averages less than 15 %, and only recently higher efficiency levels have been reported [11,29]. The comprehension of the underlying physics governing these thrusters is still limited, prompting a substantial investment of effort into researching their behavior.

1.2 Low-temperature E × B plasmas

Low-temperature $\boldsymbol{E}\times\boldsymbol{B}$ plasmas are a particularly interesting field of study for they occur widely in nature and are typical of various engineering applications, from astrophysics and space propulsion to magnetrons, material processing and more. They usually behave differently in comparison to strongly magnetized plasmas for fusion applications [31–34].

In these plasmas, while electrons possess temperatures ranging from a couple to a few tens of eV, ions typically remain closer to room temperature, with their temperature being often negligible. Consequently, this leads to partially ionized plasmas, characterized by a significant presence of neutrals. In addition, electrons exhibit low energy levels, with their population frequently existing in a non-equilibrium state. In fact, classical collisions are generally ignored in simplified models, whereas Coulomb-type collisions are insufficient to induce equilibrium. This results in electron distribution functions that are often non-Maxwellian, with the possibility of several different populations of electrons coexisting at the same time. Conversely, high-temperature plasmas exhibit extensive ionization, with electron energy levels reaching the keV range.

Secondly, most applications of these plasmas — and the plasmas that will be the focus of this manuscript — are supported by configurations of crossed $\boldsymbol{E}$ and $\boldsymbol{B}$ fields. When a magnetic field $\boldsymbol{B}$ exists perpendicular to an electric field $\boldsymbol{E}$, a common type of drift that is typically referred to as $\boldsymbol{E}\times\boldsymbol{B}$ drift arises. This drift, as well as most of the other drifts that can develop within these plasmas, exclusively affects the electrons, while ions remain basically unperturbed. This happens because, in typical applications, the applied magnetic fields possess magnitudes that are strong enough to magnetize free electrons, yet they do not magnetize ions due to their significantly larger mass and consequently larger Larmor radius. In fact, if L is the characteristic length of the problem at hand, $\rho_e \ll L \ll \rho_i$, where ρ_e denotes the Larmor radius of electrons and ρ_i refers to that of ions. The parameter L can be regarded as the particle mean free path, primarily influenced by the collision rate. Consequently, electrons tend to closely follow magnetic streamlines, undergoing several helical motions around those before colliding with another particle. Ions, in contrast, are much more prone to collisions before completing a full helical motion, predominantly following anisotropic bulk velocities, if any, while trying to maintain charge neutrality.

1.2.1 Instabilities in low-temperature E × B plasmas

It is a known fact that several types of instabilities may develop in low-temperature axisymmetric $\boldsymbol{E}\times\boldsymbol{B}$ plasmas [35, 36], leading to localized oscillation modes and/or broadband turbulence, which can give rise to enhanced, or anomalous, cross-field transport. Notable examples are found in Hall-effect thrusters, Penning discharges, and magnetron discharges [37–43]. In plasma toroids, columns and cylindrical sources, current-driven, gradient-driven, and anisotropy-driven instabilities are known to exist [44–46]. In Helicon sources, low-frequency oscillations and drift wave turbulence/zonal flows have been observed [47–50]. Moreover, the parametric decay instability has been identified as a key mechanism for nonlinear power absorption, and electron and ion heating [51–53]. This instability results from a three-wave nonlinear coupling between the pump Helicon wave and low-frequency ion acoustic waves, generally resulting in a turbulent spectrum. The other partner in the three-wave interaction could be either an electron electrostatic wave [51], a lower-hybrid wave [54], or Trivelpiece-Gould waves [55, 56].

The impact that instabilities and/or turbulence can have on cross-field particle transport, has in turn the potential to compromise plasma confinement [35, 57, 58]. In HETs, control of the plasma confinement is crucial to to achieve efficient ionization and reducing wall erosion [59], whereas in MNs it serves the purpose of ensuring optimal mass utilization of the propulsion system and increasing total efficiency [60]. Additionally, enhanced cross-particle transport could also provide a means for effective electron detachment from the MN closed field lines, to date still an open problem [61–63]. Hence, the lack of a comprehensive understanding of the physics can undermine the optimization of designs and predictive tools alike. Moreover, the presence of oscillations in the plume region may be regarded in some cases as the tell-tale of instabilities within the plasma source, which could drive plasma losses to the walls, and therefore have a direct impact on the propulsive performances of the device.

The next subsections will provide a concise introduction to the relevant oscillating behaviors taking place in the plasma of the devices that will be discussed in Chapters 2 to 4. Note that oscillations within HETs are better understood due to the maturity of the device itself. In fact, decades of experiments and simulations alike effectively advanced the comprehension of the various phenomena taking place within a HET chamber and its plume, but extensive research is still carried out to this day. Conversely, oscillations taking place in MNs are less characterized, offering more room for investigation.

1.2.2 Axial-radial oscillations in HETs

Hall-effect thrusters (HETs) exhibit various types of oscillations over a wide frequency range that affect the discharge current, the plasma properties, and the propulsive performances [1, 64]. While high-frequency oscillations have been suggested as a mechanism behind anomalous electron transport, low-frequency ones also have important consequences on the operation and efficiency of the device [36].

One of the main characterizing oscillations taking place within the discharge of HETs is the so-called *breathing mode*, which occurs within the chamber along the axial direction. The physical mechanism behind breathing oscillations is currently well understood and is usually described as a predator-prey type of ionization/neutral-depletion instability [64–69]. The ionization rate, which depends non-linearly on the electron temperature, is largely non-uniform inside a HET chamber. In a typical HET discharge, the electron temperature and the ionization rate are high close to the exit section of the thruster chamber, where the magnetic field is large and the electron mobility is low. This fact produces the depletion of the neutral density near the exhaust and the ionization front moves back upstream inside the thruster chamber, where the electron temperature and the ionization rate are lower. As the neutral population is depleted and the generated ions are accelerated downstream by the self-adjusted ambipolar electric field producing thrust, the plasma density and consequently the ionization rate drastically decrease at the exhaust, allowing neutral atoms injected through the anode to replenish again the channel. The cycle then restarts, generating a periodic oscillation usually taking place in the 1–20 kHz range, which is generally well visible in the discharge current. The electron energy/temperature is also seen to oscillate with the breathing mode [70].

A second remarkable type of quasi-axial oscillations in the low-frequency range of HET plumes are the *ion transit time* (ITT) oscillations, so called because they are characterized by periods that are roughly equal to the ion residence time in the chamber [64, 71, 72]. The prevalent theory for these oscillations links them to an acoustic instability in the ion acceleration region that, by moving upstream, creates an inhomogeneity in the ion velocity profile along the axial direction. For this reason, two populations of ions generate, a slower one, ahead, and a faster one, which follows up, perturbing the potential distribution and eventually leading the two populations to merge. When they do merge, the ion current locally exceeds the average current, which may result in a change of sign of the local electric field in order to maintain current continuity. Such type of oscillations usually have a quite broad spectrum between 70–500 kHz. Oscillations in this band have also been recorded at the exit of HETs in the azimuthal direction [73, 74]. Recently, ITT oscillations have been linked to the development of long-wavelength azimuthal instabilities leading to anomalous transport in HETs as they interact with azimuthal electron drift instabilities [75].

1.2.3 Relevant oscillations in EPTs

In the context of MNs and depending on its direction, oscillation-enhanced cross-field transport may jeopardize the proper lateral confinement of the expanding plasma, leading to increased divergence angle (outward diffusion), or it could be a means to promote the desired type of electron detachment (inward diffusion).

One of the first theoretical studies on the possible instabilities and their effect on transport is due to Gerwin [76], who hints at the Lower-Hybrid Drift (LHD) instability (and a flute-mode Rayleigh-Taylor instability) as a mechanism that would increase the outward lateral expansion of the plasma. Olsen *et al.* [77] identify rather localized, MHz-level oscillating fields in a high-power MN; they conclude that instability-induced turbulence would be a means for inward electron detachment. Hepner *et al.* [78] use probes to measure a broadband spectrum everywhere in their MN, corresponding to a primarily-azimuthally propagating mode. Under the assumption that this be a LHD instability, they point out an increase of (outward) electron diffusion of two orders of magnitude compared to classical resistivity. Finally, Takahashi *et al.* [79] employ an advanced probe setup to find localized oscillations at around 40 kHz in a different device, which they attribute to a magnetosonic wave, and indicate inward electron detachment.

In addition, other studies also discuss the existence of low frequency ionization instabilities existing in EPTs [80, 81]. While Aanesland *et al.* related the development of the observed oscillations to the existence of a current-free double layer inducing upstream flow of energized electrons from the expansion region into the source [80], Hepner pointed at a predator-prey model to explain those [81]. Additionally, the study of Doyle *et al.* addressed the development of a similar oscillation in the same range of frequencies to an ion acoustic instability, successfully controlled by modulation of the injected radio-frequency signal [82]. Simulations of a MN expansion also related the existence of oscillations in the plume to a U-shaped double layer induced by radial charge separation, which would in turn excite ion Bernstein modes [83].

1.3 Data-driven approach

Traditionally, scientific interpretation of data has relied exclusively on domain expertise and theoretical assumptions. Although a data-driven approach cannot entirely dispense with domain expertise lest misleading conclusions be obtained, it offers the significant advantage of reduced reliance upon restrictive a priori hypotheses regarding the underlying physics. This is useful to minimize the researcher bias and facilitating the extraction of features hidden in the data. Nevertheless, data-driven techniques generally require large volumes of data to increase statistical significance, something that only recently became feasible due to technological advancements in data storage and machine computation capabilities. Consequently, several unrelated branches of the scientific community have been increasingly turning to data-driven methodologies for data analysis, from fluid dynamics [84–88] to plasma fusion [89, 90], acoustics [91], climate [92, 93], biomedicine [94–96], finance [97, 98], and others [99–102].

Lately, these methodologies are slowly finding their way into the electric propulsion community. Some recent works have successfully employed data-driven approaches to obtain predictive semi-empirical models, such is the case for the impinging current in electrospray thrusters [103], the anomalous electron collision frequency [104], and even thruster development [105]. Some other works have applied data-driven algorithms for reducing computing times of numerical simulations [106], improving insufficient frequency resolutions [107], or postprocessing simulation data [108]. Due to the broadness of the topic, the next subsections will only discuss some specific data-driven techniques that are exploited in the present thesis. In the context of this study, depending on the type of data at hand, the choice fell upon techniques for modal analysis or spectral description.

1.3.1 Modal analysis

Complex physical systems often show coherent structures, dominant patterns and leading oscillations that carry most of the important information. However, the isolation of these dominant features from either experimental or simulation data is generally a difficult task, due to the interplay between multiple phenomena, the presence of noise, and transient effects. It is the objective of modal analysis to facilitate the task of uncoupling the underlying physical behaviors, describing the data in terms of few elementary functions or vectors, called *modes*. The Fourier series, for instance, can be classified as a modal decomposition, employing sine and cosine functions of increasing frequency as an orthogonal basis to represent a periodic time-varying signal.

Algorithms for modal analysis can operate on a wide variety of data. However, if the data at hand stems from point-source acquisitions, such as Langmuir probes, the low spatial dimensionality prevents the applicability of some algorithms that work better when a higher resolution in space is available. Other scenarios, e.g. for time-resolved simulations or fast camera experiments, open the possibility to apply a wider range of techniques, allowing for a higher spatial complexity while also resolving the temporal evolution of the plasma. In particular, Proper Orthogonal Decomposition (POD) [109–112] and Dynamic Mode Decomposition (DMD)-like methods [113–116] are snapshot-based algorithms that can be used for postprocessing either experimental or simulation data, decomposing them into intrinsic modes. Both POD and DMD have been extensively applied in several fields of science and engineering, while applications within the electric propulsion community are only recently surfacing. Previously, POD was employed to study the variations induced on spokes characteristics arising in a HET discharge by different cathode discharge currents [117], whereas DMD was employed to infer spatial properties of the breathing mode oscillation by modulating the discharge voltage [118], to isolate different frequency ranges belonging to different instabilities [119], or to extract spatio-temporal coherent patterns with the goal of constructing reduced order models [120, 121].

POD modes are ordered according to an energy-like norm, enabling the identification of the most energetic spatial patterns and their time evolution, noise filtering, and a low-dimensional description of the original dataset that retains the dominant physics [112]. The extracted modes form an orthonormal basis of the linear subspace generated by the snapshots, which facilitates the construction of reduced order models of the underlying dynamics. As a drawback, the associated temporal amplitudes generally exhibit a full spectrum and mix oscillations related to distinct mechanisms.

On the other hand, DMD-like methods expand a spatio-temporal dataset into dynamics-relevant modes with complex exponential time evolution, identifying the involved frequencies and growth/decay rates. Among other tasks, this allows the separation of transient behaviors from the asymptotic oscillations. DMD modes are not orthogonal but each one of them features a single frequency. However, standard DMD [113] can be unreliable for nonlinear systems with large spectral complexity, i.e. exhibiting many distinct superposed oscillating/decaying/growing modes, producing spurious results. DMD is also quite sensitive to the presence of noise in the data [122]. In order to overcome some of these limitations, Higher Order Dynamic Mode Decomposition (HODMD) was recently proposed [115, 123] as an extension of standard DMD. The aim is to improve the capability of the linear model underlying the DMD method of describing nonlinear dynamics within the data, by enlarging the number of coordinates (i.e., degrees of freedom) via time-lagged snapshots. This allows to achieve a more accurate representation of the dynamical properties of the system under study [115].

Technical details of POD and HODMD methods will be illustrated in Chapter 2, where they are applied to simulation data of the plasma in a HET.

1.3.2 Spectral description

One main concern of data-driven algorithms involves the transformation of data into alternative coordinate systems to facilitate interpretation and analysis. The most fundamental coordinate transformation is perhaps the Fourier transform, which provides a way to express the frequency content of a time-varying signal. The formulation of the Fourier transform — and of its predecessor, the aforementioned Fourier series — laid the foundation of spectral analysis and approximation theory.

Spectral density plots, providing insights into the spatial and temporal features of the observed physics, are the objective of every researcher dealing with fluctuations. If the data are purely experimental, extracting these features from measurements is typically a challenging task, one that is riddled with technical complications. While computing frequency spectra from instruments like Langmuir probes through the use of Fourier transform algorithms is more immediate, obtaining a more comprehensive spectral description in the shape of a dispersion diagram $H(k, f)$, being k the wavenumber and f the linear frequency, can prove more difficult. In fact, simultaneously scanning different spatial points with invasive diagnostics is both unfeasible and highly disruptive. While some optical plasma diagnostics have recently been developed allowing to acquire time-resolved data with higher spatial resolution, this often implies that the temporal resolution as a compromise is generally not too high [124, 125].

When the choice falls upon simpler and more cost-effective diagnostics that have limited spatial resolution, such as Langmuir probes, more elaborate experimental setups and postprocessing algorithms are often required. Techniques to infer the spatio-temporal features of plasma turbulence from point-probe sources of data have been extensively used in the past, most of those relying on the definitions of auto- and cross-correlation. A good compendium is provided in [126], which illustrates a number of them and provides practical examples. Among those, the local wavenumber frequency technique, originally developed in [127], has recently received increasing attention within the electric propulsion community due to its simplicity, with a number of works highlighting its potential [78, 128]. Lately re-labeled as Two-Points Power Spectral Density (PSD2P) technique [129], it computes the *sample local wavenumber*, intended to be an approximation of the actual wavenumber k under certain assumptions, through cross-correlating the signals coming from a pair of aligned probes. The algorithm ultimately allows to obtain an estimation of the full $H(k, f)$ dispersion diagram.

Additionally, spectral techniques can be employed to estimate existing correlations between different signals or interactions between different frequencies. In this regard, coherence [130] and bi-coherence [131] analyses represent two well-known examples. Coherence analysis yields the unitary, normalized quantity *magnitude-squared coherence*, measuring the linear correlation between two time series at each frequency. The coherence is directly analogous to the squared correlation coefficient in linear regression. At a given frequency, if the phase of one oscillation is fixed relative to that of another oscillation, then the signals can have a high coherence at that frequency. In the case of signals measured by two aligned Langmuir probes, this information can be used to infer the presence of a traveling wave. Conversely, bi-coherence analysis quantifies quadratic non-linear interactions intrinsic to the data. Specifically, the *bispectral coherency* or *bi-coherence* is also a normalized, unitary value, which serves the purpose of estimating the phase-locking between a pair of modes at frequencies f_1 and f_2 and a mode at the sum-frequency $f_1 + f_2$. The objective of this technique is to identify pairs of interacting frequencies (namely, f_1 and f_2) in the context of three-wave coupling. Applications of both coherence and bi-coherence analyses are found extensively in plasma physics [45, 132] and other unrelated fields [133, 134].

All spectral techniques taken into account in this thesis will be further detailed and applied to experimental data of different thrusters in Chapters 3 and 4.

1.4 Thesis scope and objectives

Realizing the importance of studying plasma oscillations in devices employed for space propulsion, this thesis sets out to advance the general understanding of their governing physics. The investigation covers different thrusters, from more traditional and mature technologies like HETs to novel devices such as HPTs and ECRTs, both employing MNs. To achieve this, various data-driven techniques are studied, adapted and employed to dissect simulation and experimental data of the plasma in such devices, and characterize the observed oscillations. A data-driven approach offers the advantage of limiting the reliance on a priori assumptions, and therefore promises reduced researcher bias and enhanced feature-detecting abilities.

With this in mind, the goals of this thesis may be broken down in three different macro-areas as follows.

- *Contributing to the overall understanding of low-frequency, axial-radial oscillations taking place within HETs*: The study of instabilities in HETs dates back decades, with an ample number of dynamics developing in different regions of the thruster and for different operating conditions. Yet, a significant effort from the community continues to this day, as open research questions still persist. Within the current work, this goal is accomplished by studying axial-radial simulation data of a Stationary Plasma Thrutser (SPT)-100 discharge, providing insights into the spatial structure and temporal behavior of the plasma by successfully isolating the two dominant oscillations observed, namely the breathing mode and the ITT dynamics. Further characterization of both oscillations is achieved by varying the thruster operating condition. Separately reconstructing coexisting oscillations is crucial to better describe each, and reduces mode interplay that can contaminate the interpretation of the results.

- *Fostering the investigation of fluctuations taking place in the plume of novel devices employing MNs, HPT and ECRT prototypes in particular*: Oscillations in MNs, due to the novelty of the inspected devices, are a relatively new field of research. Evidence of various types of oscillations developing in MNs is recently surfacing, with authors attempting to characterize them, providing possible explanations for the underlying physics of the phenomena they observe and the effect these may have on anomalous transport and plume detachment from the applied field. Nonetheless, it is evident that a global understanding of such oscillations is still lacking, especially for what concerns their potential impact on thruster operation and anomalous cross-field electron transport. In the framework of this thesis, the mentioned objective is achieved performing experimental campaigns for the detection of oscillations within the MN of prototypes of HPT and ECRT devices. Different oscillating dynamics are extensively reported, and their characterization is performed with respect to variations of the operating conditions of the device and the spatial position of the diagnostics within the MN. An attempt to explain these phenomena is done by invoking, when possible, results existing in the literature or directly inferring intrinsic features of the oscillations.

- *Illustrating the large potential of data-driven techniques applied to the study of oscillations in low-temperature $\boldsymbol{E}\times\boldsymbol{B}$ plasmas*: Data-driven techniques are nowadays established in several fields of science, but they are only recently slowly paving their way into the electric propulsion community. With the recent advances in machine capabilities and data storage, datasets are gradually becoming larger for better statistical significance. Relying on data-driven techniques, which minimize model-based a priori assumptions, comes with the promise of reducing researcher bias and facilitating the isolation of dominant physical mechanisms. In this thesis, such goal is achieved through the application of an ample array of data-driven algorithms, from POD and HODMD on simulation data with high spatial dimensionality, to PSD2P, coherence and bi-coherence analyses on experimental Langmuir probe acquisitions, which only provide with a much lower spatial resolution. It is worth mentioning that, in some cases, an adaptation (or slight improvement) of the used techniques has been necessary in order to enhance their performance in the context of this work.

1.4.1 Thesis outline

The present manuscript is organized as follows.

- Chapter 2 presents a data-driven modal analysis of plasma oscillations in a SPT-100-like HET in the 1–120 kHz range. Data are generated by a two-dimensional (axial-radial) hybrid particle-in-cell/fluid simulation code for different operating points of the thruster to identify the dominant discharge modes and the relations among the different variables. A discussion is presented about the limitations of POD in isolating the two dominant oscillation mechanisms present in the simulation data, namely the breathing mode and the ITT dynamics, while it is shown how HODMD can appropriately handle this task. Indeed, the computed HODMD components can be clustered into two distinct groups, enabling the separate reconstruction of the dynamics of the two oscillation modes. It is also shown that each plasma variable exhibits a different behavior in each cluster, with the breathing oscillations showing a predominantly global or standing-wave character, while the ion transit time mode shows instead a progressive-wave structure. Changes in the operating condition of the thruster display a significant change in the relative importance of the breathing and ITT modes, while also their characteristic frequencies are slightly modified with respect to the reference operating point. This chapter reports the contents published in the peer-reviewed journal Plasma Sources Science and Technology, titled "Data-driven analysis of oscillations in Hall thruster simulations", by Maddaloni D., Domínguez-Vázquez A., Terragni F., Merino M.

- Chapter 3 illustrates the study of low-frequency oscillations (below 1 MHz) within the plume of a HPT prototype, experimentally collected for two different mass flow rate operating conditions. The data are gathered by means of an array of floating Langmuir probes strategically displaced to resolve the wavevector components along both the azimuthal and parallel directions relative to the magnetic field, at various locations in the plume. The wavevector components are recovered by means of the PSD2P technique, and coherence analysis is employed to assess the consistency of the phase difference between the LP acquisitions. Various features are identified: a very low-frequency ($\simeq$ 4 kHz), global oscillation mode, attributed to an ionization instability in the source; and a broadband, low-coherence, essentially-azimuthal, ion-acoustic-like spectrum at < 200 kHz. Within this range, a mild peak of larger coherence is found at $\simeq$ 50 kHz, followed by a weak secondary peak at $\simeq$ 100 kHz at some locations. Application of bi-coherence analysis allows to estimate the amount of non-linear power coupling intrinsic to the data, indicating the existence of significant coupling taking place between the broadband fluctuations and the driving frequency of 13.56 MHz. This suggests the former are likely the result of a parametric decay instability. Additionally, plasma parameters are extracted from time-averaged data, indicating that the phase velocities of the broadband traveling wave fall in the same order of magnitude as the sound velocity. This chapter reports the contents of the paper entitled "Experimental characterization of low-frequency fluctuations in the magnetic nozzle of a Helicon Plasma Thruster", by Maddaloni D., Bayón-Buján B., Navarro-Cavallé J., Terragni F., Merino M, submitted at the peer-reviewed journal Plasma Sources Science and Technology and currently under review.

- Chapter 4 presents the outcome of a three months long internship at *Office National d'Études et de Recherches Aérospatiales* (ONERA) in Palaiseau, France. This collaboration investigated experimentally plasma oscillations in the range 5–100 kHz in the plume of a coaxial ECRT for different operating conditions of input microwave power, injected xenon mass flow rate, and microwave driving frequency. The presented work proposes measurements acquired simultaneously with three plasma diagnostics: an array of four floating LPs, a curling probe (CP), and high-speed camera imaging to try to characterize the plasma fluctuations. Data at different operating points are analyzed, leading to the identification of two different oscillation modes, one at low frequency ($\simeq$ 9 kHz), and another at higher frequency ($\simeq$ 60 kHz). Dispersion diagrams are once again reconstructed from the LP acquisitions by combining the PSD2P technique with coherence analysis, while also employing bi-coherence analysis to assess non-linear interactions taking place between the two modes observed. The oscillations are captured with very good agreement by all employed diagnostics. In addition, the data from the CP allows to carefully follow the impact of the oscillations upon the plasma density, whereas the data from the camera is analyzed by means of POD to characterize the behavior of the light emitted by the plasma within the source. Possible explanations for the observed behaviors are explored, linking the low-frequency oscillation with a ionization-induced mode, while the higher-frequency one is contextualized taking into account recent literature studying oscillations with similar characteristics in devices employing MNs. This chapter reports the contents of the conference paper "Experimental characterizations of oscillations in the Magnetic Nozzle of an Electron Cyclotron Eesonance Thruster", by Maddaloni D., Boni F., Désangles V., Bayón-Buján B., Merino M., Terragni F., presented at the 38th International Electric Propulsion Conference (IEPC) in Toulouse, France. This work is currently underway to be converted into a journal article.

- Chapter 5 gathers the major contributions of this thesis and sets the ground for a number of future lines of work.

2. DATA-DRIVEN ANALYSIS OF OSCILLATIONS IN HALL THRUSTER SIMULATIONS

In this chapter, simulation datasets of a Stationary Plasma Thruster (SPT)-100 class Hall Effect Thruster (HET), obtained from a two-dimensional (2D) axisymmetric hybrid particle-in-cell (PIC)/fluid numerical code named HYPHEN-HET, are analyzed using Proper Orthogonal Decomposition (POD) and Higher Order Dynamical Mode Decomposition (HODMD). The 2D maps of the plasma density, the neutral density, the electron temperature, the plasma potential, and the axial ion current density are investigated to identify the dominant discharge modes in the 1–120 kHz range and the relations among the different variables. A discussion is presented about the limitations of POD in isolating the two dominant oscillation mechanisms present in the simulation data, namely the breathing mode and the ion transit time (ITT) dynamics, while it is shown how HODMD can appropriately handle this task. Noise and transients in the data are characterized and removed, while the persistent breathing and ITT oscillations are identified with and reconstructed from ‘clusters’ of stable HODMD modes, which enables the investigation of their spatial, frequency, and phase features.

This chapter represents a transcription of the following journal paper (without the introduction section):

- **Maddaloni D.**, Domínguez-Vázquez A., Terragni F., Merino M., "Data-driven analysis of oscillations in Hall thruster simulations". Plasma Sources Science and Technology. 2022, May 3; 31(4):045026. Doi: 10.1088/1361-6595/ac6444.

The Ph.D candidate carried out the entirety of the postprocessing of the simulation data, while also fundamentally contributing to the data interpretation and analysis. Additionally, they performed the adaptation and tuning of the data-driven algorithms employed within this chapter. The candidate also undertook the initial drafting of the manuscript.

2.1 Simulations setup and data overview

The 2D axisymmetric hybrid PIC/fluid, OpenMP-parallelized HET simulator named HYPHEN-HET is used to generate the data for this study. The details of the underlying model and its numerical implementation are detailed in [135–140]. In the following, only a summary of the main aspects is provided.

The dynamics of the quasineutral plasma in the axial-radial $z-r$ domain (see Figure 2.1) are simulated by two main modules: the ion module, which follows a Lagrangian PIC approach for simulating the dynamics of the heavy species (i.e., singly- and doubly-charged ions, and neutrals), and the electron module, which implements a magnetized drift-diffusive (inertialess) fluid model for the electron population, including their energy equation. Single ionization rates are obtained from the BIAGI database [141], while double ionization rates follow the Drawin model [142]. An additional, anomalous electron collisionality $\nu_t = \alpha_t \omega_{ce}$ is included in the electron momentum equation to phenomenologically represent the effect of plasma turbulence on electron transport [66, 143, 144], where α_t is a tuning parameter modeling the turbulence level and ω_{ce} is the electron gyrofrequency. Here, a value $\alpha_t = 0.02$ [145] is set in the full domain for all simulation cases, so that the obtained plasma solution is representative of typical SPT-100 HET experimental data in terms of thrust and specific impulse [146, 147]. It is noted however that existing works [71, 148] suggest an influence on the ITT oscillations of the anomalous electron transport, and that a more accurate treatment may require varying α_t spatially and with the thruster operating point. **The simulation results are extensively validated against experiments and other simulation tools for a wide variety of operating conditions and input parameters, both on a time-averaged and time-resolved scale [139, 140, 149]. Additionally, recent studies also investigate the behavior of the breathing mode through the results of the HYPHEN simulator [118, 150], further corroborating the validation of the code**.

Each code module employs a different mesh, optimized for its needs: a structured mesh for the ion module and an unstructured, magnetic-field-aligned mesh (MFAM) for the electron module. Interpolation is used to carry the necessary coupling variables across modules. Lastly, a dedicated sheath module provides the boundary conditions to the quasineutral plasma bulk domain, by solving the non-neutral plasma sheaths that develop at the thruster walls, which are treated as thin surfaces. The emission of secondary electrons from the boron nitride walls [151], and the ion recombination and accommodation of neutrals at all walls [139] are also taken into account. The downstream boundaries are free-particle-loss and zero-current boundaries, while at the axis $r = 0$ symmetry conditions are imposed.

Table 2.1 lists the main parameters and the thruster operating conditions for the various simulations used in this work, hereafter classified as the *nominal* case and the two *off-nominal* cases (with lower discharge voltage and higher mass flow rate, respectively; while all other input parameters are kept constant). A flux of neutral xenon (Xe) atoms $\dot{m}_A$ is injected with a Maxwellian distribution from the anode wall, upstream in the thruster channel. According to the cathode model presented in [152], the external neutralizer, identified as the reference point for the plasma potential ϕ, where $\phi = 0$, is represented by a single mesh cell located in the near plume region, indicated by a white round marker in Figure 2.1, from where 3 eV electrons are injected into the domain. The net current emitted by the cathode is imposed to be equal to the current collected at the anode wall at each time step, which is the discharge current I_d. A prescribed discharge voltage V_d is set between the anode wall and the cathode element. The resulting time-averaged discharge characteristics are reported in Table 2.1 for each simulation case.

Each simulation features a total number of $24 \cdot 10^4$ simulation steps (equivalent to 3.6

Simulation parameter / variable peak	**Units**	**Nominal case**	**Low voltage case**	**High mass flow rate case**
PIC mesh number of cells, nodes	-		1464, 1553	
MFAM number of cells, faces	-		4822, 9796	
Cathode location: z, r	cm		3.12, 6.80	
Simulation (PIC) timestep, Δt	$\mathrm{s} \cdot 10^{-8}$		1.50	
Total number of simulation steps	-		240000	
Injected Xe mass flow, $\dot{m}_A$	mg/s	5	5	6
Discharge voltage, V_d	V	300	200	300
Average discharge power, P_d	kW	1.8	1.0	2.2
Plasma density, n	$\mathrm{m}^{-3} \cdot 10^{18}$	1.50	1.43	1.84
Electron temperature, T_e	eV	32.8	22.7	32.9
Total axial ion current density, j_{zi}	$\mathrm{A\ m}^{-2} \cdot 10^{3}$	1.17	1.08	1.44
Neutral density, n_n	$\mathrm{m}^{-3} \cdot 10^{19}$	2.88	2.90	3.47

Table 2.1: Main SPT-100-like HET simulation parameters for the nominal and off-nominal cases, together with the peak values of the time-averaged maps of the main variables. Refer to Domínguez-Vázquez *et al.* [140] for further details regarding the simulation parameters that are not mentioned here.

ms of physical time), in which the obtained discharge current undergoes around 50–60 HET breathing mode cycles. All computed variables are time-averaged and stored every 100 simulation steps (equivalent to 1.5 µs) so that, for each test case, a total number of 2400 snapshots is available. It has been checked that, increasing the number of retained snapshots leads to similar results in our analysis; hence, the considered data carry all relevant information for the present study. Note that such data should allow to extract phenomena with frequencies up to $\sim$ 340 kHz. As mentioned in the introduction, the analyzed variables are the plasma density n, the neutral density n_n, the electron temperature T_e, the electrostatic potential ϕ, and the total axial ion current density j_{zi} (which adds up the contributions of single and double ions). The time-averaged 2D maps of some plasma properties in the nominal case are shown in Figure 2.1. The plasma density peaks inside the channel at around 10^{18} m^{-3} and decreases in the plume region as the plasma expands. A second density maximum appears near the thruster centerline, where the annular jet converges on the axis of symmetry. The electron temperature is largest on the magnetic lines near the cathode (indicated by a white marker in plot (a)), where it reaches 30–35 eV. The electrostatic plasma potential axially decreases with the plume expansion. It is worth remarking that neutral density (not shown in Figure 2.1) is simulated with a lower

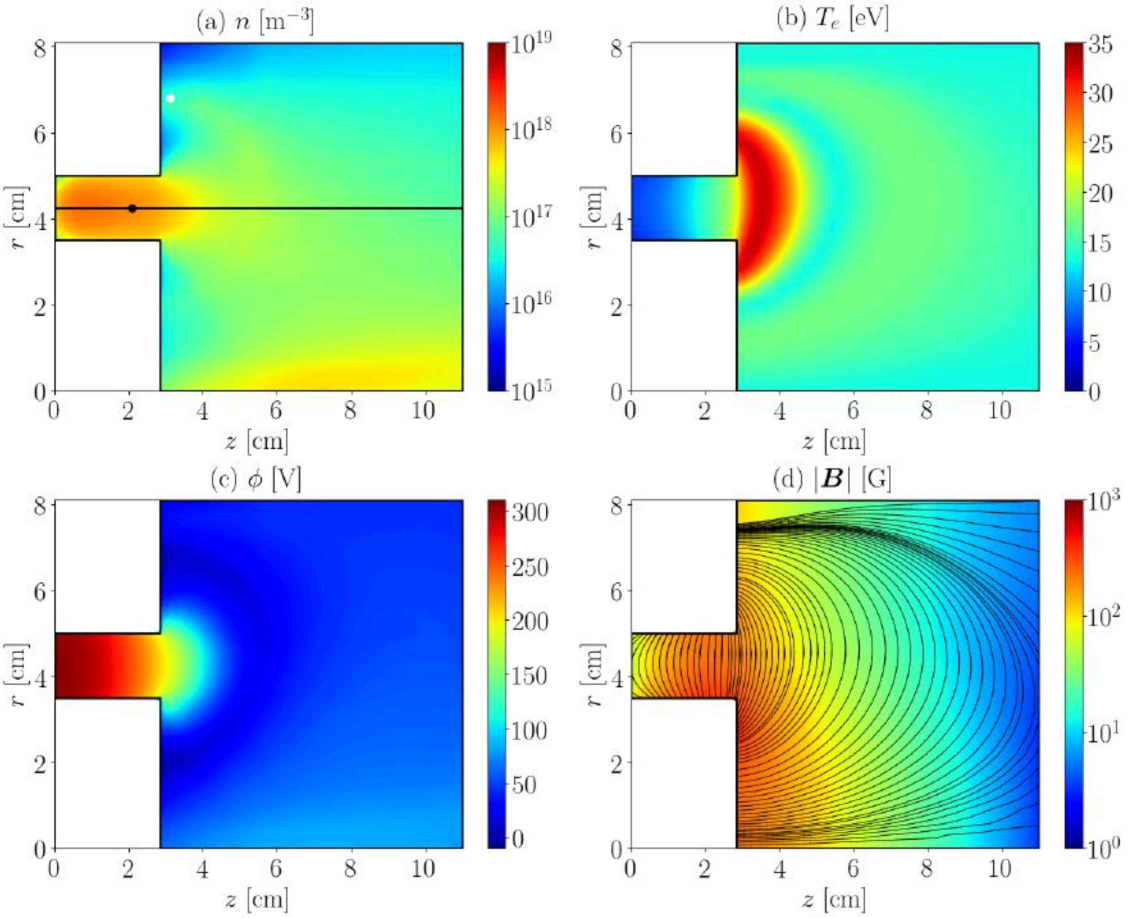

Figure 2.1: Time-averaged 2D maps of (a) plasma density n, (b) electron temperature T_e, (c) plasma potential ϕ, and (d) magnetic field intensity $|\boldsymbol{B}|$, in the nominal case. In plot (a), the white marker shows the location of the cathode emission, while the black marker depicts one significant point along the centreline (shown by a black line) at $(z, r) = (2.10, 4.16)$ cm that will be referred to hereafter. For the other analyzed variables (not shown), namely ion current density j_{zi} and neutral density n_n, the time-averaged maximum values are $1.17 \cdot 10^3$ A m^{-2} and $2.88 \cdot 10^{19}$ m^{-3}, respectively.

count of particles per cell to lighten the computational cost. As discussed below, this will limit the number of modes for n_n that can be reliably extracted from the analysis.

The time and frequency response of the discharge current $I_d - \overline{I}_d$ and the plasma density $n - \overline{n}$ at one representative point inside the domain, with coordinates $(z, r) = (2.10, 4.16)$ cm, are shown in Figure 2.2, where their mean values $\overline{I}_d$ and $\overline{n}$ are also reported. As can be observed, the discharge current is dominated by low-frequency oscillations near 10^4 Hz (plus several harmonics), corresponding to the breathing mode, with amplitudes larger than their mean value. The spectrum has a second, smaller but wider peak at higher frequencies ($\sim 10^5$ Hz), which is related to the ITT dynamics. The response of the plasma density at the chosen point visibly shares the same features as the discharge current.

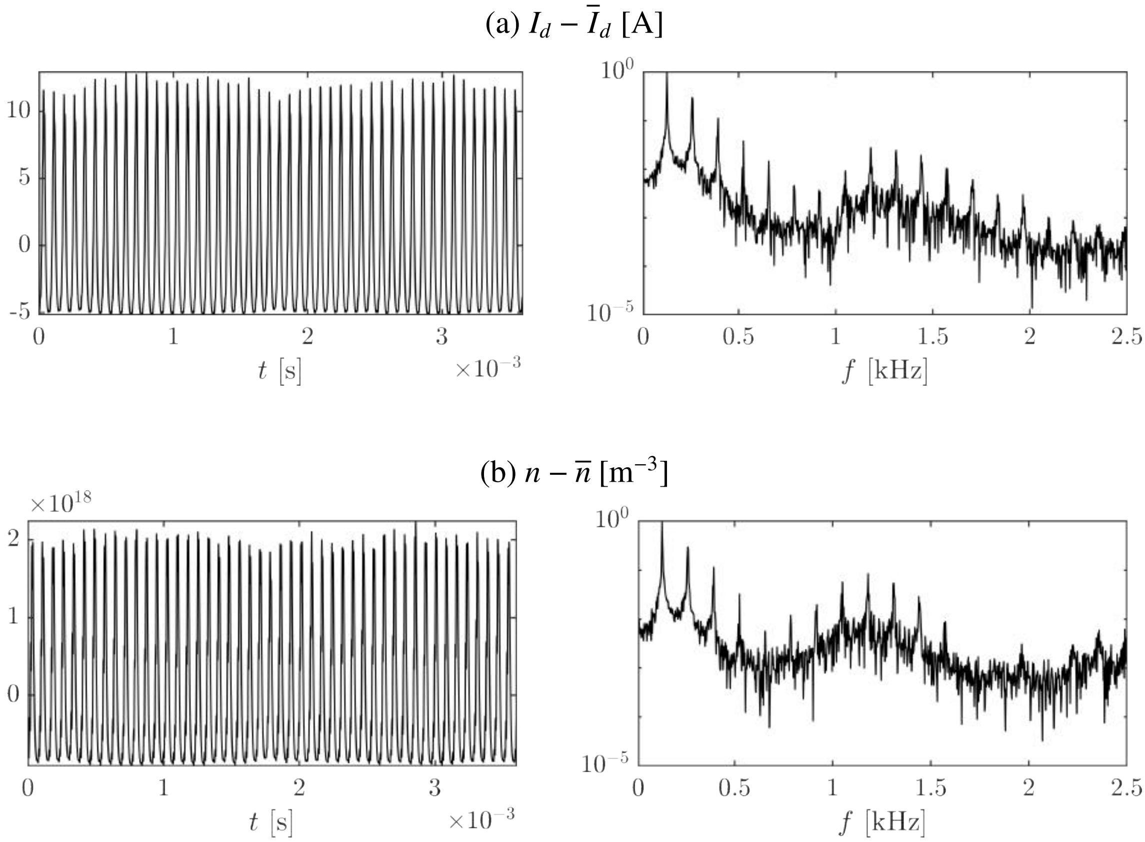

Figure 2.2: Time evolution and Fourier transform of (a) the discharge current $I_d - \overline{I}_d$ and (b) the plasma density $n - \overline{n}$ at one representative point inside the domain with coordinates $(z, r) = (2.10, 4.16)$ cm, in the nominal case. Oscillations exhibit a magnitude of almost three times their mean values, given by $\overline{I}_d = 5.99$ A and $\overline{n} = 1.07 \cdot 10^{18}$ m^{-3} for the two variables.

2.2 Data-driven analysis approach

In order to illustrate the analysis procedure by means of the POD and HODMD techniques, spatio-temporal data given by N real snapshots of dimension M, namely $\boldsymbol{q}_1, \ldots, \boldsymbol{q}_N \in \mathbb{R}^M$, are considered. These vectors will store the values of a physical variable $\boldsymbol{q}$ of interest at the M spatial mesh points involved in the numerical simulations,

$$\boldsymbol{q}_n = \boldsymbol{q}(t_n), \tag{2.1}$$

where time instants are $t_n = (n-1)\,\mathrm{d}t$, for $n = 1, \ldots, N$. Note that the snapshots in equation (2.1) can be organized as columns of the $M \cdot N$ so-called *snapshot matrix* $\boldsymbol{Q} = [\boldsymbol{q}_1, \boldsymbol{q}_2, \cdots, \boldsymbol{q}_N]$. Prior to any analysis, the time-averaged values are subtracted from $\boldsymbol{Q}$.

2.2.1 Proper orthogonal decomposition

According to the method of snapshots, standard truncated POD [110, 112] applied to the vectors in equation (2.1) provides $K < \min\{M, N\}$ orthonormal POD modes, $\boldsymbol{w}_1, \ldots, \boldsymbol{w}_K \in$

$\mathbb{R}^M$, such that each $\boldsymbol{q}_n$ can be approximated as

$$\boldsymbol{q}_n \approx \sum_{k=1}^{K} \alpha_n^k \boldsymbol{w}_k, \tag{2.2}$$

where the coefficients α_n^k (the POD amplitudes) result from the orthogonal projection of the snapshots onto the linear subspace generated by the modes, namely $\alpha_n^k = \langle \boldsymbol{q}_n, \boldsymbol{w}_k \rangle$. Note that equation (2.2) yields the best joint root mean square (RMS) approximation of the snapshots based on K modes, with respect to the considered inner product $\langle \cdot, \cdot \rangle$. Standard POD based on the Euclidean inner product can be efficiently computed via singular value decomposition (SVD) [153] of the snapshot matrix,

$$\boldsymbol{Q} = \boldsymbol{W} \boldsymbol{\Sigma} \boldsymbol{U}^T, \tag{2.3}$$

where $\boldsymbol{W}$ ($M \cdot M$) and $\boldsymbol{U}$ ($N \cdot N$) are two orthogonal matrices ($\boldsymbol{W}^T \boldsymbol{W} = \boldsymbol{U}^T \boldsymbol{U} = \boldsymbol{I}$), while $\boldsymbol{\Sigma}$ ($M \cdot N$) is a diagonal matrix whose elements σ_k on the main diagonal are the singular values. The latter are real, non-negative, and arranged so that $\sigma_1 \geq \sigma_2 \geq \ldots \geq \sigma_N \geq 0$. Note that the singular values are the square roots of the eigenvalues of the correlation matrix $\boldsymbol{Q}^T \boldsymbol{Q}$, while the POD modes are precisely the columns of $\boldsymbol{W}$.

In the context of POD, each mode is ranked according to the magnitude of the corresponding singular value, which is related to the energetic content of the mode. Here, the term ‘energy’ refers to the Euclidean norm of the data, hence the energy associated with each POD mode is easily seen to be the square of the corresponding singular value [110]. Thanks to this, POD is widely used for dimension reduction and noise filtering purposes, since it allows to eliminate the smallest and redundant contributions to the data by imposing a truncation on the reconstruction given by equation (2.2). Indeed, the appropriate number K of POD modes to be retained for a desired accuracy ε is selected by imposing that

$$E_{\text{RMS}}(K) = \frac{\sqrt{\sum_{j=K+1}^{N} (\sigma_j)^2}}{\sqrt{\sum_{j=1}^{N} (\sigma_j)^2}} < \varepsilon, \tag{2.4}$$

where $E_{\text{RMS}}(K)$ is the relative RMS error when reconstructing all snapshots by means of K POD modes [153]. In equation (2.4), the threshold ε is related to the amount of energy that is neglected. Figure 2.3 shows such error vs K for the reconstruction of the plasma density snapshots in the nominal case. After a fast decrease, E_{RMS} becomes fairly flat, indicating that around $K = 100$ POD modes are necessary to approximate the data within a relative RMS accuracy of $\varepsilon \approx 10^{-2}$. The final drop of the error suggests that higher-order modes are related to noise, which has a level of at least 1% for the performed simulations.

On the other hand, the frequency response of a POD mode can be extracted from its time-dependent POD amplitude by means of the Fourier transform. Thus, the decomposition allows to have a close look at the dominant patterns underlying the data and their evolution. Nevertheless, POD may not provide a strict identification and isolation of the different involved dynamics, since (i) modes are ranked according to energetic content and

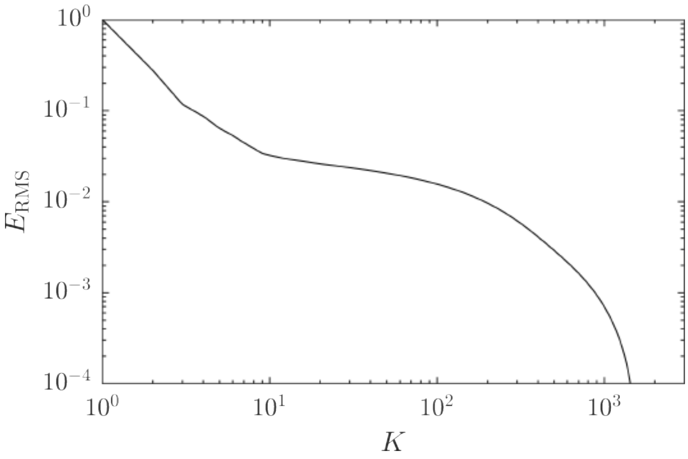

Figure 2.3: Relative RMS reconstruction error as defined in equation (2.4) vs the number K of retained POD modes, for the plasma density n in the nominal case.

not to their dynamical importance and (*ii*) each mode typically exhibits a spread spectrum, with a mix of frequencies.

2.2.2 Higher order dynamic mode decomposition

DMD-like methods are suitable for the analysis of spatio-temporal data associated with dynamics exhibiting a superposition of time-dependent, exponential growth or decay and oscillations [113]. More precisely, they aim at decomposing each snapshot $\boldsymbol{q}_n$ by an expansion with complex-exponential components of the form

$$\boldsymbol{q}_n \approx \boldsymbol{q}_n^{\mathrm{DMD}} = \sum_{k=1}^{K} a_k \boldsymbol{\psi}_k e^{(\delta_k + i\omega_k)t_n}, \tag{2.5}$$

being $\boldsymbol{\psi}_k$ complex, normalized (with unit RMS norm) spatial modes, $a_k > 0$ their real amplitudes, and ω_k and δ_k the associated frequencies and growth rates, respectively. Such decomposition, in fact, allows a very specific characterization of each mode in terms of a single amplitude, frequency, and growth rate. The dynamical relevance of each mode within the data is given by its amplitude, being a_k the amplitude of $\boldsymbol{\psi}_k$ at the beginning of the timespan where the snapshots are sampled, namely at $t_1 = 0$. On the other hand, according to equation (2.5), the temporal evolution of the data comprises a purely oscillating part (terms with negligible growth rates), corresponding to the asymptotic dynamics or attractor, and decaying or growing contributions (terms with non-negligible growth rates). Note that decaying or growing modes can be associated with transient processes, which become less relevant as the data sampling window becomes longer.

Standard DMD [113] relies on the so-called *Koopman assumption*, according to which a linear mapping is assumed to exist between each snapshot and the next one through the Koopman matrix $\boldsymbol{A}$, so that

$$\boldsymbol{q}_{n+1} = \boldsymbol{A}\boldsymbol{q}_n, \tag{2.6}$$

for $n = 1, \dots, N-1$. Note that equation (2.6) is not intended to be the actual physical model underlying the data, but a tool leading to an expansion of the form (2.5). Indeed, once the matrix $\boldsymbol{A}$ is computed (e.g., from the snapshot matrix via the pseudo-inverse), the growth rates and frequencies appearing in equation (2.5) are related to the nonzero eigenvalues μ_k of $\boldsymbol{A}$ as

$$\delta_k + i\omega_k = \frac{1}{\mathrm{d}t}\ln(\mu_k). \tag{2.7}$$

The modes $\boldsymbol{\psi}_k$ are the associated (normalized) eigenvectors. However, in many real-life applications (including HETs), standard DMD may yield spurious results because of strong non-linearities and noise intrinsic in the data, which leads to a loss of consistency between the assumption (2.6) and the equation (2.5). Further details can be found in [113, 154].

A way to overcome this limitation consists in introducing the *higher order Koopman assumption* [115] as follows

$$\boldsymbol{q}_{n+d} = \boldsymbol{A}_1\boldsymbol{q}_n + \boldsymbol{A}_2\boldsymbol{q}_{n+1} + \ldots + \boldsymbol{A}_d\boldsymbol{q}_{n+d-1}, \tag{2.8}$$

for $n = 1, \dots, N-d$, where the tunable parameter $d > 1$ defines time-lagged (delayed) snapshots to use in the analysis. This has the effect of enlarging the dimension of the problem space in which a linear approximation of the data is sought. Equation (2.8) can then be rewritten as

$$\widetilde{\boldsymbol{q}}_{n+1} = \widetilde{\boldsymbol{A}}\widetilde{\boldsymbol{q}}_n, \tag{2.9}$$

being

$$\widetilde{\boldsymbol{q}}_n = \begin{bmatrix} \boldsymbol{q}_n \\ \boldsymbol{q}_{n+1} \\ \vdots \\ \boldsymbol{q}_{n+d-2} \\ \boldsymbol{q}_{n+d-1} \end{bmatrix}, \qquad \widetilde{\boldsymbol{A}} = \begin{bmatrix} \boldsymbol{0} & \boldsymbol{I} & \boldsymbol{0} & \dots & \boldsymbol{0} & \boldsymbol{0} \\ \boldsymbol{0} & \boldsymbol{0} & \boldsymbol{I} & \dots & \boldsymbol{0} & \boldsymbol{0} \\ \vdots & \vdots & \vdots & \vdots & \vdots & \vdots \\ \boldsymbol{0} & \boldsymbol{0} & \boldsymbol{0} & \dots & \boldsymbol{I} & \boldsymbol{0} \\ \boldsymbol{A}_1 & \boldsymbol{A}_2 & \boldsymbol{A}_3 & \dots & \boldsymbol{A}_{d-1} & \boldsymbol{A}_d \end{bmatrix}, \tag{2.10}$$

where $\widetilde{\boldsymbol{A}}$ is called the modified Koopman matrix, while $\boldsymbol{I}$ and $\boldsymbol{0}$ are the $M \cdot M$ unit and null matrices, respectively. The modified snapshots $\widetilde{\boldsymbol{q}}_n$ can be organized as columns of the *modified snapshot matrix* $\widetilde{\boldsymbol{Q}}$.

The procedure to obtain the expansion in equation (2.5) relying on the assumption in equation (2.9) is called higher order dynamic mode decomposition (HODMD), which is now briefly summarized following [115], where a detailed illustration of the algorithm can be found.

1. An initial SVD filtering is performed on the original snapshot matrix $\boldsymbol{Q}$ in order to eliminate redundancies and noise. This is accomplished by imposing a reduction tolerance ε_1 on the retained singular values in the data reconstruction by means of equation (2.4).

2. The filtered snapshots are used to build the modified snapshot matrix $\widetilde{\boldsymbol{Q}}$, by choosing a suitable number d of delayed snapshots.

3. The matrix $\widetilde{\boldsymbol{Q}}$ is SVD-filtered by means of a reduction tolerance ε_2 (cf. step 1).

4. Standard DMD is applied to the filtered matrix $\widetilde{\boldsymbol{Q}}$ to calculate the modes, growth rates, and frequencies in the expansion (2.5).

5. The amplitudes are computed via least-squares fitting. Then, modes and amplitudes are conveniently rescaled, by requiring that $\boldsymbol{\psi}_k$ exhibit unit RMS norm while preserving the product $a_k\boldsymbol{\psi}_k$.

6. A final truncation of less dynamically relevant modes is performed by imposing a relative tolerance $\varepsilon_{\mathrm{DMD}}$ on the retained amplitudes.

The implementation of the HODMD algorithm used in this work is based on the original code by Le Clainche and Vega [155] but it was adapted to the present application. Indeed, the amplitudes calculation (step 5) is based on [156]. Moreover, a different way of truncating the final expansion (2.5) is introduced in step 6, where a mode $\boldsymbol{\psi}_j$ is neglected if

$$\int_\tau a_j\, e^{\delta_j t}\mathrm{d}t \Big/ \max_k \int_\tau a_k\, e^{\delta_k t}\mathrm{d}t \;<\; \varepsilon_{\mathrm{DMD}}. \tag{2.11}$$

Thus, a mode is disregarded if its mean importance over the considered timespan τ is smaller than the desired threshold. Note that the condition in equation (2.11) is equivalent to $a_k/\max_k a_k < \varepsilon_{\mathrm{DMD}}$ if all growth rates are negligible, which may not be the case in the presence of growing and decaying transients, noise or numerical errors.

Finally, in the present work, the HODMD algorithm described above is *iteratively* applied (with the same parameter values), after reconstructing the data by means of the expansion (2.5), to further filter out the less relevant HODMD modes [122, 123]. The iterative process stops when the number of computed modes is maintained after two consecutive iterations.

2.2.3 HODMD parameter tuning

As mentioned, the HODMD algorithm depends on some tunable parameters: the number d of delayed snapshots, the reduction tolerances ε_1 and ε_2, and the amplitude tolerance $\varepsilon_{\mathrm{DMD}}$. A proper choice of the value of these parameters is determinant for a successful HODMD analysis [115, 123].

Firstly, the number d of delayed snapshots is the primary parameter to be calibrated. A proper selection of d is essential to deal with large spectral complexities, nonlinear dynamics, and noisy data. Indeed, numerical experimentation with manufactured, one-dimensional test data (constructed by the superposition of K complex exponentials) showed that d must be increased proportionally to K for the HODMD algorithm to be able to capture the different modes. Also, it should be incremented even more when adding random noise to the data. An insufficient value of d was seen to make the algorithm miss some of the existing modes, and fail to predict the involved frequencies and growth rates.

As a side note, more δ_k than expected were systematically negative (i.e., the computed reconstruction was slightly decaying). This seemed to be related to the method to find $\widetilde{\boldsymbol{A}}$ in equation (2.9). Indeed, if computing $\widetilde{\boldsymbol{B}}$ in the reciprocal relation $\widetilde{\boldsymbol{q}}_n = \widetilde{\boldsymbol{B}}\widetilde{\boldsymbol{q}}_{n+1}$, more δ_k were systematically positive (i.e., the computed reconstruction was slightly exploding). In order to identify a suitable range for d, an empirical analysis was performed, inspecting the relative RMS error of the HODMD reconstruction as a function of d. It was found that, while this error is large for low values of d, it plateaus for $d > 400$–600 depending on the variable. The conservative value $d = 1000$ was finally selected for all variables, for which the relative RMS reconstruction error is sufficiently small (between 0.05 and 0.15). In addition, it was checked that variations of d around that value do not strongly affect the HODMD outputs.

Secondly, in this work, the two reduction tolerances were kept the same, namely $\varepsilon_1 = \varepsilon_2 = \varepsilon_{\mathrm{SVD}}$. Note that their value controls the relative RMS error of each SVD truncation, as in equation (2.4). As anticipated, the simulation data have a noise level of at least 1%. This means that any SVD mode with singular value smaller than that level should be regarded as noise. For this reason, $\varepsilon_{\mathrm{SVD}} = 0.01$ was imposed for all considered variables, except for the neutral density, for which $\varepsilon_{\mathrm{SVD}} = 0.05$, since the latter was computed with less accuracy as mentioned in Section 2.1.

Finally, the amplitude tolerance was set to $\varepsilon_{\mathrm{DMD}} = 5 \cdot 10^{-4}$ for all variables. This parameter is not critical though and, in fact, the chosen value is generally quite indulgent since it allows the majority of the HODMD modes to be retained.

Figure 2.4 illustrates the amplitudes a_k and the decay/growth rates $|\delta_k \tau|$ (where τ is the total timespan of the simulation) vs the frequencies, for the plasma density n in the nominal case. Both a_k and $|\delta_k \tau|$ are symmetric around the zero-frequency, since the processed snapshots are real. As it can be observed, the HODMD spectrum of the plasma density n has qualitatively the same features as the spectrum of the original data shown in Figure 2.2. As discussed in Section 2.3, the dominant modes in the center of the amplitude diagram are associated with the breathing mode, while the secondary peaks correspond to the ITT dynamics. The spectrum contains several harmonics of these modes. Note that, in this figure, a large number of modes is recovered, but only a small fraction of them has large amplitudes. Indeed, the latter are those describing the dominant oscillations underlying the data, which this work aims at analyzing. The rest of the modes crowd at the bottom of the amplitude diagram and exhibit larger values of $|\delta_k \tau|$. As such, they are associated with transients, secondary phenomena, and noise in the data, hence they will be disregarded.

While most of these modes may also be filtered out by a more aggressive value of $\varepsilon_{\mathrm{DMD}}$, in the present work the HODMD method was iterated on the reconstructed data, until achieving convergence of the HODMD diagrams. This reduces the number of retained modes, and slightly refines the values of the involved a_k and δ_k. The number of necessary iterations depends on the variable: for instance, about 40 and 70 iterations were

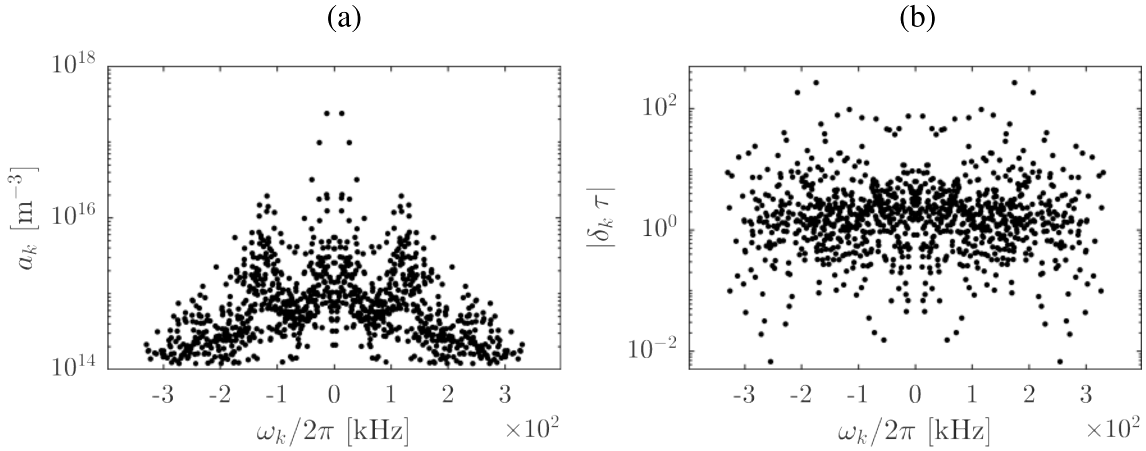

Figure 2.4: HODMD (a) amplitudes and (b) growth rates (normalized by the total timespan τ) vs the frequencies, for the plasma density n in the nominal case, after a single run of the HODMD algorithm with parameter values $d = 1000$, $\varepsilon_{\mathrm{SVD}} = 0.01$, and $\varepsilon_{\mathrm{DMD}} = 5{\cdot}10^{-4}$.

typically required in the nominal case for the plasma density and the neutral density, respectively.

2.3 Results and discussion

In this section, after a brief discussion on the POD of the data, the HODMD technique is applied to each variable of interest in the various simulation cases and the results are discussed. It was checked that the simultaneous analysis of all the variables together (i.e. by normalizing each variable with its RMS norm and concatenating them in a single snapshot matrix), yields similar results.

2.3.1 Nominal case

Figure 2.5 shows the first six normalized POD modes of the plasma density and the electron temperature, together with their temporal and frequency responses, in the nominal case, which has $V_d = 300$ V and $\dot{m}_A = 5$ mg/s as presented in Table 2.1. The energetic dominance of the first two modes is evident, as their energy norms represent above 95% of the total. These two POD modes correspond well to the breathing mode dynamics, in view of their frequency spectrum, with a dominant frequency equal to 13.1 kHz and several higher harmonics. This value is close to that obtained in previous simulations [65, 157, 158] and within the 10–30 kHz range reported in experiments [64, 66, 68]. Their spatial structure shows that these oscillations are mainly axial. In addition, they are essentially restricted to the discharge channel and, in the case of the electron temperature, also to the near plume region, on the magnetic lines where the neutralizer is located.

However, the next four POD modes contain a mixture of frequencies belonging to what are arguably different behaviors, covering both the breathing and ITT frequency

	n [m^{-3}]	T_e [eV]	ϕ [V]	j_{zi} [A m^{-2}]	n_n [m^{-3}]
Breathing dominant mode (13.1 kHz)	$2.36 \cdot 10^{17}$	2.77	11.4	244	$7.94 \cdot 10^{17}$
ITT dominant mode (118 kHz)	$1.24 \cdot 10^{16}$	0.29	1.51	7.23	-

Table 2.2: Summary of frequencies and amplitudes of the dominant HODMD modes in the two dynamics clusters, for all analyzed variables in the nominal case.

ranges. Indeed, the spectrum of these POD modes exhibits some energy content at the same frequencies as the first two, plus a comparable amount of energy spread over the range of frequencies 100–130 kHz, peaking at 118 kHz, which corresponds to the ITT oscillations. Thus, these POD modes reproduce such higher-frequency mechanics but are strongly modulated by the breathing mode fundamental frequency. The spatial patterns described by these modes are mainly axial too, but exhibit a shorter wavelength, some radial structure, and reach across the thruster axis.

This mixture of breathing and ITT dynamics illustrates that POD is unable to correctly isolate and separate the two types of oscillatory mechanisms present in the thruster. This is related to the fact that, as previously stated in Section 2.2.1, POD recognizes the most energetically-dominant structures in the data, regardless of their dynamical relevance and frequency content.

Amplitude vs frequency diagrams resulting from the application of HODMD are displayed in Figure 2.6. Plasma density and electron temperature exhibit a similar diagram, consisting of two clear peaks: the first one corresponds to the breathing mode fundamental frequency, 13.1 kHz, and the second one to the ITT mode fundamental frequency, 118 kHz, matching the peaks visible in the POD results (compare with Figure 2.5). The axial ion current density and the plasma potential (not shown) have similar behaviors. This two-peak distribution suggests clustering the HODMD modes into two groups, the ‘breathing mode components’ and the ‘ITT components’. These are shown in Figure 2.6 by blue circles and red diamonds markers, respectively. This clustering is in agreement with the typical breathing and ITT frequency ranges reported in the literature [73, 148, 159], and is further supported by a clear different spatio-temporal behavior of the modes belonging to each one of the two clusters (discussed further down). Table 2.2 collects the frequencies and amplitudes of the dominant modes in each cluster for all analyzed variables.

The dominant mode for each variable in the breathing mode cluster has a HODMD amplitude that is roughly one order of magnitude larger than the dominant mode amplitude in the ITT cluster, for n, T_e, j_{zi}, and ϕ.

The neutral density n_n displays less modes than the other variables (see Figure 2.6), partly due to the applied filtering. Indeed, only two modes belonging to the breathing dynamics are recovered, while the ITT cluster is missing, since all modes in this frequency range are below the fixed amplitude tolerance. This suggests that, while neutrals play a

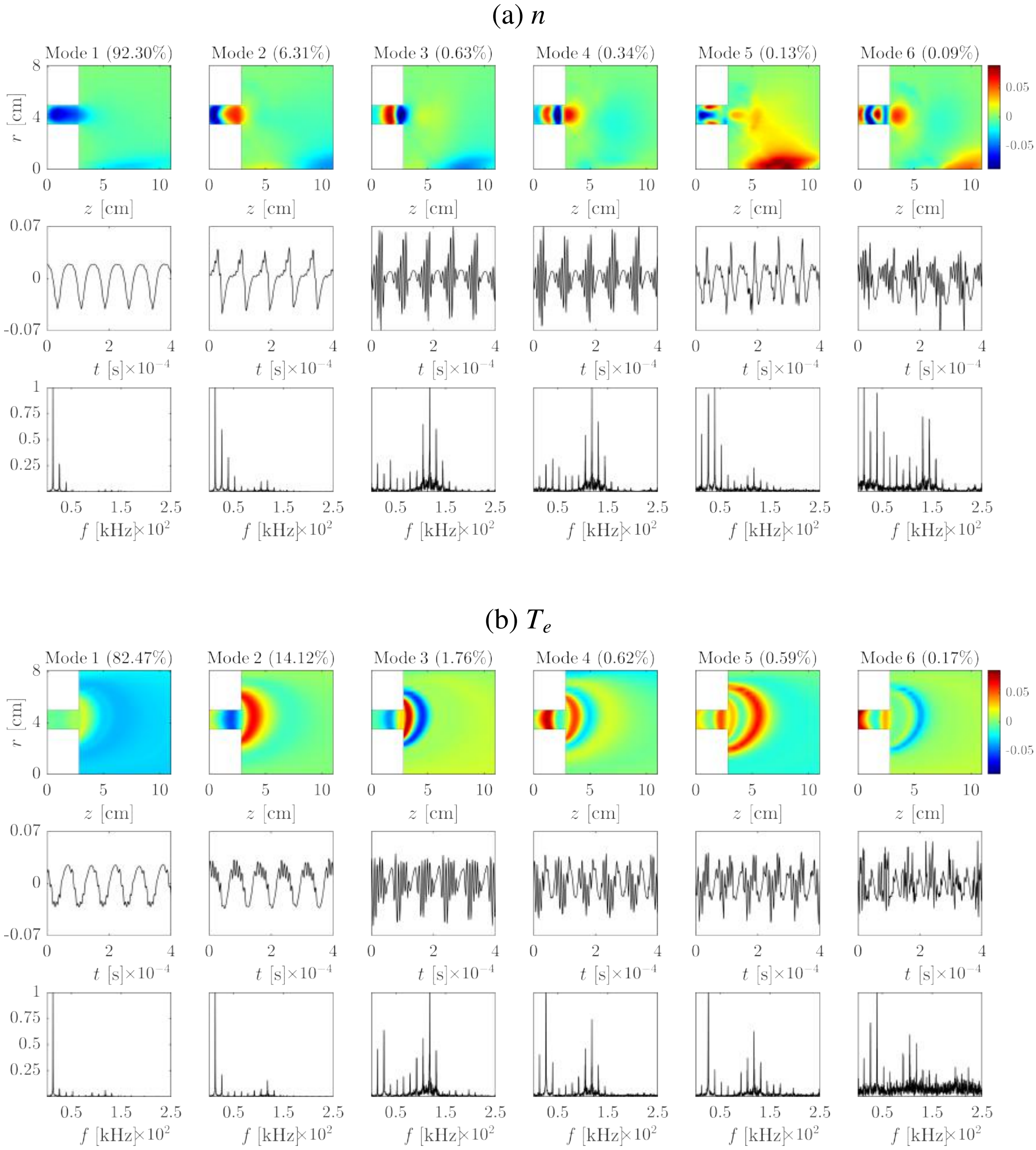

Figure 2.5: Results of POD analysis for (a) plasma density n and (b) electron temperature T_e, in the nominal case. Row 1: dominant spatial POD modes, with the percentage energy content. Row 2: temporal response of the POD modes (i.e., columns of $\boldsymbol{U}$ in equation (2.3)). Row 3: Fourier transform of the mode temporal response.

central role in the breathing mode dynamics, they do not participate much in the ITT oscillations. These findings are in line with the comments in [64], where the spectrum of the ITT dynamics is said to be quite independent of $\dot{m}_A$ at fixed V_d.

There is a chain of larger-amplitude HODMD modes in the breathing cluster that are, within the uncertainty present in the data and the method of analysis, harmonics of the dominant mode, which has the fundamental frequency of the breathing oscillations (namely, 13.1 kHz).

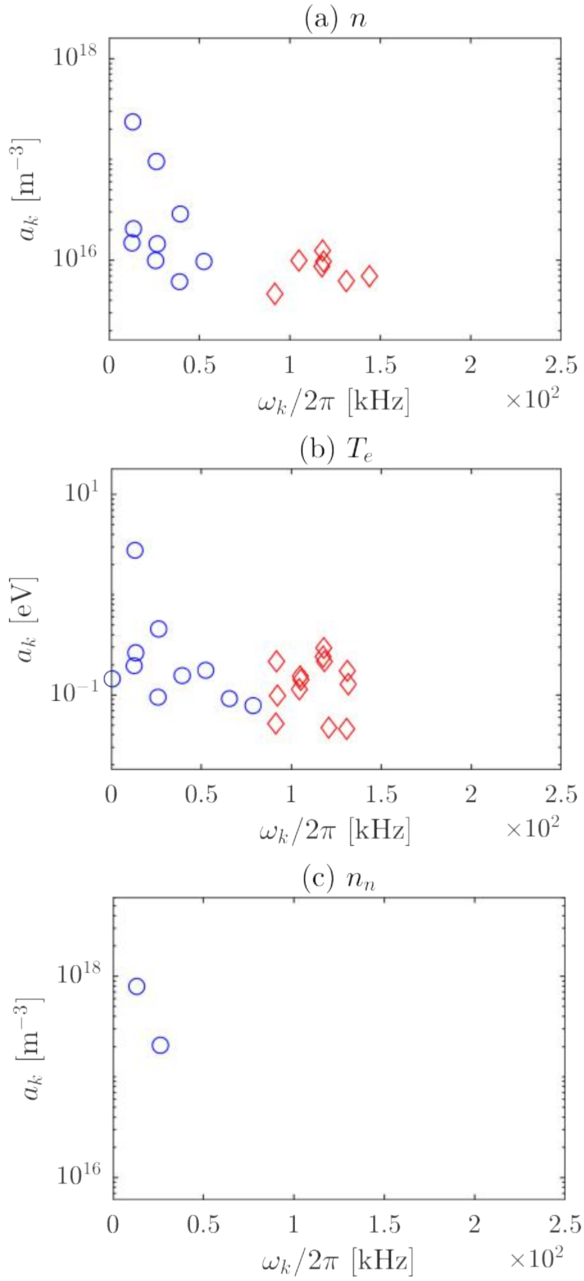

Figure 2.6: HODMD amplitude vs frequency diagrams for (a) plasma density n, (b) electron temperature T_e, and (c) neutral density n_n, in the nominal case. Blue circles refer to modes belonging to the breathing mode cluster (with fundamental frequency 13.1 kHz), while red diamonds refer to modes belonging to the ITT cluster (with fundamental frequency 118 kHz). Ion current density j_{zi} and plasma potential ϕ (not shown) exhibit a similar behavior to n and T_e, respectively.

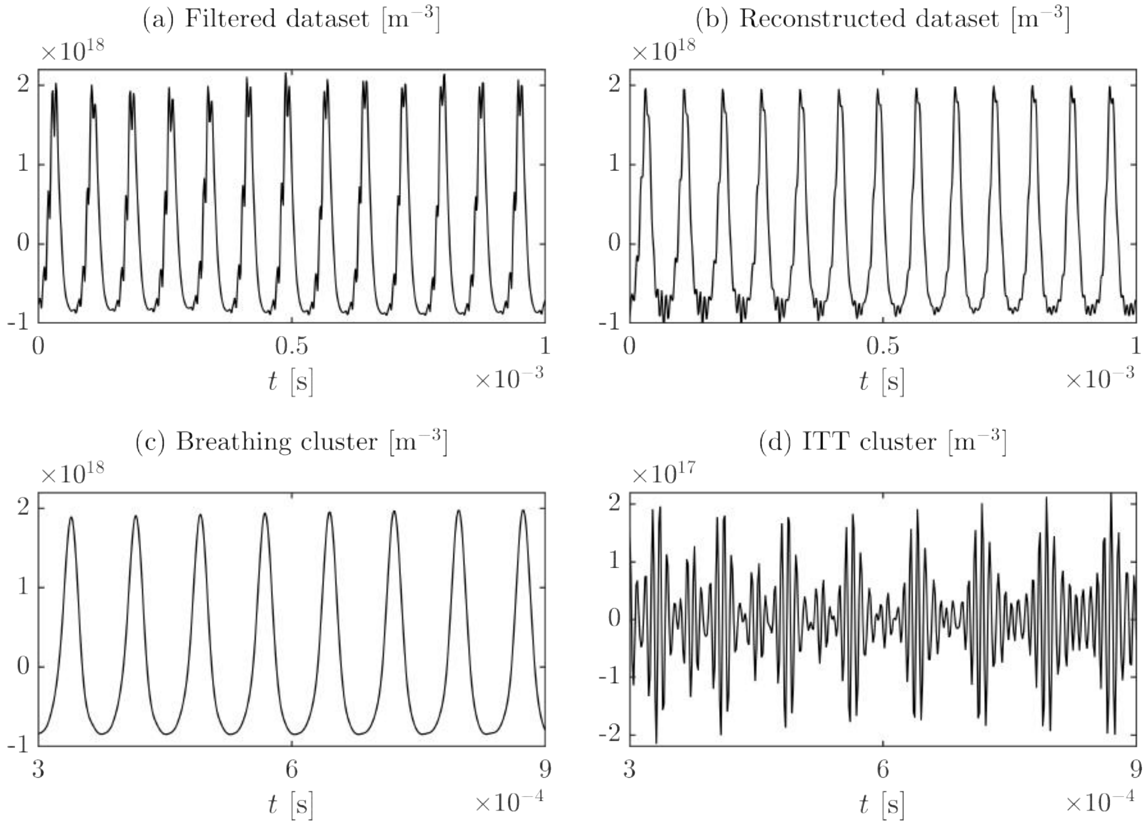

Figure 2.7: Temporal evolution of the plasma density n at $(z, r) = (2.10, 4.16)$ cm. Top plots: comparison between (a) the original data filtered by SVD and (b) the HODMD reconstruction, on the whole timespan τ. Bottom plots: HODMD approximation of the asymptotic dynamics for (c) the breathing mode and (d) the ITT oscillation, over a partial time window.

Besides these larger-amplitude modes, the breathing cluster also exhibits several lower-amplitude modes (roughly one order of magnitude smaller) at similar frequencies. These modes will be labelled here as ‘secondary modes’ for descriptive purposes. Observe that, in the HODMD framework, all terms $\delta_k + i\omega_k$ in equation (2.7) are different. Indeed, secondary modes slightly differ from the dominant ones in both frequency and growth rate. The existence of such secondary modes is seen for all the variables and reveals that the breathing oscillations cannot be reconstructed, within the selected accuracy, by a simple sinusoidal term (or the superposition of sinusoidal harmonics), but they have a richer spectral complexity, requiring these additional contributions.

The ITT cluster, on the other hand, shows a spread spectrum. Three observations can be made. First, in the simulation cases studied in this work, the main frequency in the ITT cluster is non-commensurable with the breathing fundamental frequency. Hence, the presence of two fundamental frequencies suggests that the two types of oscillations correspond to distinct mechanisms. In the nominal case, however, the ITT main frequency is found to be approximately 9 times the breathing mode fundamental frequency, namely 118 kHz. Second, the frequency spacing between the modes in the ITT cluster coincides with the breathing fundamental frequency, meaning that breathing oscillations modulate the ITT oscillations. Third, there are more abundant secondary modes than in the breathing cluster, especially for the electron temperature T_e, revealing a higher spectral complexity.

Relying on the expansion (2.5), the time evolution of each variable can be reconstructed adding together the contributions of all HODMD modes. Figure 2.7 shows the temporal reconstruction of n at $(z, r) = (2.10, 4.16)$ cm as an illustrative example. The comparison between the reconstruction based on all HODMD modes and the original data (after a SVD filtering in order to eliminate noise) highlights the quality of the approximation (cf. top panels). A major advantage of the HODMD technique is the ability to isolate different dynamics and mechanisms. Indeed, it is possible to separately reconstruct the dynamics of n in each cluster, as shown in the bottom panels of Figure 2.7. The breathing oscillations are characterized by periodic wide valleys and narrow peaks. On the other hand, the ITT oscillations feature higher frequencies and show the modulation by the breathing dynamics: the maximum amplitude of the former fast oscillations takes place during the rise of the breathing mode. This behaviour has been also observed in previous numerical studies [128, 148, 160].

Figure 2.8 shows the spatial structure of the dominant HODMD mode in the breathing cluster for each variable, displaying the magnitude of the mode (plots in rows 1–2) and its phase angle (plots in rows 3–4), both in the 2D domain and along the mid-channel $r = 4.16$ cm line. While the magnitude plots allow understanding where the oscillations take place, the phase plots describe their standing or progressive-wave structure and help identifying any phase relation between the variables. Plasma density n, neutral density n_n, and ion current density j_{zi} oscillate strongly and mainly inside the thruster channel, particularly in the ionization region of the HET discharge, where most of the neutral gas flow is ionized and the steady-state maximum of n is located. The length of this region roughly coincides with the characteristic length in which the magnetic field decreases inside the channel, from the exhaust plane to the anode, in agreement with previous works [59]. On the other hand, oscillations of electron temperature T_e and plasma potential ϕ mainly occur outside the channel, in the near plume.

The phase angle plots in Figure 2.8 reveal fundamental behaviors and relations among the variables. On the one hand, n, n_n, and j_{zi} have an essentially constant phase throughout the channel mid-radius line, and therefore they correspond to global oscillations in the whole domain. Additionally, n and j_{zi} oscillations are in phase, exhibiting a phase delay with respect to n_n of about 90°. On the other hand, T_e and ϕ show the same, in-phase, outward progressive-wave structure (i.e., traveling towards the right in the diagrams) in regions inside the channel and immediately outside the thruster, whereas their phase becomes essentially constant in the plume region.

In order to gain further insight into the breathing dynamics, Figure 2.9 displays the temporal evolution of the breathing cluster for plasma density n, neutral density n_n, the

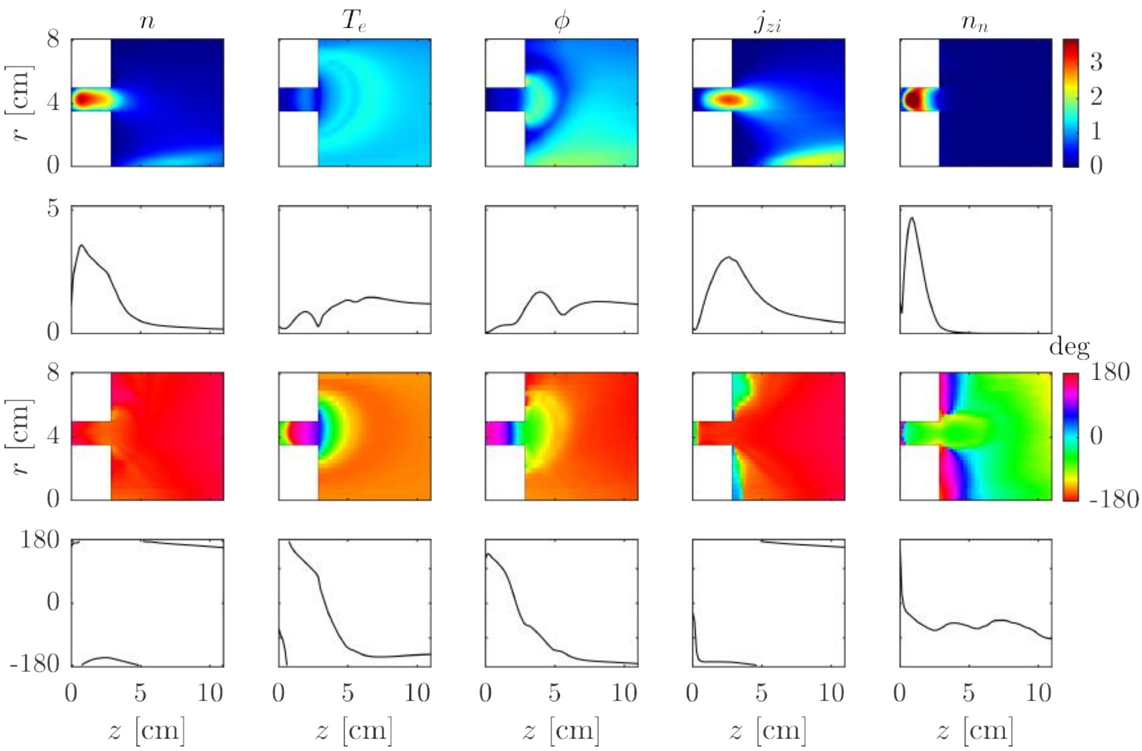

Figure 2.8: Plasma density n, electron temperature T_e, plasma potential ϕ, ion current density j_{zi}, and neutral density n_n in terms of the dominant HODMD spatial mode in the breathing mode cluster (with frequency 13.1 kHz), for the nominal case. Row 1: mode magnitude in the 2D domain. Row 2: mode magnitude along the $r = 4.16$ cm line. Row 3: mode phase angle in the 2D domain. Row 4: mode phase angle along the $r = 4.16$ cm line. Note that magnitudes are displayed in arbitrary units.

ionization production term $S_{ion} = n\,\nu_{ion}$ (where ν_{ion} is the total ionization frequency), the axial electric field $E_z = -\partial\phi/\partial z$, and electron temperature T_e, at the central point in the discharge channel $(z, r) = (2.10, 4.16)$ cm, highlighted in Figure 2.1(a). The amplitude of each variable is normalized by its time-averaged value at the spatial point of analysis. The breathing oscillations begin with an increase of the neutral density in the chamber. This larger availability of neutrals results in a growth of the ionization rate, followed by an increase of the plasma density. Eventually, neutrals are depleted: their density n_n goes down and the plasma density n peaks. The larger amount of plasma in the channel drives then an increase of the axial electric field E_z, which helps evacuating it, and the plasma density n finally returns to its initial level. This cycle repeats, which is consistent with the predator-prey models of the breathing mode [68]. It is noted that the oscillations of the electron temperature T_e follow the shape of those of E_z. This is explained by the greater Joule heating experienced by the electrons when E_z is large, which is accompanied by a higher Hall current in the $\boldsymbol{E} \times \boldsymbol{B}$ direction and a larger axial current.

In a similar fashion to Figure 2.8, Figure 2.10 displays the dominant HODMD mode in the ITT cluster, evidencing a different behavior compared to the breathing mode. As previously mentioned, the weaker ITT oscillations are related to the ion residence char-

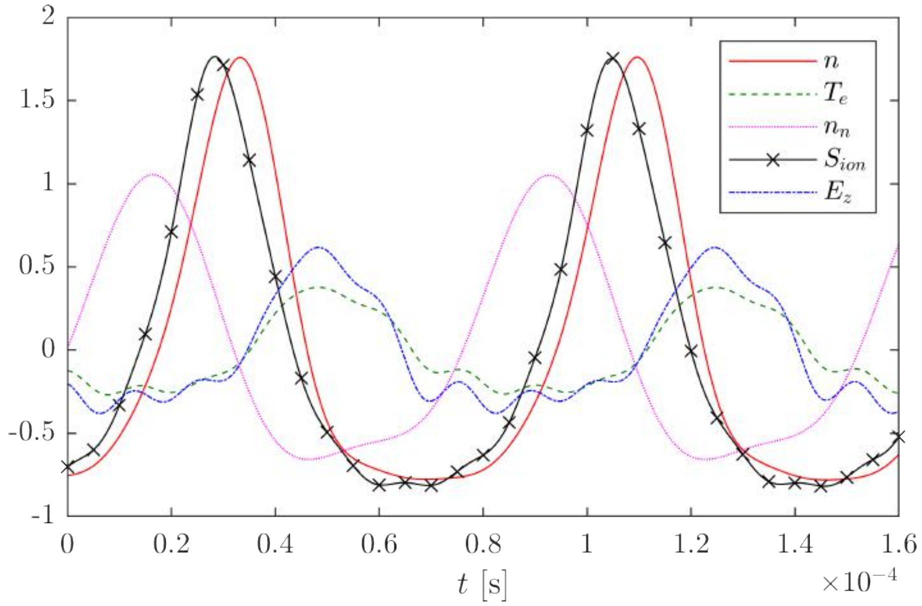

Figure 2.9: Breathing mode evolution reconstruction in the nominal case for different variables, plotted at $(z, r) = (2.10, 4.16)$ cm and normalized by the time-averaged values at the same point in space. Lines show plasma density n (red solid), neutral density n_n (magenta dotted), axial electric field E_z (blue dot-dashed), electron temperature T_e (green dashed), and the ionization production term S_{ion} (black crossed).

acteristic timescale $\tau_i = L/u_{zi}$, where L is the channel length. Computing the mean ion velocity $u_{zi} \simeq 14971$ m/s, the value $1/\tau_i = 129$ kHz is found, which is in good agreement with the frequency of the dominant HODMD mode in the ITT cluster, namely 118 kHz. In this cluster, all variables have a progressive-wave structure in most of the domain.

The following observations can be made. Firstly, the oscillations of T_e and ϕ mainly take place in the neighborhood of the thruster exit, further downstream than where the oscillation peak of the plasma density occurs for the breathing mode. This is where $\boldsymbol{B}$ and $\boldsymbol{E}$ are higher, characterizing the acceleration region of a HET discharge [59]. This is also reported in the hybrid simulations of [160]. Both variables have a clear progressive-wave structure in this region, with a wavelength comparable to the channel length, smaller than for the breathing mode. The electron temperature T_e displays two maxima in the magnitude along the channel mid-line and a near-flat phase angle in the plume region, beyond the cathode magnetic line.

Secondly, while j_{zi} mainly oscillates in the plume region, the peak of n takes place inside the channel (but, incidentally, closer to the exit than for the breathing mode). Indeed, the oscillations of j_{zi} are due to those of the ion velocity u_{zi} taking place outside the device. These oscillations are linked to the traveling oscillations of ϕ near the exit of the thruster reported above, which results in the periodic motion of the acceleration region where the axial electric field is maximum. In addition, it can be observed that there is a second peak in the oscillation of j_{zi}, corresponding to the position where the magnitude of n is large. Indeed, the oscillations of j_{zi} inside the channel have a different behavior from

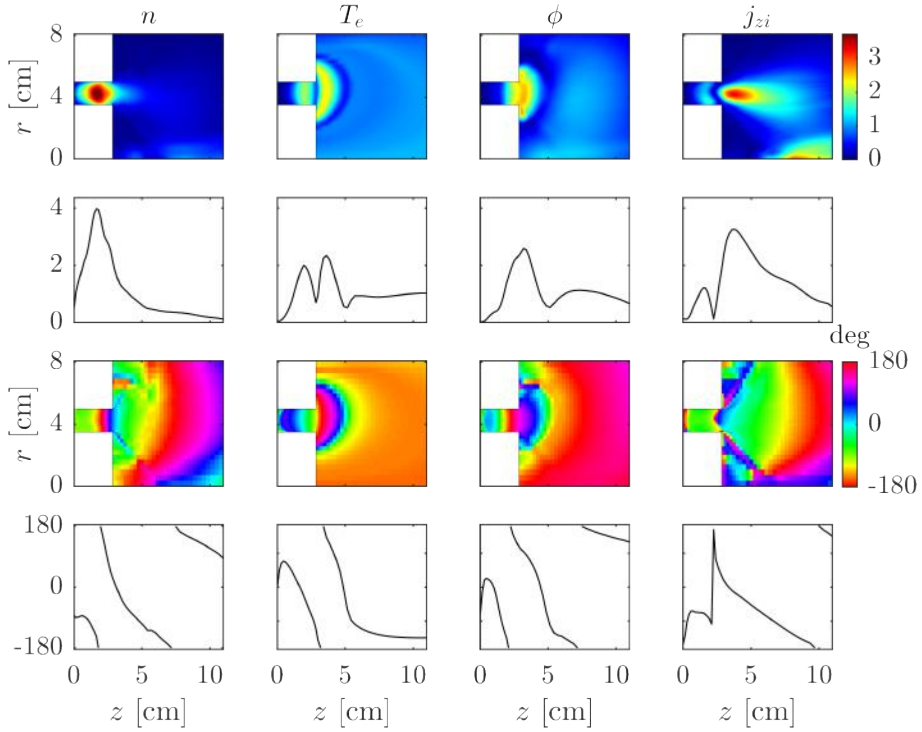

Figure 2.10: Counterpart of Figure 2.8 for plasma density n, electron temperature T_e, plasma potential ϕ, and ion current density j_{zi} in terms of the dominant HODMD spatial mode in the ITT cluster (with frequency 118 kHz), for the nominal case.

the ones outside the channel, with a dominant standing-wave character, and are separated from the outside by a line of nodes in the magnitude plot and a 180° phase shift near the channel exit. It is noted that the characteristic phase velocity in the acceleration region of these waves is 13723 m/s for the plasma density and 15809 m/s for the ion current density, which is in good correspondence with the mean ion velocity u_{zi} indicated above.

As a side note, it is worth observing that while Figures 2.8 and 2.10 show only the dominant mode in each cluster, the behavior of the remaining modes follows the same trends, in terms of type of wave structure and location of the magnitude peaks, providing additional physical arguments for the separation of the two groups. This is also true in the off-nominal simulations reported in the next section of this paper.

In order to better describe the dynamics of the ITT oscillations, which have a richer spectral complexity than breathing oscillations, Figure 2.11 displays the ITT mode spatial reconstruction for some plasma variables in the midline of the channel at four time instants of its cycle. The oscillations originate near the anode and propagate outward into the channel and the near plume. An increase of plasma density n originating near the anode is followed by an increase of the axial electric field E_z. The evolution of the ion velocity u_{zi} is mainly the result of two phenomena: advection and acceleration due to E_z. **As the E_z perturbations travel downstream, separation of slow and fast ions occurs. With this process, ITT oscillations contribute to increase the velocity dispersion of ions in the plume. Subsequently, fast and slow ions tend to bunch together further downstream**

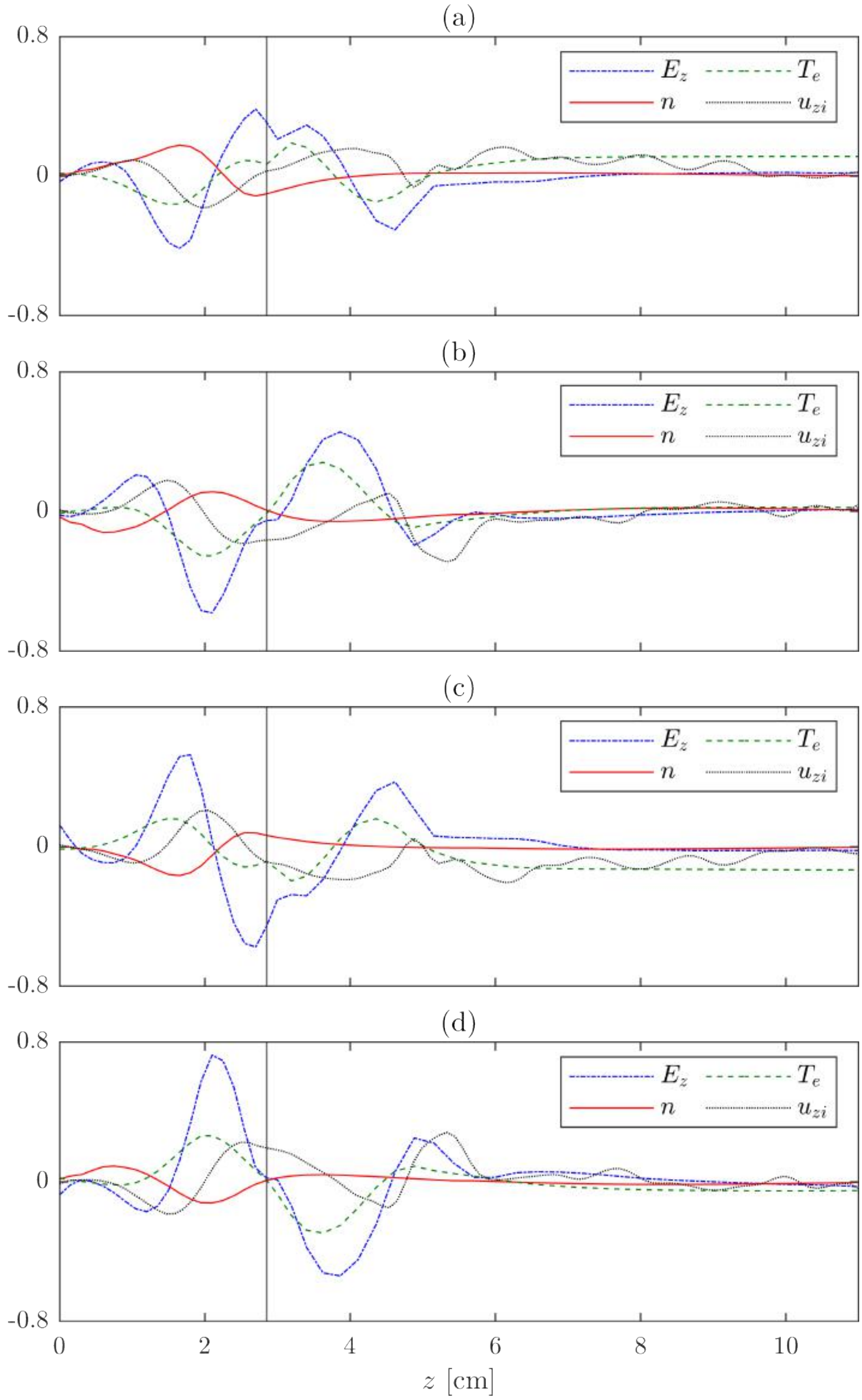

Figure 2.11: ITT mode spatial reconstruction in the nominal case for different variables, plotted along the centreline at $z = 4.16$ cm and normalized by the time-averaged values at the spatial point $(z, r) = (2.10, 4.16)$ cm. The plots depict four different phase instants of the ITT dynamics evolution, at (a) 25%, (b) 50%, (c) 75%, and (d) 100% of its period, which is approximately 8.5 μs. Lines show plasma density n (red solid), axial electric field E_z (blue dot-dashed), electron temperature T_e (green dashed), and single ions axial velocity u_{zi} (black dotted), whereas the vertical line represents the chamber exit.

in the plume region due to their different velocities. This behavior is in agreement with the results in [148] and with the observations made in [72], where a short-wave asymptotic analysis showed that the total ion velocity perturbation can be expressed as the sum of a standing and a traveling wave, the former weaker than the latter. Finally, it is noted that electron temperature T_e is essentially in phase with the axial electric field E_z, suggesting the same relative behavior as in the breathing oscillations.

2.3.2 Off-nominal cases

In the first off-nominal simulation case, with discharge voltage V_d = 200 V, the mean discharge current decreases from $\overline{I}_d$ = 5.99 A to 5.23 A, while the mean plasma density sees an increment from $\overline{n}$ = 1.90 · 10^{17} m^{-3} to 2.17 · 10^{17} m^{-3}. The amplitude of their oscillations is now smaller and roughly equal to said mean values, rather than about three times as in the nominal case. This trend for V_d is consistent with the observations of previous studies [66, 148, 160, 161]. As the breathing mode amplitude essentially corresponds to the discharge current amplitude, the strength of the former is expected to decrease when lowering the discharge voltage. Indeed, this is what the analysis shows.

The POD modes for the low voltage case (not shown) reproduce the general behavior described for the nominal case, although now even the first, most energetic POD modes exhibit a mixture of frequencies belonging to both the breathing and ITT parts of the spectrum. This already suggests the loss of dominance of the breathing mode and that both types of oscillations have a similar energy content. As before, it also manifests the limitations of the POD technique in successfully separating the different oscillation mechanisms.

Figure 2.12 shows the diagrams of amplitude vs frequency extracted by means of the iterative HODMD method, while Table 2.3 reports the frequencies and amplitudes of the dominant modes in each cluster. Variables n, T_e, n_n, j_{zi}, and ϕ exhibit behaviors comparable to those observed in the nominal case. In addition, the spatial structure of the involved HODMD modes is qualitatively similar. The breathing mode fundamental frequency is now equal to 10.8 kHz, while the ITT mode fundamental frequency is 112 kHz. One of the major differences stems from the lower amplitudes in the breathing mode cluster, which are now comparable to the ITT amplitudes, in agreement with the above. The two fundamental frequencies are more markedly non-commensurable, compared to the nominal case.

Comparatively, only one harmonic of the dominant mode is retained in the breathing cluster for n and T_e, together with some secondary modes. On the other hand, in the ITT cluster of these variables, a new harmonic group is recovered in the 200–250 kHz range, which was absent in the nominal simulation case, while the number of secondary modes also increases. The existence of more secondary modes suggests that the oscillations are more complicated (i.e., they exhibit higher spectral complexity). Lastly, the neutral density n_n also participates in the ITT oscillations with a single small-amplitude mode. As

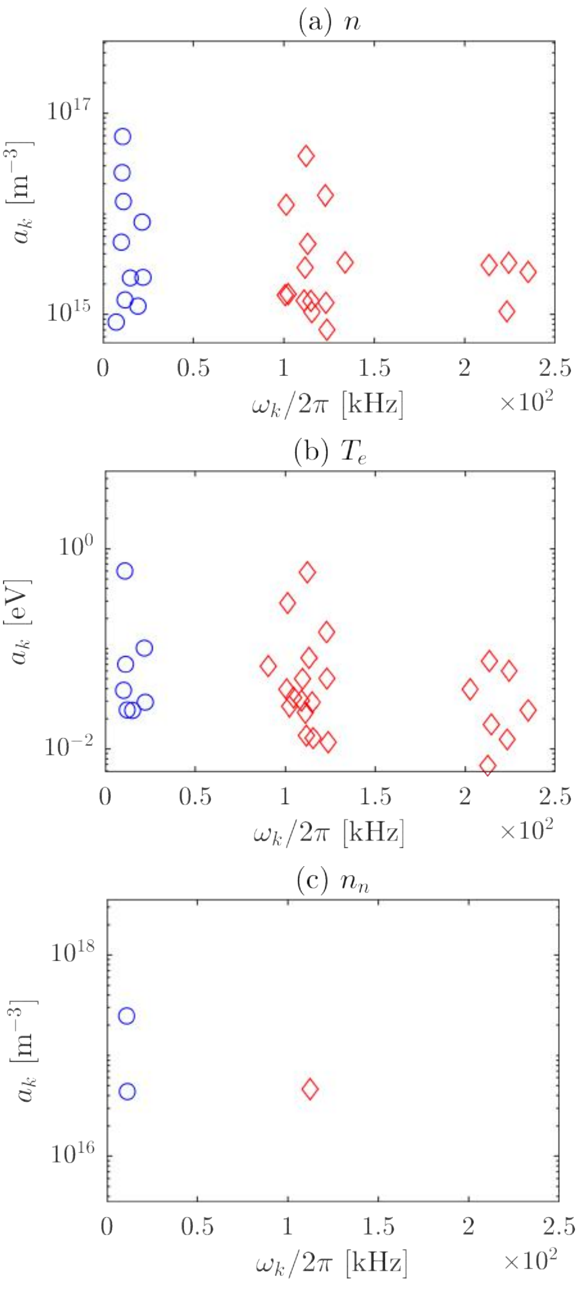

Figure 2.12: Counterpart of Figure 2.6 for the low voltage, off-nominal case, with V_d = 200 V and $\dot{m}_A$ = 5 mg/s. Blue circles refer to modes belonging to the breathing mode cluster (with fundamental frequency 10.8 kHz), while red diamonds refer to modes belonging to the ITT cluster (with fundamental frequency 112 kHz). Ion current density j_{zi} and plasma potential ϕ (not shown) exhibit a similar behavior to n and T_e, respectively.

	n [m^{-3}]	T_e [eV]	ϕ [V]	j_{zi} [A m^{-2}]	n_n [m^{-3}]
Breathing dominant mode (10.8 kHz)	$5.88 \cdot 10^{16}$	0.60	1.74	71.0	$2.47 \cdot 10^{17}$
ITT dominant mode (112 kHz)	$3.75 \cdot 10^{16}$	0.58	3.10	21.7	$4.63 \cdot 10^{16}$

Table 2.3: Summary of frequencies and amplitudes of the dominant HODMD modes in the two dynamics clusters, for all analyzed variables in the low voltage case.

noted before, this does not occur in the nominal case and it still agrees with the fact that the role of n_n on these oscillations is almost negligible. The reconstructed ITT oscillations are again modulated by the breathing frequency, albeit this modulation is weaker than in the nominal case. This is seen in Figure 2.13. Indeed, the ITT peaks are now out of phase with respect to the breathing ones and their magnitude is less significant than in the nominal case. The breathing and ITT oscillation amplitudes are finally comparable with each other, as previously mentioned.

In the high mass flow rate simulation case, with $\dot{m}_A = 6$ mg/s, the mean discharge current and the mean plasma density increase to $\overline{I}_d = 7.23$ A and $\overline{n} = 2.25 \cdot 10^{17}$ m^{-3}, respectively. It is observed that essentially the same amplitude of breathing oscillations as in the nominal case exists in the discharge current. In the POD analysis (not shown), again the first two POD modes are dominated by the breathing mode fundamental frequency and the subsequent two modes by the ITT mode fundamental frequency, indicating a similar relative energy content of the two oscillation types as in the nominal case.

Figure 2.14 displays the HODMD results. The breathing mode and ITT mode dominant frequencies are 13.4 kHz and 121 kHz, respectively, while the amplitude of the oscillations mildly increases with respect to the nominal case. Table 2.4 reports the frequencies and amplitudes associated with the dominant HODMD modes for both clusters and all the variables under study. A similar number of breathing mode harmonics as in Figure 2.6 is extracted, but with no secondary modes. This hints at a spectrally simpler oscillation, which can be described as a superposition of a lower number of complex exponentials (cf. expansion (2.5)). The ITT cluster spectrum is again broad and also loses its secondary modes, but the same comments apply. The frequency spacing between the ITT modes matches well the breathing mode fundamental frequency, showing a large modulation by the latter. This is also observed upon reconstructing the ITT oscillations, as shown in Figure 2.15. Finally, no n_n modes are recovered in the ITT group, as in the nominal simulation case.

The spatial structure of the HODMD modes in each cluster is qualitatively similar to the nominal case. Hence, it can be concluded that the trend of increasing the mass flow rate, at least in the studied range, is to result in a cleaner, simpler mode solution for both the breathing and ITT oscillations, but otherwise it does not drastically modify any of the two mechanisms.

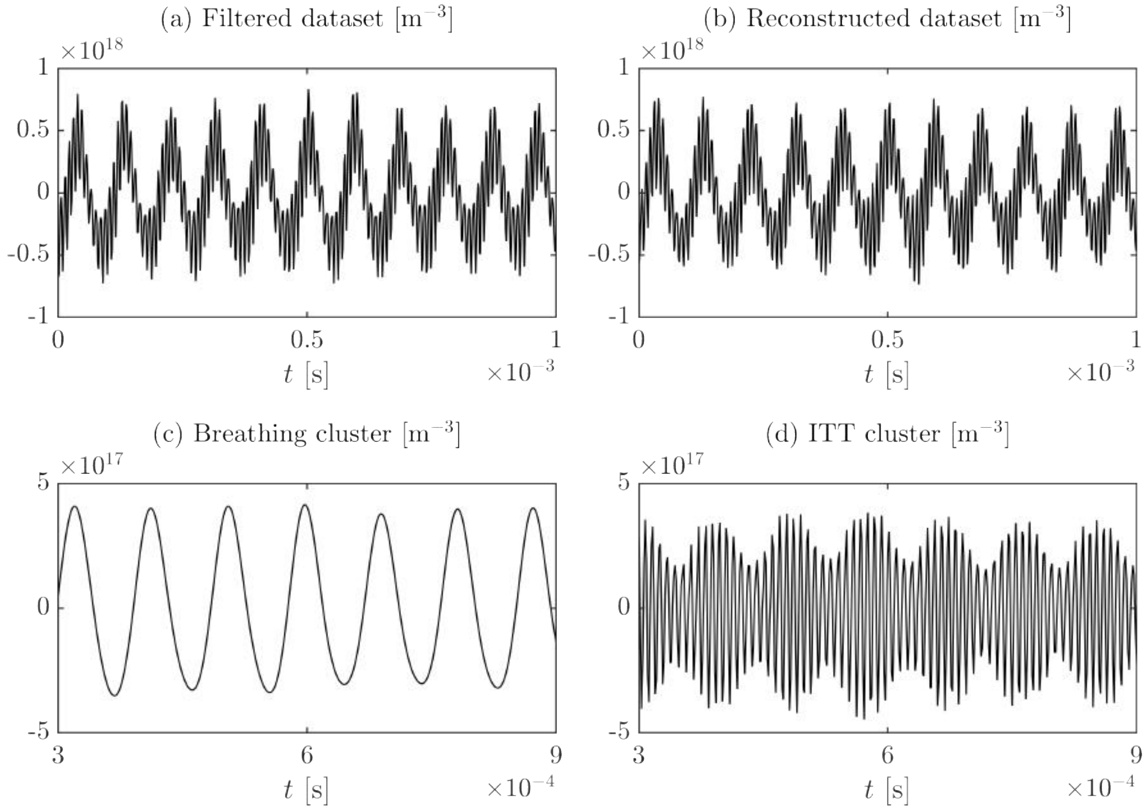

Figure 2.13: Counterpart of Figure 2.7 for the low voltage, off-nominal case, with $V_d = 200$ V and $\dot{m}_A = 5$ mg/s, for plasma density n at $(z, r) = (2.10, 4.16)$ cm. Top plots: comparison between (a) the original data filtered by SVD and (b) the HODMD reconstruction, on the whole timespan τ. Bottom plots: HODMD approximation of the asymptotic dynamics for (c) the breathing mode and (d) the ITT oscillation, over a partial time window.

2.4 Conclusions

Low-frequency axial-radial oscillations in the plume of a SPT-100-like HET have been investigated by means of data-driven techniques, namely POD and HODMD, relying on the simulation data of a 2D axisymmetric hybrid PIC/fluid code (HYPHEN-HET).

Application of POD yields an energy-based decomposition of the data, useful for noise filtering and dimensionality reduction. However, this technique is unable to isolate the dynamics of different oscillation mechanisms present in the HET discharge, especially due to the mix of frequencies associated to each POD mode. HODMD, on the other hand, achieves this separation by representing the spatio-temporal data as a superposition of single-frequency, non-orthogonal, dynamically relevant modes. The HODMD method goes beyond standard DMD in the study of nonlinear systems, by enlarging the coordinate space using time-lagged snapshots. Iterations of the method are used to further filter out irrelevant modes.

The analysis permitted isolating and reconstructing the breathing mode dynamics,

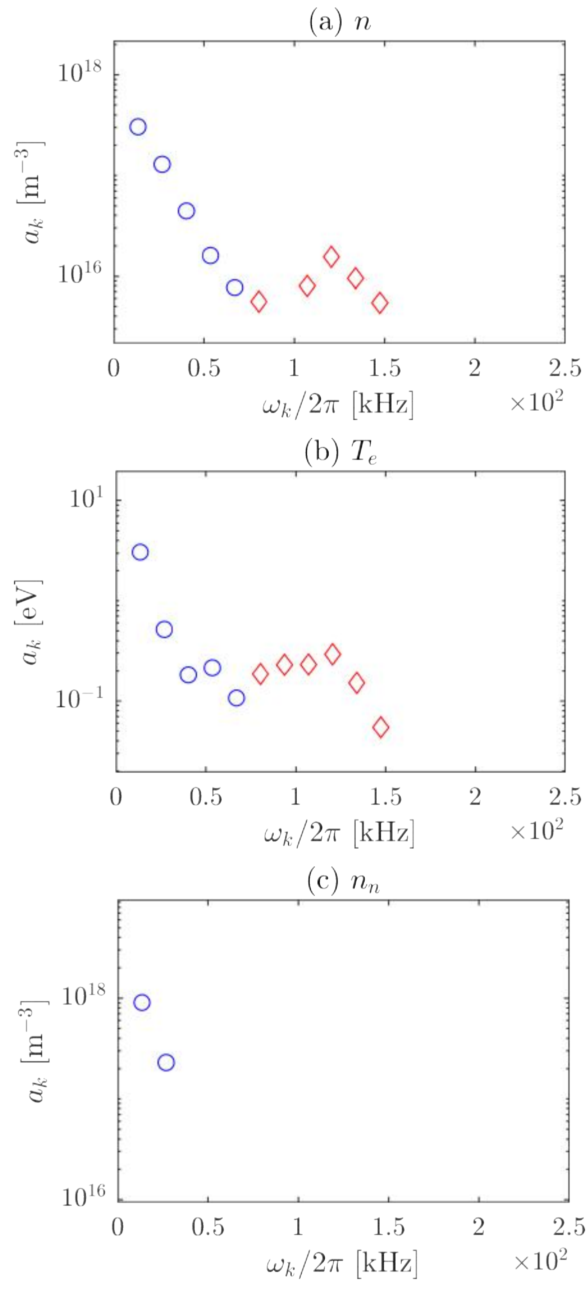

Figure 2.14: Counterpart of Figure 2.6 for the high mass flow rate, off-nominal case, with V_d = 300 V and $\dot{m}_A$ = 6 mg/s. Blue circles refer to modes belonging to the breathing mode cluster (with fundamental frequency 13.4 kHz), while red diamonds refer to modes belonging to the ITT cluster (with fundamental frequency 121 kHz). Ion current density j_{zi} and plasma potential ϕ (not shown) exhibit a similar behavior to n and T_e, respectively.

	n [m^{-3}]	T_e [eV]	ϕ [V]	j_{zi} [A m^{-2}]	n_n [m^{-3}]
Breathing dominant mode (13.4 kHz)	$3.05 \cdot 10^{17}$	3.06	12.5	318	$9.05 \cdot 10^{17}$
ITT dominant mode (121 kHz)	$1.56 \cdot 10^{16}$	0.29	1.07	8.50	-

Table 2.4: Summary of frequencies and amplitudes of the dominant HODMD modes in the two dynamics clusters, for all analyzed variables in the high mass flow rate case.

observing strong global oscillations, and a phase difference between the plasma density and the neutral density inside the channel. In addition, it provides an estimate of the noise level in the simulation data, thus enabling to filter out numerical errors and uncover physical phenomena masked by spurious perturbations. The electron temperature and the plasma potential show a progressive-wave structure. The HODMD spectrum reveals a cluster of components that are harmonics of the breathing mode fundamental frequency. Results agree well with the predictions of predator-prey models and existing results. In addition, weaker, higher-frequency oscillations are found in the ITT range, corresponding to the ion residence time in the acceleration region of the thruster. These oscillations exhibit an axial progressive-wave structure for all variables, except for the neutral density that is essentially not excited by them and does not play an important role in their physics. The phase velocity of these traveling waves corresponds well with the average ion velocity in the acceleration region.

The effect of varying the thruster operating point has also been investigated. The major effect of changing the discharge voltage or the anode mass flow rate is to modify the dominant frequencies of the two oscillation types. By decreasing the discharge voltage, the amplitude of the breathing oscillations weakens and becomes comparable to that of the ITT dynamics. More modes are retained by the HODMD algorithm, resulting in more complicated oscillations. Increasing the mass flow rate, on the contrary, lowers the number of modes needed to model them, and therefore suggests spectrally simpler oscillations. Otherwise, the spatial structure of the involved HODMD modes and the overall behavior of the discharge remain qualitatively the same in the explored parameter ranges.

This work illustrates the significance of modal analysis techniques, like HODMD, for the isolation and analysis of different oscillation mechanisms in plasma flows relevant to electric propulsion. The main advantage of HODMD is that every characteristic oscillation is decomposed into (a superposition of) modes with one single frequency, growth rate and amplitude each, allowing to separate the different dynamics present in the data. In addition, as our parametric analysis has shown, given several datasets at different thruster operating points, it is possible to identify trends for the frequency, the amplitude, and the behavior of the underlying oscillations. While the source of the data has been numerical in the present work, we expect this technique to be equally applicable to experimental

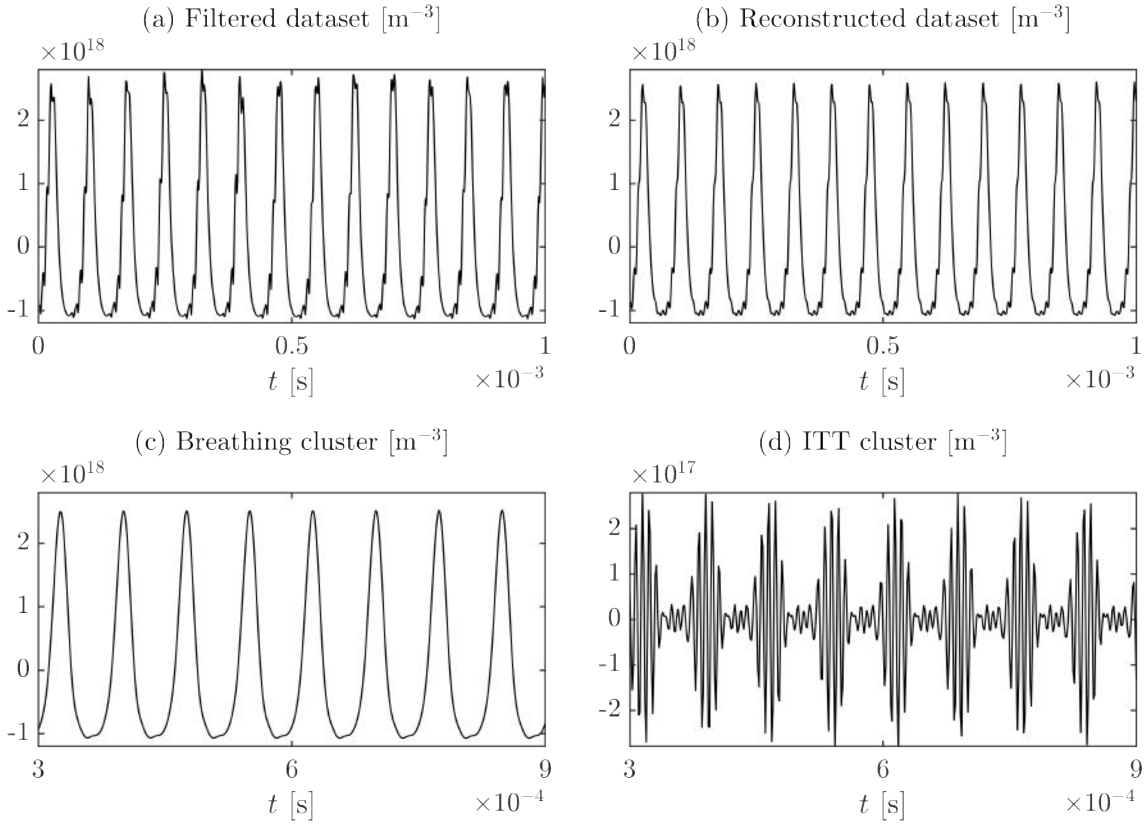

Figure 2.15: Counterpart of Figure 2.7 for the high mass flow rate, off-nominal case, with $V_d = 300$ V and $\dot{m}_A = 6$ mg/s, for plasma density n at $(z, r) = (2.10, 4.16)$ cm. Top plots: comparison between (a) the original data filtered by SVD and (b) the HODMD reconstruction, on the whole timespan τ. Bottom plots: HODMD approximation of the asymptotic dynamics for (c) the breathing mode and (d) the ITT oscillation, over a partial time window.

measurements (from, e.g., plasma probes), provided that their spatial and time resolution is sufficient.

3. EXPERIMENTAL CHARACTERIZATION OF LOW-FREQUENCY FLUCTUATIONS IN THE MAGNETIC NOZZLE OF A HELICON PLASMA THRUSTER

In this chapter, oscillations within the Magnetic Nozzle (MN) of a Helicon Plasma Thruster (HPT) ≤ 1 MHz are experimentally characterized. The experimental setup employs an array of electrically floating Langmuir Probes (LPs) strategically displaced in space to resolve the wavevector components of the waves along the azimuthal and parallel directions relative to the magnetic field. The LPs are displaced at various positions in the plume employing a remotely controlled mechanical arm, and data is collected for two different mass flow rate conditions. The wavevector components are recovered through a custom-made version of the Two-Points Power Spectral Density (PSD2P) technique, employing coherence analysis to assess the consistency of the phase difference between two LP signals. A very low-frequency, global oscillation mode is detected around $\simeq 4$ kHz, attributed to an ionization instability in the source, while a broadband, low-coherence, essentially-azimuthal, ion-acoustic-like spectrum is visible at < 200 kHz. A mild peak of larger coherence is superposed to the broadband spectrum at $\simeq 50$ kHz, followed by a weak secondary peak at $\simeq 100$ kHz at some locations. A bi-coherence analysis discards any nonlinear interactions within the < 1 MHz band. However, significant coupling is found between the broadband fluctuations and the driving frequency of 13.56 MHz, which suggests the former are likely the result of a parametric decay instability. By computing time-averaged plasma variables, it is found that the broadband azimuthally-propagating spectrum possesses phase velocities in the same order of magnitude as the ion sound velocity.

This chapter represents a transcription of the following journal paper (without the introduction section):

- **Maddaloni D.**, Bayón-Buján B., Navarro-Cavallé J., Terragni F., Merino M., "Experimental characterization of low-frequency fluctuations in the magnetic nozzle of a Helicon Plasma Thruster". Plasma Sources Science and Technology. (submitted)

The Ph.D candidate carried out the development of the LPs and the collection of the experimental data. Additionally, they implemented and adapted the PSD2P algorithm and the coherence estimate, while also fundamentally contributing to the data interpretation and analysis. The candidate also undertook the initial drafting of the manuscript.

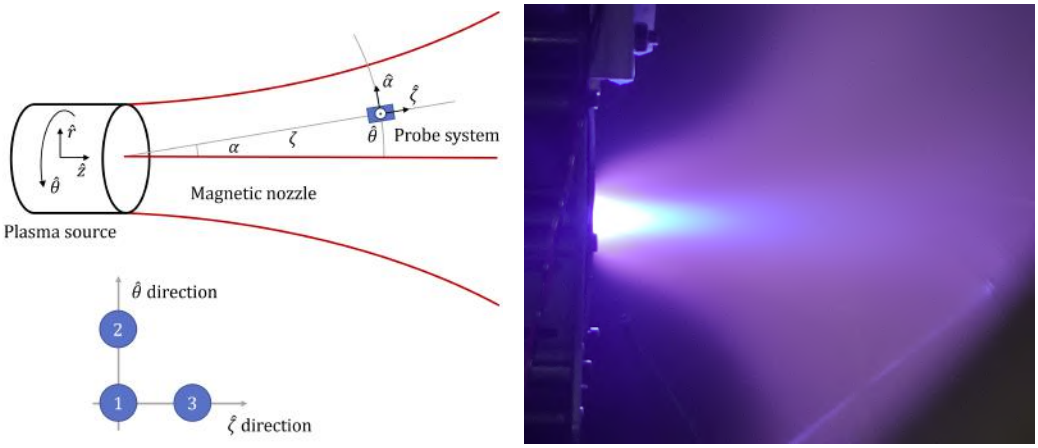

Figure 3.1: Sketch of the HPT source (in black) and its MN (in red), shown on the left. The probe system is represented with a blue rectangle and consists of three cylindrical probes. The *reference probe* (1) is placed at the origin of the probe system reference frame ($\hat{\boldsymbol{\zeta}}, \hat{\boldsymbol{\alpha}}, \hat{\boldsymbol{\theta}}$), with polar coordinates (ζ, α) from the source exit center point. Probes (2) and (3) are displaced 10 mm along $\hat{\boldsymbol{\theta}}$ and $\hat{\boldsymbol{\zeta}}$ directions, respectively, as shown on the right. The cylindrical reference frame ($\hat{\boldsymbol{z}}, \hat{\boldsymbol{r}}, \hat{\boldsymbol{\theta}}$) for the plasma source is also shown. On the right, a picture of the HPT device firing during the experiments.

3.1 Experimental setup

The test article is the HPT prototype described and partly characterized in [162] using LIF technique. This device consists of a cylindrical source made of a quartz tube with a 25 mm inner diameter and a 140 mm length, a half-turn helical antenna excited with 300 W of radio-frequency power at 13.56 MHz, and a set of permanent magnets made of neodymium and radially polarized. The magnetic field strength is about 750 G at the exit of the source, while a power of 300 W is injected using a radiofrequency Helicon signal at 13.56 MHz. Note that in the MN of this prototype [162], the magnetic vector field $\boldsymbol{B}$ points backward (i.e., toward the source). The device was operated with xenon at two different mass flow rates, namely at $\dot{m} = 5$ and 10 sccm (1 sccm $\simeq$ 0.1 mg/s for xenon). Most of the results refer to the first operating condition, namely $\dot{m} = 5$ sccm. All the experiments have been completed at the EP2-UC3M experimental facilities, in a 3.5 m long and 1.5 m in diameter vacuum chamber, equipped with cryopanels and turbomolecular pumps enabling a background pressure of 2×10^{-5} mbar at 20 sccm xenon and below 10^{-5} mbar at 5 sccm xenon.

The diagnostics setup consists of an array of three identical, cylindrical Langmuir probes (LPs), mounted on a probe system that can be translated and rotated in the polar directions ζ and α, respectively, as shown in Figure **??**. Each probe is made of a tungsten rod tip 4 mm long and 0.25 mm in radius, and an alumina tube body. The probe signals are brought outside of the chamber using coaxial connectors, cables, and feedthroughs to minimize noise pickup in the setup. The *reference probe*, labeled as probe (1), is placed at the origin of the probe system reference frame ($\hat{\boldsymbol{\zeta}}, \hat{\boldsymbol{\alpha}}, \hat{\boldsymbol{\theta}}$), with polar coordinates (ζ, α)

from the source exit center point. Probes (2) and (3) are placed 10 mm along $\hat{\boldsymbol{\theta}}$ and $\hat{\boldsymbol{\zeta}}$ directions, respectively.

For the $\dot{m} = 5$ sccm operating condition, three axial positions were scanned at $\zeta = 50$, 100, and 150 mm. On the other hand, while ζ was fixed, the angle α was varied from 0 to 50 deg. These measurement points are represented in Figure 3.2. A smaller dataset was acquired for the other mass flow rate condition, $\dot{m} = 10$ sccm. Note that the direction $\hat{\boldsymbol{\zeta}}$ approximately coincides with the direction of $-\boldsymbol{B}$ in the MN, whose magnitude is also displayed in Figure 3.2. The maximum deviation between $\hat{\boldsymbol{\zeta}}$ and $-\boldsymbol{B}$ is always below 4 deg at the measurement points.

The main set of measurements was obtained with the three LPs in the floating regime, synchronously sampling with an AC-coupled Yokogawa DLM5058 Mixed Signal Oscilloscope, resolving frequencies up to 50 MHz. This allowed to resolve the characteristic Helicon frequency alongside its first harmonics. The oscilloscope provides 8 bits of vertical resolution, 2.5 GSa/s of sampling rate, and 250 MHz of bandwidth. Three samples of 500 ms length each were acquired at each inspected location. After inspection of the spectrogram, the acquired signals are considered to be stationary over the sampled timespan. The floating potential oscillations are used as a proxy for the plasma potential fluctuations under the assumption of approximately isothermal electrons over that timescale [47, 49, 73, 132].

Alongside time-resolved measurements, the I–V characteristics from the (uncompensated) reference probe were also collected in order to estimate the time-averaged plasma density n, plasma potential ϕ_p, electron temperature T_e, and all their gradients. To this end, the I–V curves were postprocessed following the procedure detailed in [163]. The axial distances scanned for these acquisitions are the same as for the time-resolved ones, namely $\zeta = 50$, 100, and 150 mm, but the angular positions are fewer. In particular, for each distance, the scanned angles are $\alpha = 0$, 7, 15, and 30 deg.

3.2 Time-resolved data analysis

To characterize the electrostatic fluctuations at each measurement point, we first subdivide the total measurement timespan of 1500 ms into $N_w = 600$ non-overlapping windows of 2.5 ms, with $N_s = 2.5 \times 10^5$ samples each, and then compute the (N_s-normalized) discrete Fourier transform of the floating potential $\phi_{i,n}(t)$ of each probe i on each window n, $\psi_{i,n}(f)$, for $i = 1, 2, 3$ and $n = 1, \ldots, N_w$ (here, f is the linear frequency), as

$$\psi_{i,n}(k\Delta f) = \frac{1}{N_s} \sum_{j=0}^{N_s-1} \phi_{i,n}(j\Delta t) \exp(-\mathrm{i}2\pi jk/N_s), \quad \text{for } k = 0, \ldots, N_s - 1, \tag{3.1}$$

where $\Delta t = 0.01$ µs is the time step for the signal sampling and $\Delta f = 1/(N_s \Delta t)$ is the resolvable frequency. The power spectral density at probe i (P_{ii}), the cross spectral density among two probes i and j (P_{ij}), and the corresponding unit magnitude-squared coherence

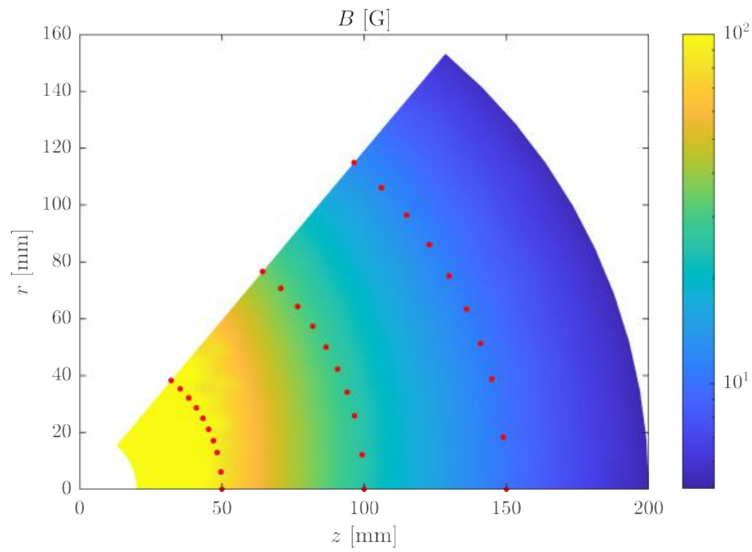

Figure 3.2: Measured magnitude of the applied magnetic field in the MN. The magnetic vector field $\boldsymbol{B}$ points toward the source in this setup. The red dots indicate the points in the plume at which time-resolved measurements were carried out.

(R^2_{ij}) are computed by averaging over the windows, as

$$P_{ii}(f) = \frac{1}{\Delta f}\langle \psi_{i,n}\psi^*_{i,n}\rangle, \quad P_{ij}(f) = \frac{1}{\Delta f}\langle \psi_{i,n}\psi^*_{j,n}\rangle, \quad R^2_{ij}(f) = \frac{|P_{ij}|^2}{P_{ii}P_{jj}}, \tag{3.2}$$

where "*" stands for complex conjugation. While the (real) P_{ii} quantifies the power per unit frequency in the fluctuations, the (complex) P_{ij} measures the amount of power per unit frequency that can be attributed to oscillations that have a nearly-constant phase difference between probes i and j, indicating the presence of a consistent wave structure in that direction. This is expressed by the normalized R^2_{ij}, which is close to 1 when there is a consistent phase difference among the probes, and close to 0 when no correlation exists. In fact, the significance coherence threshold for a 95% confidence level over N_w realizations is $1 - 0.05^{1/(N_w-1)}$ [164]; accordingly, any value of R^2_{ij} larger than this threshold (in our analysis, > 0.005 for $N_w = 600$) can be considered as an indication of a statistically significant behavior. On the other hand, as probes (1), (2) are aligned along $\hat{\boldsymbol{\theta}}$ direction and probes (1), (3) along $\hat{\boldsymbol{\zeta}}$ direction, we shall call $R^2_\theta = R^2_{12}$ and $R^2_\zeta = R^2_{13}$.

The phase difference $\theta_{ij,n}(f)$ for the pair of probes i, j and the time window n can be computed as

$$\theta_{ij,n}(f) = \arg(\psi_{i,n}\psi^*_{j,n}). \tag{3.3}$$

Note that, with the present definition, a positive $\theta_{ij,n}$ would indicate a wave that travels from probe i to probe j, namely its phase at probe i is ahead in time with respect to the phase at probe j. In the Two-Points Power Spectral Density (PSD2P) technique [78, 127, 128], the mean phase difference is approximated as $\langle\theta_{ij}\rangle = \arg(P_{ij})$. In a slight departure from this approach, we employ circular-normal statistics [165] to estimate the mean and standard deviation of the distribution as

$$\langle\theta_{ij}\rangle(f) = \arg\left(\langle\exp(\mathrm{i}\,\theta_{ij,n})\rangle\right), \tag{3.4}$$

$$\sigma_{ij}(f) = \frac{1}{N_w - 1}\sum_{n=1}^{N_w}(\pi - |\pi - |\theta_{ij,n} - \langle\theta_{ij}\rangle||). \tag{3.5}$$

The computation of the standard deviation, and not just the mean phase difference, together with the information provided by $R^2_{ij}(f)$, allows the assessment of the uncertainty and significance of our results. Indeed, these two quantities are related, as one expects $\sigma_{ij} \to 0$ when $R^2_{ij} \to 1$. Then, we compute the azimuthal wavenumber, the azimuthal mode number, and the parallel wavenumber as

$$\kappa_\theta(f) = \frac{\langle\theta_{12}\rangle}{d}, \qquad m_\theta(f) = r\,\kappa_\theta(f), \qquad \kappa_\zeta(f) = \frac{\langle\theta_{13}\rangle}{d}, \tag{3.6}$$

where $d = 10$ mm is the separation distance between probes and r is the radial distance from the MN symmetry axis. This setup enables resolving wavenumbers in the principal domain $[-314, 314]$ rad/m. The azimuthal mode number m_θ ought to be an integer in an axisymmetric MN, while κ_ζ may take real values. Note that, very close to the symmetry axis (for $r \lesssim 10$ mm), the effective radii of probes (1) and (2) can differ substantially, and therefore their usage to estimate $\kappa_\theta(f)$ becomes inadequate.

Finally, to identify any quadratic phase couplings in the data, the signature of nonlinear power transfer among modes in the spectrum (e.g., three-wave coupling), we define the (normalized) bi-coherence at probe i, $B^2_i(f_1, f_2)$, as [166]

$$B^2_i(f_1, f_2) = \frac{\left|\langle\psi_{i,n}(f_1)\psi_{i,n}(f_2)\psi^*_{i,n}(f_1 + f_2)\rangle\right|^2}{\left\langle\left|\psi_{i,n}(f_1)\psi_{i,n}(f_2)\right|^2\right\rangle\left\langle\left|\psi_{i,n}(f_1 + f_2)\right|^2\right\rangle}. \tag{3.7}$$

The bi-coherence describes nonlinear interactions between frequencies f_1, f_2, and $f_3 = f_1 + f_2$; a consistent phase-lock over realizations yields a bi-coherence value close to 1 (complete phase coupling), whereas a random phase relation or noise should average close to zero. Indeed, for a 95% confidence level, the significance threshold of the bi-coherence considering N_w realizations is approximately $3/N_w$ [167].

3.3 Results and discussion

Figure 3.3 displays the low-frequency power spectral density at the reference probe, P_{11}, and the value of the two coherences R^2_ζ and R^2_θ, in the range 0–1 MHz, at several measurement points in the MN for both analyzed operating conditions. For reference, the noise floor level for P_{11} in this range was estimated to be well below 10^{-13} V^2/Hz in the absence of plasma. Beyond 1 MHz, the only major features identifiable in the spectrum are the Helicon pump frequency 13.56 MHz (with peak power spectral density values of $P_{11} \simeq 10^{-6}$–10^{-7} V^2/Hz) and its harmonics.

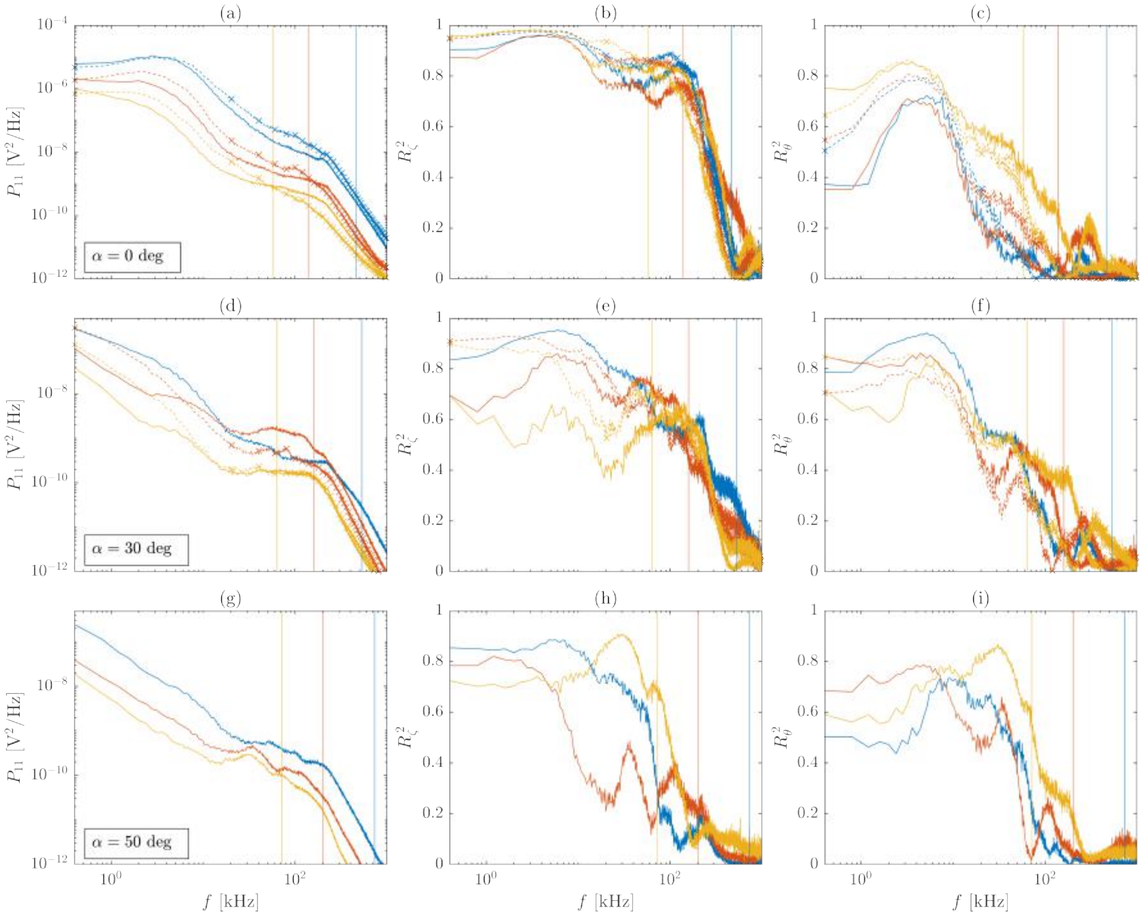

Figure 3.3: Power spectral density at the reference probe, P_{11} (first column), and two-probe coherence values, R^2_ζ (second column) and R^2_θ (third column), at some selected measurement points in the MN. Solid lines refer to the $\dot{m} = 5$ sccm case, whereas dashed lines (where existing) represent the $\dot{m} = 10$ sccm case. For all plots, the blue lines refer to $\zeta = 50$ mm, the red lines to $\zeta = 100$ mm, and the yellow lines to $\zeta = 150$ mm. Corresponding vertical lines indicate the lower-hybrid frequency f_{LH} for each axial position.

These results evidence two features of the low-frequency spectrum: (*i*) a very low-frequency ($\lesssim$ 4–5 kHz) coherent oscillation, with large values of P_{11} and R^2_ζ, R^2_θ roughly everywhere in the plume, and with a clear peak on the axis ($\alpha = 0$ deg) and nearer to the source ($\zeta = 50$ mm); (*ii*) a broadband fluctuation extending roughly until $f = 200$ kHz, followed by an exponential power decay. This frequency band is characterized by milder yet significant coherence values. Embedded in this broadband fluctuation, a mid-frequency ($\simeq$ 30–50 kHz) mode is evident at positions away from the axis, exhibiting a raise in coherence. A smaller, secondary bump is identifiable at the double frequency, $\simeq$ 100 kHz, at some locations. The lower-hybrid frequency, $f_{LH} = \sqrt{\omega_{ci}\,\omega_{ce}}/2\pi$ (with $\omega_{cj} = |q_j|B/m_j$, $j = i, e$), although falling roughly in the frequency range 60–500 kHz, does not seem to align with any major structure in the spectrum nor the coherences, but it agrees at least in order of magnitude with the end of the broadband fluctuation range.

The effect of increasing the operational mass flow rate from $\dot{m} = 5$ to 10 sccm is observed in the first two rows of plots in Figure 3.3. Overall, the spectrum and the coherences do not experience important changes, with the exception of a larger P_{11} on the axis. At $\alpha = 30$ deg, the power level is greater for $\dot{m} = 10$ sccm at very low frequencies, < 5 kHz; beyond, the power level is lower than in the $\dot{m} = 5$ sccm case at $\zeta = 100$ mm and no distinctions are found for $\zeta = 150$ mm.

We find that the coherence values of R^2_ζ and R^2_θ are overall comparable, although not necessarily equal, and in fact they differ substantially for some frequencies at some measurement points. In particular, we note that $R^2_\theta \ll R^2_\zeta$ on the axis (at $\alpha = 0$ deg). This could be justified by the fact that, around this region, probes (1) and (2) sample at quite different radii from the axis, and would suggest that fluctuations do not exhibit a coherent behavior over the radial direction. The similarity between the values of R^2_ζ and R^2_θ is larger away from the axis and especially downstream, where the displacement between probes (1) and (2) better represents the azimuthal direction. This indicates that, at least there, any modes that are coherent are so along both $\hat{\boldsymbol{\zeta}}$ and $\hat{\boldsymbol{\theta}}$ directions. With these provisions in mind, in the remainder of this section we shall conservatively use $R^2_{min} = \min(R^2_\zeta, R^2_\theta)$, unless otherwise noted, instead of either of the two quantities.

With the goal of reasoning about the possible waves that could explain the observed fluctuations in the data, Figure 3.4 displays the two-dimensional maps of the time-averaged plasma density n and plasma potential ϕ_p, obtained from the analysis of the I–V characteristics of the reference probe. Since the probe is not compensated in the radiofrequency, the measured electron temperature T_e is considered less trustworthy and is not shown. Nevertheless, the measurements suggest a nearly-uniform T_e with mean value equal to 12.5 eV for the $\dot{m} = 5$ sccm case and 7 eV for the $\dot{m} = 10$ sccm case in the explored domain, with a standard error of ±2 eV, consistent with previous investigations on this prototype [168].

In the following, each of the identified features of the low-frequency spectrum is separately analyzed. Figure 3.5 presents the values of P_{11}, R^2_{min}, κ_ζ, and m_θ for the $\simeq 4$ kHz mode in the sampled region of the MN, illustrating that this oscillation is strongest near the axis and closer to the plasma source, is highly coherent everywhere (the lower values seen near the axis are due to the low R^2_θ, as explained above), and has $m_\theta = 0$ at all points, with an exception perhaps at mid-angles downstream, where $m_\theta = 1$ is more likely. The parallel wavenumber κ_ζ is small (around 0–10 rad/m) in the core of the plasma jet; slightly higher values seem to exist in the peripheral region (10–30 rad/m). This mode seems rather stable, or even to gain importance, upon doubling the mass flow rate from $\dot{m} = 5$ to 10 sccm. The peak frequency remains essentially unaffected.

Plausibly, this very low-frequency, global oscillation is the consequence of an ionization instability in the plasma source. Oscillations attributed to ionization dynamics are also reported in other MN thrusters [80–82]. Moreover, they are well known in Hall effect thrusters, where they are termed *breathing oscillations* [66, 67]. In addition, this kind of oscillations has also been observed in plasma sources [169] and in

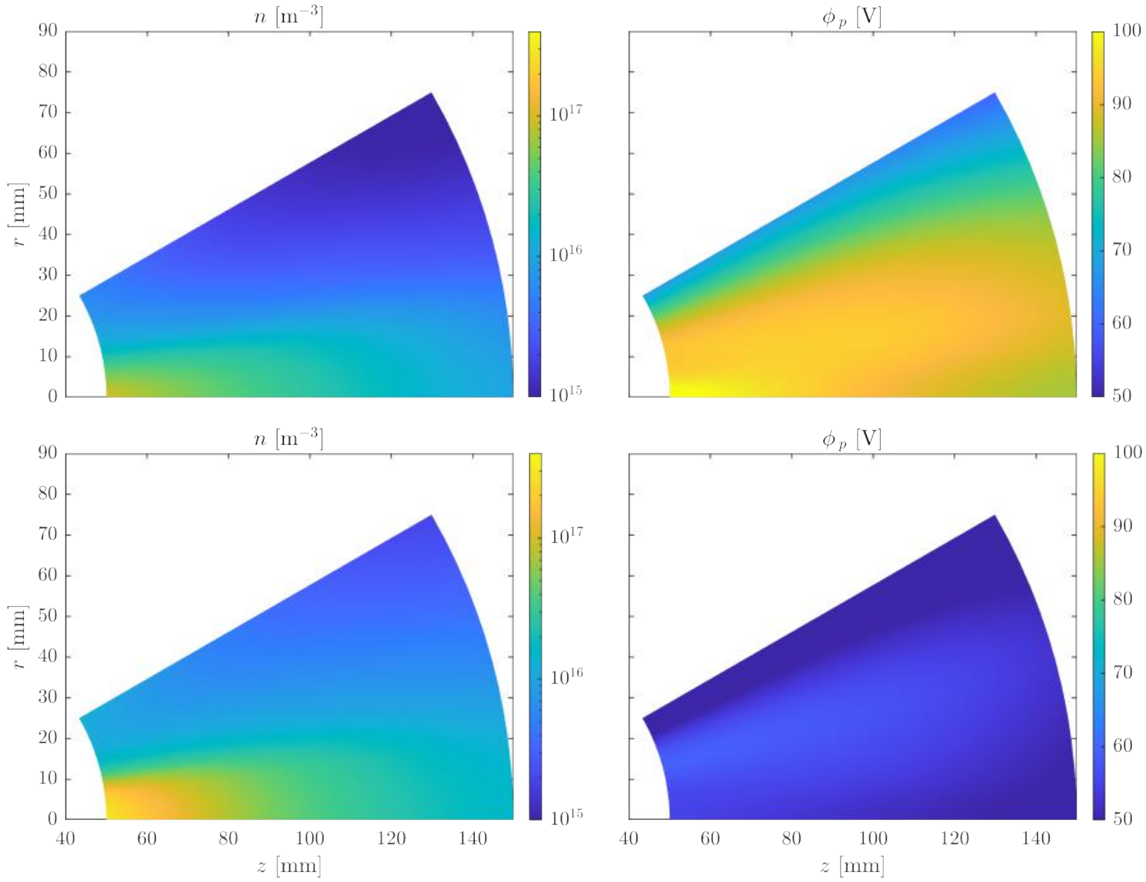

Figure 3.4: Two-dimensional maps of the time-averaged plasma density n and plasma potential ϕ_p with respect to ground for both the $\dot{m} = 5$ sccm case (top row) and the $\dot{m} = 10$ sccm case (bottom row).

hollow cathodes [170, 171]. They exhibit a global behavior, with little to no propagation in space [65, 172], and their characteristic frequencies are roughly < 40 kHz [64, 173]. Simple ionization instability models, like the predator-prey one [65], predict oscillations at frequencies comparable to the hybrid residence time of ions and neutrals within the chamber, defined as

$$f = \frac{\sqrt{v_i v_n}}{2\pi L}, \tag{3.8}$$

where v_i and v_n are the ion and neutral characteristic velocities in the ionization region, respectively. Characteristic velocities of xenon neutrals and ions can be estimated from their respective sound velocities: $v_n \approx 160$ m/s (assuming a temperature of 400 K for xenon neutrals), and $v_i \approx 3$ km/s for the $\dot{m} = 5$ sccm case and 2.3 km/s for the $\dot{m} = 10$ sccm case. For a chamber length of $L = 120$ mm, the expected frequency is around 5.8 kHz and 5 kHz for each case, respectively, which is within the same order of magnitude as the frequencies of the on-axis peaks found in our data.

Regarding the mid-frequency mode at $\simeq 50$ kHz, Figure 3.6 allows us to conclude that the oscillation power is spread out to larger angles from the axis, albeit featuring an overall smaller P_{11} than the $\simeq 4$ kHz oscillation. The minimal coherence, although greater than the significance threshold 0.005 everywhere, is larger around 30–35 deg. At these mid

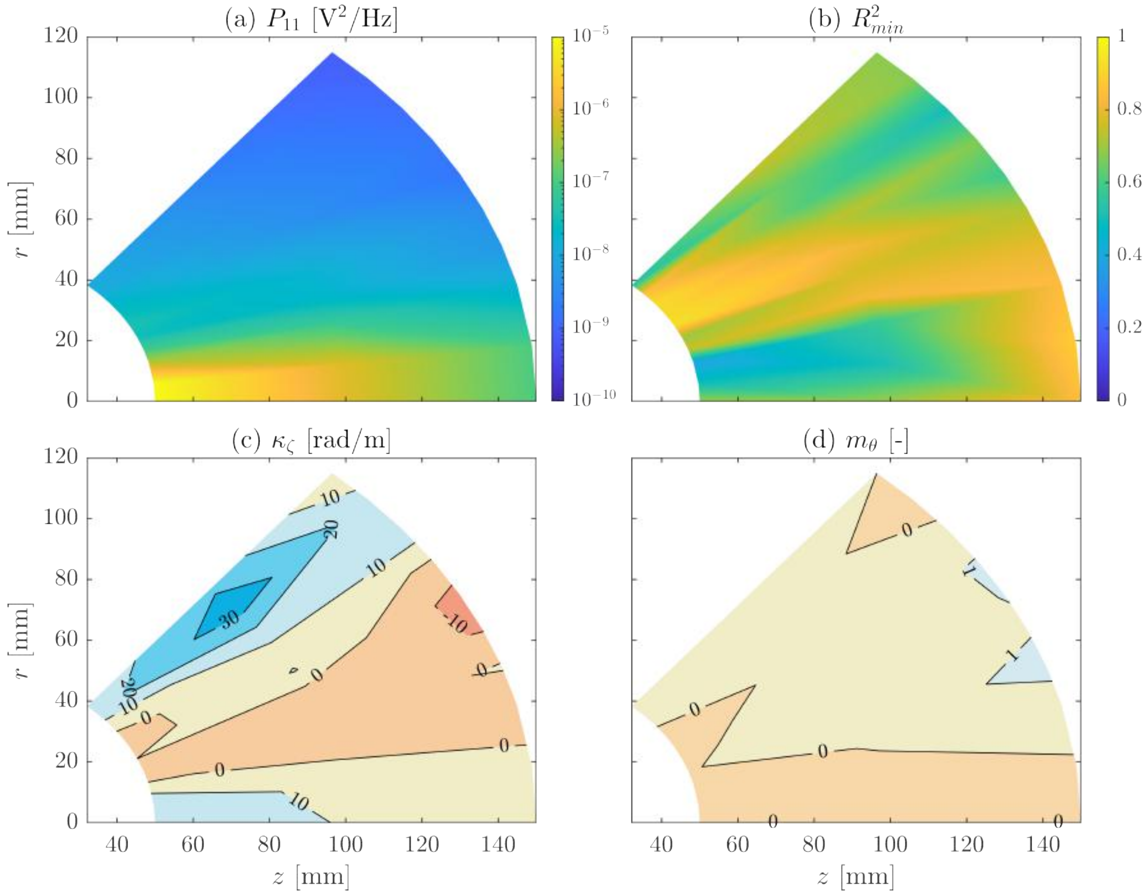

Figure 3.5: Two-dimensional maps of (a) the power spectral density at the reference probe, P_{11}, (b) the minimal coherence, R^2_{min}, (c) the parallel wavenumber, κ_ζ, and (d) the azimuthal mode number, m_θ, around 4 kHz for the $\dot{m} = 5$ sccm case. The average of these quantities in the range 4 ± 1 kHz is shown.

angles, the oscillation is best described by low negative values of m_θ, from around -3 to 0, and near-zero κ_ζ values. Interestingly, there is also a distinct behavior in the peripheral region of the MN for this mode, although the coherence is lower there compared to the core region. Indeed, larger negative values of m_θ (down to -8) are found at large angles, as well as higher κ_ζ values up to 120 rad/m.

Now, in order to analyze the full < 200 kHz broadband region, including the 50 kHz oscillation, and to further discuss the wave structures in our setup, Figure 3.7 reconstructs the dispersion diagrams (m_θ, f) and (κ_ζ, f) at selected points. The coherences R^2_θ and R^2_ζ, respectively, are used to color the datapoints, while the standard deviations σ_{ij} in $\hat{\boldsymbol{\theta}}$ and $\hat{\boldsymbol{\zeta}}$ directions (as given in Equation 3.5) are used to quantify the uncertainty at each frequency. The first row of plots in Figure 3.7 presents the experimental dispersion relation at $\zeta = 100$ mm, $\alpha = 30$ deg for the $\dot{m} = 5$ sccm case. This result is representative of nearly all mid-angle positions for the $\dot{m} = 5$ sccm case and for most of the $\dot{m} = 10$ sccm dataset. Keeping in mind the admonitions of Section 3.3.1, where we discuss the limitations of the analysis technique and the implications in the case of more than one coexisting wave, the diagrams suggest a linear trend in m_θ toward negative values, while no clear trend emerges in κ_ζ for

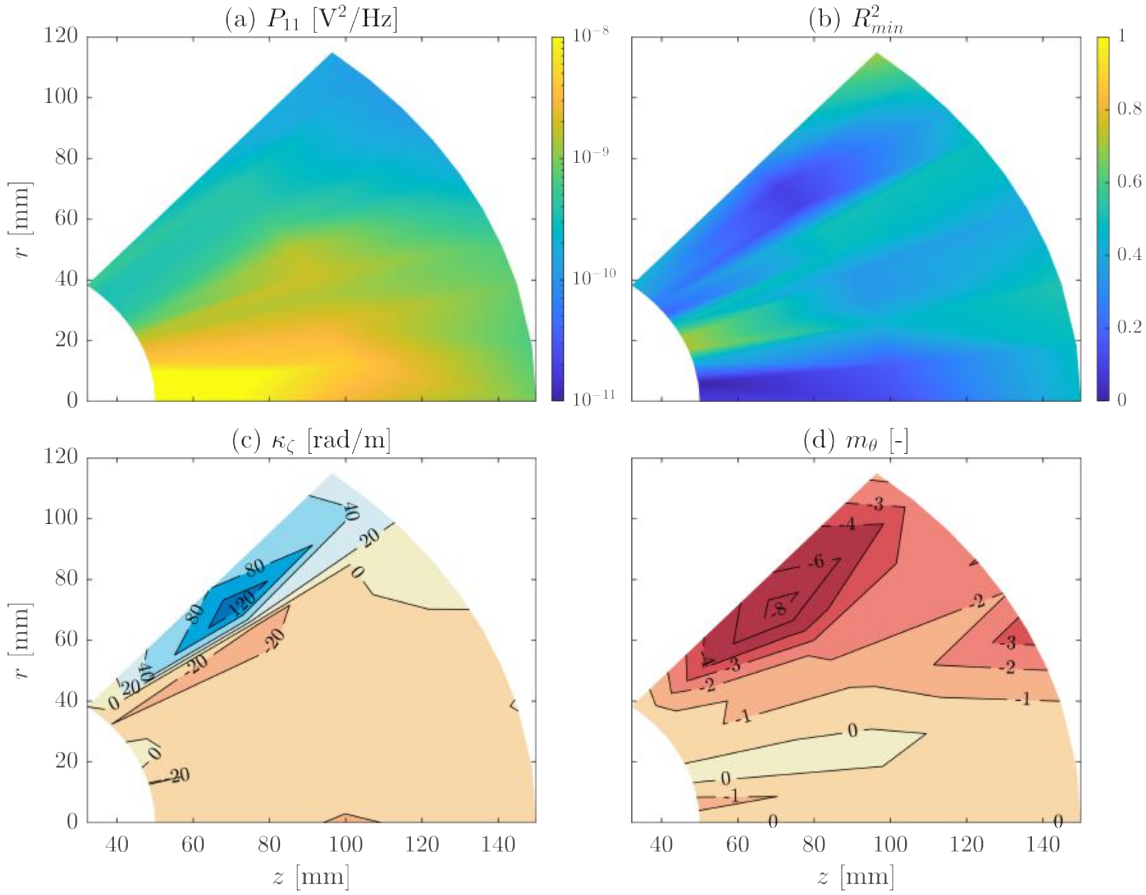

Figure 3.6: Two-dimensional maps of (a) the power spectral density at the reference probe, P_{11}, (b) the minimal coherence, R^2_{min}, (c) the parallel wavenumber, κ_ζ, and (d) the azimuthal mode number, m_θ, around 50 kHz for the $\dot{m} = 5$ sccm case. Note that the color scale for P_{11} differs from that in Figure 3.5. The average of these quantities in the range 50 ± 5 kHz is shown.

the explored frequency range. The corresponding azimuthal phase velocities are typically between 10^3–10^4 m/s; computed min/max values are reported in Table 3.1. The 50 kHz (and weaker 100 kHz) coherent mode falls within the negative m_θ linear trend, suggesting that it is part of the same wave as the broadband spectrum. The 4 kHz mode, however, does not align well with it, and indeed shows a 0–1 positive value of m_θ as discussed above, which further suggests that this feature is separate from the rest. The uncertainty (characterized by the standard deviation in each plot) is generally lower around the 4, 50 kHz modes than it is at other frequencies. Beyond 200 kHz, the coherence is low and the standard deviation is large.

The second row of plots in Figure 3.7 corresponds with the high-m_θ peripheral region of the 50 kHz mode shown in Figure 3.6. In this region, the same trend as above is found at low frequencies. However, beyond 60 kHz, the m_θ dispersion relation appears to abruptly return to near-zero m_θ values and has low coherence, wide standard deviation. A positive slope in the κ_ζ diagram is also apparent, yet this trend also stops around the same frequency range. This behavior is only found in this peripheral region of the MN.

Finally, the last row of plots in Figure 3.7 shows the change in the dispersion diagrams of the first row when doubling the mass flow rate to $\dot{m} = 10$ sccm. In this case, the dispersion trend in the azimuthal direction is essentially a vertical line at $m_\theta = 0$ up to 50 kHz, followed by a negative trend until 130 kHz, frequency at which the m_θ solution undergoes a discrete jump, from $\simeq -9$ to $\simeq -23$. Meanwhile, the κ_ζ diagram exhibits no such features, showing low values of κ_ζ throughout the analyzed band. We consider this behavior exceptional, as it is found only at some locations in the $\dot{m} = 10$ sccm case for $\alpha \geq 30$ deg.

While we do not have a definite explanation for the last two illustrated findings, it is possible that two (or more) waves coexist at each frequency, confounding the two-probe analysis technique as explained in Section 3.3.1. In fact, if two counter-propagating waves of similar characteristics exist at the measurement point (giving rise to an essentially standing-wave structure), it is expected that the analysis technique would yield $\langle\theta_{ij}\rangle \simeq 0$ (if the plasma at the two probes i, j is in phase) or $\langle\theta_{ij}\rangle \simeq 180$ deg (out of phase plasma at the probes i, j). Overall, the presence of a second wave would affect the dispersion diagram by pushing the values of $\langle\theta_{ij}\rangle$ toward either of these two values. This, of course, assumes repeatability of the spatial structure with respect to the probes from realization to realization: in our experiments, all samples were taken contiguously in time, so arguably this could be the case. What we observe beyond $f = 60$ kHz for $\dot{m} = 5$ sccm, $\alpha = 50$ deg, and below $f = 50$ kHz for $\dot{m} = 10$ sccm, $\alpha = 30$ deg, could be explained as the coexistence of two counter-rotating yet otherwise identical waves, with a varying ratio of amplitudes. The discrete jump in m_θ in the latter case at $f = 130$ kHz corresponds to $\Delta\langle\theta_{ij}\rangle \simeq 160$ deg, which (although not exactly 180 deg) would suggest that the near-standing-wave structure generated by the two counter-rotating waves has a node between the two probes from that frequency onward.

We now return to the more canonical case shown in the first row of plots in Figure 3.7, representative of a large portion of the MN. Given that some integer-multiple structures are present in the analyzed frequency range, namely the 50 kHz mode and a secondary bump at 100 kHz at some measurement points, it is natural to inquire if there is some non-linear coupling among modes, i.e., whether these two modes are phase-locked harmonics, which would suggest that harmonic excitation is taking place. However, close examination of the bi-coherence at the reference probe $B_1^2(f_1, f_2)$ disproves this hypothesis, as only very low values of this quantity are found for $f_1, f_2 < 1$ MHz ($B_1^2 < 0.017$, comparable to the significance threshold value 0.005). This strongly differs from the bi-coherence found among the Helicon pump frequency and itself ($f_1 = f_2 = 13.56$ MHz, yielding $B_1^2 \simeq 0.99$) or with its first harmonic ($f_1 = 13.56$ MHz and $f_2 = 27.12$ MHz, yielding $B_1^2 \simeq 0.98$), where it is natural to assume that the pump wave is exciting its harmonics non-linearly.

A radically different story is told by the bi-coherence among the pump frequency 13.56 MHz and the < 1 MHz range, as explained next. The first plot in Figure 3.8 displays P_{11} for the case of $\dot{m} = 5$ sccm at $\zeta = 100$ mm, $\alpha = 30$ deg in the neighborhood of the pump frequency, which exhibits noticeable shoulders around the main peak, with

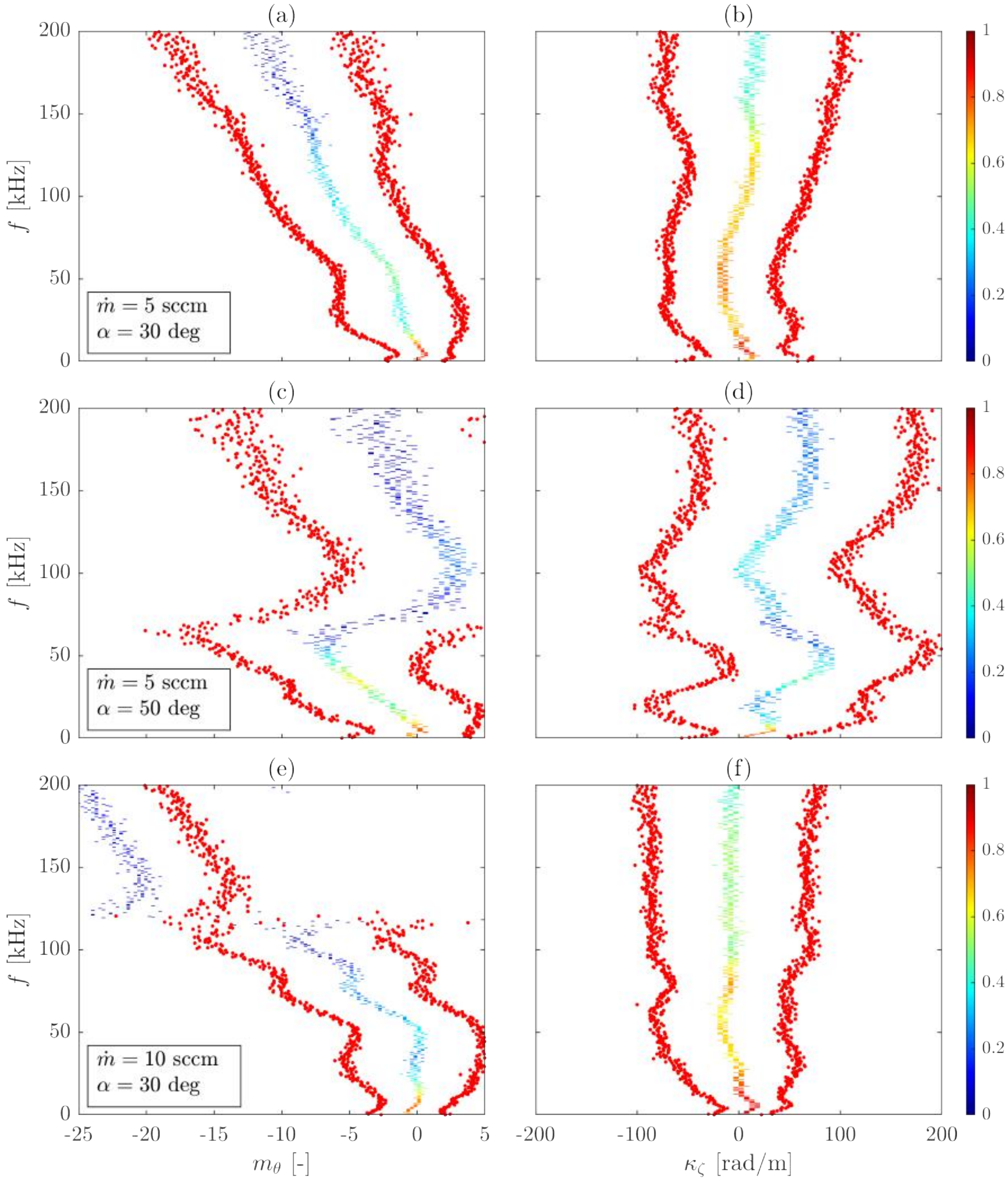

Figure 3.7: Reconstructed dispersion diagrams (m_θ, f) and (κ_ζ, f) at $\zeta = 100$ mm for two values of α and the two mass flow rates. The coherence R^2_θ is used to color the datapoints in (a), (c), and (e), whereas R^2_ζ is used for (b), (d), and (f). The ± 1-σ intervals (according to the definition in eq. (3.5)) are shown using red dots. In terms of the azimuthal wavenumber, $m_\theta = 10$ corresponds to $\kappa_\theta \simeq 200$ rad/m for $\alpha = 30$ deg and to $\kappa_\theta \simeq 130$ rad/m for $\alpha = 50$ deg.

a bandwidth of roughly 150–200 kHz each (approximately the same bandwidth as our low-frequency broadband fluctuation). The remaining two plots in Figure 3.8 display the bi-coherence B^2_1 in this range, showing that significant values of B^2_1 exist for $f_1 = 13.56$ MHz and for $f_3 = f_1 + f_2 = 13.56$ MHz. This suggests that there is a nonlinear power coupling between the pump wave and the low-frequency spectrum. (we note that the bi-coherence map has multiple symmetries, owing to the definition of B_i^2 in Equation 3.7). This suggests a nonlinear power coupling between the pump wave and the low-frequency spectrum. Specifically, this would signify the decay of the Helicon pump wave into side-bands below the pump frequency and the low-frequency fluctuations. Indeed, our results show qualitative agreement with those of Lorenz *et al.* [56] (see, e.g., Figures 3, 8, and 10 therein), who argue that the 13.56 MHz excitation frequency in their experiment couples with low-frequency ion acoustic waves and high-frequency Trivelpiece-Gould waves, satisfying the resonance conditions $|f_1| + |f_2| + |f_3| = 0$, $\boldsymbol{k}_1 + \boldsymbol{k}_2 + \boldsymbol{k}_3 = 0$. Consequently, data suggests that the observed spectrum in our case is consistent with a parametric decay instability.

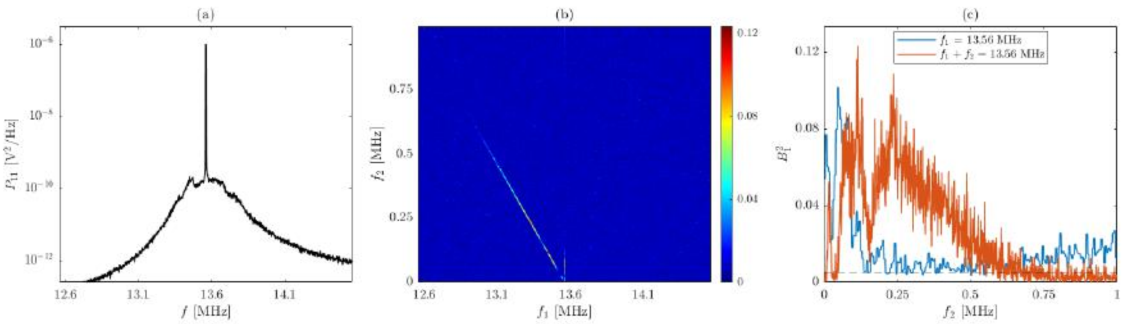

Figure 3.8: (a) Power spectral density at the reference probe, P_{11} in the interval $f = 13.56 \pm 1$ MHz; (b) squared bi-coherence in the neighborhood of $f_1 = 13.56 \pm 1$ MHz and $f_2 < 1$ MHz; and (c) bi-coherence along the vertical and diagonal features corresponding to $f_1 = 13.56$ MHz and $f_3 = f_1 + f_2 = 13.56$ MHz, respectively. Plot (c) showcases the significance level of the bi-coherence (0.005) as a dashed horizontal line. All the plots (a), (b) and (c) refer to the $\dot{m} = 5$ sccm case, at $\zeta = 100$ mm, $\alpha = 30$ deg.

In the interest of identifying the nature of the low-frequency waves in our experiment, various relevant velocities are reported in Table 3.1 for two positions of interest within the plume and the two tested mass flow rates. To estimate the $\boldsymbol{E} \times \boldsymbol{B}$ and diamagnetic drift velocities, the spatial gradients of the maps shown in Figure 3.4 were computed. The $\boldsymbol{E} \times \boldsymbol{B}$ drift direction is along $+\hat{\boldsymbol{\theta}}$ (with the only exception being near the axis downstream, where a shallow minimum of ϕ_p seems to develop, especially in the $\dot{m} = 10$ sccm case). The diamagnetic electron drift corresponds everywhere to the $-\hat{\boldsymbol{\theta}}$ direction.

It is clear that the observed phase velocities fall in the same order of magnitude as the ion sound velocity, although a near-exact match (as in [53]) is unlikely. Nevertheless, the analysis rules out any major role of the $\boldsymbol{E} \times \boldsymbol{B}$ and diamagnetic drift velocities, or the Alfvén velocity, in the wave dispersion relations. Incidentally, we note that the possible coexistence of counter-rotating waves (as discussed above and in Section 3.3.1) can have the net effect of reducing the experimentally-found values of m_θ for each frequency, resulting in an artificially higher estimated phase velocity. While $\boldsymbol{k}$-conservation in the parametric decay instability is expected to yield low-frequency waves traveling in the same direction [56], wave scattering against electrons and ions could eventually give rise to a richer, turbulent spectrum, comprising acoustic waves traveling in all directions. If multiple waves were present at each frequency in our data (and we currently lack the means to ascertain it), this could partially explain the difference between the ion sound velocity and the phase velocity.

	$\zeta = 100$ mm, $\alpha = 30$ deg		$\zeta = 150$ mm, $\alpha = 30$ deg	
	5 sccm	10 sccm	5 sccm	10 sccm
Phase velocity, v_{ph}	$-[4.64, 11.4]$	$-[2.03, 17.7]$	$-[7.07, 13.0]$	$-[5.23, 19.5]$
Ion sound velocity, c_s	± 3.03	± 2.27	± 3.03	± 2.27
$\boldsymbol{E} \times \boldsymbol{B}$ drift, v_E	423	261	766	315
Diamagnetic drift, v_D	-70	-39	-156	-145
Alfvén velocity, v_A	144	87	76	49

Table 3.1: Characteristic velocities at selected measurement points, for both operating conditions. All velocities are in km/s.

In order to close this discussion, it is worth mentioning that some similarities and differences exist with the oscillation spectra found in the MNs of other devices. Hepner *et al.* [78], in the MN of an electron-cyclotron resonance thruster, identify a broadband fluctuation in their ion saturation measurements, which extends to higher frequencies than ours; immersed in it, low-frequency modes at 13 kHz and 26 kHz (ascribed to an ionization instability) are found only downstream (and not everywhere in the plume as would be our case). Their broadband dispersion relation features, however, are characterized by a strong propagation in the axial direction, which our data does not have. The oscillations detected within the work of Takahashi *et al.* [79] on a Helicon-type, 13.56 MHz thruster, also share partial similarities with the ones observed in this study. They find plasma density and potential oscillations with a clear coherent peak at 40 kHz (and a subsidiary peak at 80 kHz) and azimuthal structure, concentrated mainly around the high-density conic structures that exist in their plasma plume. While it is unclear whether their data also has a broadband fluctuation, that peak is at least two orders of magnitude greater than the rest of the shown spectrum.

Hepner *et al.* [78] attribute their broadband observations to a LHD instability. Their dispersion relation uses a fluid treatment for ions with $T_i = 0$, while electrons are described with a kinetic approach. These waves typically have a phase velocity that falls in the same range as the ion sound velocity. It can be shown that such dispersion relation reduces to the Modified Simon-Hoh (MSH) instability [174, 175] for $\kappa_{\|} = 0$ and in the quasineutral fluid limit. The condition $\kappa_{\|} \simeq 0$ approaches the findings in our study and, incidentally, it is one for which the LHD instability is found by Carter *et al.* [176] to have maximum growth rate. However, neither the MSH nor LHD disperinstabilitiesion relations produce any complex (i.e. unstable) solution for the values and signs of the plasma property gradients in our MN. Moreover, it was seen in figure 3.3 that the lower-hybrid frequency does not align with any specific feature in the spectrum.

Takahashi *et al.* [79] describe their coherent mode as a magnetosonic wave, which corresponds to a compressional Alfvén wave. For low wavenumbers κ_θ, the dispersion relation of the magnetosonic wave scales according to the Alfvén velocity v_A, to then asymptotically approach the lower-hybrid frequency at high wavenumbers [177, 178]. Whilst theiry have Alfvén velocities are around 10^3 m/s, which show good agreement with their data, Alfvén velocities in our study are in the range of 10^5 m/s (owing to the lower plasma density and higher magnetic field strength) and differ significantly in magnitude from the phase velocities, as reported in Table 3.1.

Finally, as indicated in the introduction, and although there are substantial differences among the two devices and their plasma plumes (e.g., the second of them features unique 'high-density conics'), these two works disagree on the reported direction of the quasilinear electron transport induced by the oscillations, with Hepner *et al.* indicating a radially-outward transport and Takahashi *et al.* an inward transport focusing toward the axis of the MN. In our case, if we identify our broadband oscillation as being, most likely, the excitation of the ion acoustic branch resulting from a parametric decay instability of the pump wave, it should give rise to the anomalous heating of ions and electrons, as well as an increased effective collision frequency [52]. It is then expected that this enhanced collisionality would act as to relax the gradients in the plasma properties and, hence, to displace the plasma outward in our single-peaked plume, and therefore, increasing its divergence angle. Nevertheless, ascertaining this would require a far more complex setups, capable of sampling (synchronously) the oscillations in potential *and* plasma density, similar to the technique of Takahashi *et al.* [79], and likely featuring more than two probes in each direction to discriminate among multiple waves.

3.3.1 Limitations of the selected approach

The proposed experimental setup and analysis technique have enabled us to observe low-frequency oscillations, and assert the presence of a coherent wave mode and a broadband, more turbulent, fluctuation (with 1 or 2 larger-power modes within), as well as the possibility of nonlinear power coupling between the pump wave at 13.56 MHz and the low-frequency range. Notwithstanding this, it is pertinent to assess the limitations of this approach.

As advanced above, a main limitation of the two-probe coherence technique stems from the inability to tell apart multiple waves that may coexist at a given frequency. If there are two or more waves of comparable amplitude at a given frequency, the phase difference measured between the two probes will be some form of average of each of them. In particular, two identical, counter-traveling waves setting up a standing-wave structure would resolve as either $\langle\theta_{ij}\rangle = 0$ or 180 deg, depending if there are standing-wave nodes between the probes. Moreover, if the waves do not have a fixed phase relation between them among experimental realizationspetitions, the resulting coherence will be low and the standard deviation will be large, irrespective of how coherent is each of the participating modes is individually. A total of N probes lined in the same direction at non-commensurable distances would be needed to disambiguate among $N-1$ coexisting waves.

While we cannot preclude the possibility of multiple branches of the plasma dispersion relation being simultaneously excited in our experiments, the fact that the dispersion diagrams show rather clean trend lines suggests that, if present, this effect is minor and frequency-bounded, at least at the locations in the MN represented by the dominant behavior shown in the first row of plots in Figure 3.7. Indeed, the different azimuthal direction of the 4 kHz mode with respect to the rest of the analysed range makes us believe that this is a distinct oscillation mode altogether, likely induced by an ionization instability in the source as explained above.

Albeit the bi-coherence is only slightly affected by this phenomenon (at least as long as there is repeatability of all the involved waves and their relative phases among realizations), an inherent limitation of this metric stems from the inability to ascertain the direction of power transfer, if any, among quadratically phase-locked modes. Nevertheless, in the present study, as the coupling of the low-frequency spectrum occurs with the pump wave, it is natural to assume that power flows from the latter to the former, following a parametric decay instability.

Lastly, intrusive probes cause a perturbation of the plasma expansion in the MN, which in the past has been deemed to have a negligible effect on DC properties. However, the impact of these current-collecting obstacles on the oscillations remains to be unassessed. There is no reason to believe that probes cannot quench or alternatively promote fluctuations, or anchor the nodes of stationary. wave structures. Moreover, spurious correlations among probe signals could be caused by each probe on the others, especially if probes are too close to each other for their sheaths to interact. Here, we have used floating probe conditions and a 10 mm separation among probes, which is much greater than the largest Debye length in the explored domain ($\lambda_D < 0.93$ mm), in an attempt to reduce these undesired effects. Likewise, MN oscillations in a laboratory facility (where the plasma is subject to background pressure and interacts with conducting metallic walls) could differ from oscillations in free-space conditions and expansions to infinity.

3.4 Conclusions

In this paper, multi-probe data of the MN plume of a HPT prototype has been analyzed to characterize the low-frequency oscillation spectrum.

A very low-frequency oscillation, around 4 kHz, stronger on the axis and in proximity of the thruster, is likely the result of a breathing/ionization instability at the source.

A broadband fluctuation extending to roughly 200 kHz and featuring an essentially azimuthal structure, with phase velocity in the range 10^3–10^4 m/s compatible with the ion sound velocity, is found. Within this band, a high-coherence power peak is found at $\simeq$ 50 kHz and, at some locations, a weaker peak is detected at $\simeq$ 100 kHz. The parallel wavenumber is small, below $\pm$20 rad/m in the majority of the plume. The possible coexistence of multiple waves at each frequency was discussed as a possible mechanism biasing and distorting the dispersion diagrams found with the two-probe technique. A bi-coherence analysis suggests that there is no phase coupling among frequencies in the $\leq$ 1 MHz range, but points at a parametric decay instability of the pump Helicon wave as a plausible explanation for the broadband, ion-acoustic-like spectrum.

We have compared our findings with other results in the literature. While some similarities exist, available data is insufficient to infer universal aspects of plasma oscillations in MNs. Indeed, the specificities of each prototype source and plasma profile in the plume may render the effort of identifying trends a moot point. Regarding the crucial question of whether wave-induced transport is directed radially inward or outward in the MN, enabling electron detachment or increasing plume divergence, our findings and our tentative classification of the broadband oscillation as the result of a parametric decay instability would suggest the heating of ions and electrons, hence a gradient-relaxing (i.e., generally outward) transport of plasma particles. Further research is necessary to ascertain this classification and this potential conclusion.

4. EXPERIMENTAL CHARACTERIZATION OF OSCILLATIONS IN THE MAGNETIC NOZZLE OF AN ELECTRON CYCLOTRON RESONANCE THRUSTER

This chapter focuses on the experimental characterization of oscillatory phenomena between 5 and 100 kHz in the plasma of an Electron Cyclotron Resonance Thruster (ECRT) device. The presented work proposes measurements acquired simultaneously with three plasma diagnostics: an array of four floating Langmuir probes (LPs), a curling probe (CP), and high-speed camera imaging to try to characterize the plasma fluctuations. Data at different operating points are analyzed, leading to the identification of two different oscillation modes: one at low frequency ($\simeq$ 9 kHz), and another at higher frequency ($\simeq$ 60 kHz). Dispersion diagrams are reconstructed from the LP data by means of a combination of Two-Points Power Spectral Density (PSD2P) technique and coherence analysis, while non-linear power coupling is explored by means of a bi-coherence estimate. The oscillations are captured with very good agreement by all employed diagnostics. In addition, the data from the CP allows to carefully follow the impact of the oscillations upon the plasma density, whereas the data from the camera is analyzed by means of Proper Orthogonal Decomposition (POD) to characterize the behavior of the light emitted by the plasma within the source. Potential explanations for the observed behaviors are explored, addressing the possibility of the low-frequency oscillation being induced by an ionization-related mode, whereas the higher-frequency oscillation is compared against recent literature displaying oscillations with similar features developing in devices employing Magnetic Nozzles (MNs).

This chapter represents a transcription of the following conference paper (without the introduction section):

- **Maddaloni D.**, Boni F., Désangles V., Bayón-Buján B., Merino M., Terragni F., "Experimental characterization of oscillations in the Magnetic Nozzle of an Electron Cyclotron Resonance Thruster". In 38th International Electric Propulsion Conference (IEPC-2024). June 23-28, 2024, Toulouse, France.

The Ph.D candidate carried out the development of the LPs, the collection and post-processing of the experimental LP data, while also fundamentally contributing to the data interpretation and analysis. Additionally, the candidate implemented and adapted the PSD2P algorithm and the coherence estimate. They also undertook the initial drafting of the manuscript, the contents of which were presented at the IEPC 2024 by the candidate.

4.1 ECR thruster and vacuum facility

Data has been collected in the expanding plasma inside the magnetic nozzle of the 30 W ECR coaxial model developed at ONERA [8–11]. This prototype employs a permanent magnet generating a strictly diverging magnetic field. Microwaves are injected at a frequency of 2.45 GHz at the rear of the thruster. The ECR condition is met a few millimeters downstream from the backplate in the thruster discharge chamber, where the magnetic field reaches 875 G. The device is typically fed with xenon at mass flow rates around 1 sccm (1 sccm $\simeq$ 0.1 mg/s for xenon), and microwave power at 2.45 GHz around 30 W. In the context of this study, the mass flow rate, the power deposited in the plasma, and the driving microwave frequency are varied from their typical values: between 1 and 2.2 sccm for the flow rate, between 13 and 33 W for the power deposited at the backplate, and between 2.00 and 2.60 GHz for the driving frequencies. The whole thruster is electrically floating and its potential naturally rises from a few tens to a few hundreds of volts with respect to the vacuum tank reference ground.

Measurements have been performed inside the B09 vacuum chamber, a cylindrical vessel of 0.8 m in diameter and 2 m long, at the ONERA premises in Palaiseau. The high vacuum pumping system consists of three turbomolecular pumps and one cryogenic pump, yielding a total pumping speed of 13 000 l/s for xenon, with a base pressure of about 3×10^{-7} mbar. In this work, the background pressure with the thruster firing is in the range of $0.6 - 1.2 \times 10^{-5}$ mbar.

4.2 Plasma diagnostics

A set of three diagnostics has been used to characterize the plasma oscillations: an array of four Langmuir probes – developed at UC3M –, a microwave resonant curling probe – developed at ONERA –, and a high-speed camera – provided by ONERA. A single trigger signal enables to collect acquisitions synchronously. Additionally, the forward and reflected microwave power, alongside the thruster floating potential, are separately monitored. On the left of Figure 4.1, a sketch of the ECRT source and the magnetic nozzle is illustrated, alongside a visual representation of the whole experimental setup with the three diagnostics. The reference frame associated with the plasma source is the cylindrical coordinate system $(\hat{\boldsymbol{r}}, \hat{\boldsymbol{\theta}}, \hat{\boldsymbol{z}})$, whereas the probe system refers to a different, local frame $(\hat{\boldsymbol{\zeta}}, \hat{\boldsymbol{\alpha}}, \hat{\boldsymbol{\theta}})$. On the right of Figure 4.1, a photograph of the ECRT source and the probes is shown. The probe system, consisting of the LPs and the CP, can be moved within the 2D polar coordinate system $(\hat{\boldsymbol{\zeta}}, \hat{\boldsymbol{\alpha}})$ in the plasma plume using a motorized stage. **Probes are mounted in a way to minimize possible perturbation of the setup on the plasma plume, and extensive testing is performed to ensure that the tips of the LPs, positioned ahead of the CP, do not interfere with the CP measurements. Ultimately, it is found that this perturbation is negligible, which can be explained by the limited thickness of the LP tips.**

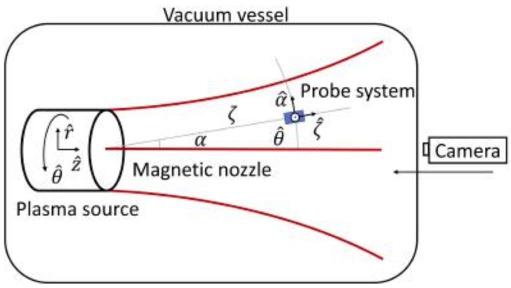

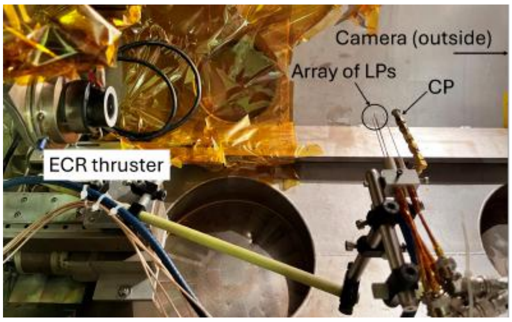

Figure 4.1: Left: Sketch of the ECRT source and its MN, alongside a visual representation of the whole experimental setup with the three diagnostics. The probe system, comprising the LP array and the CP, is immersed into the plasma and is represented with a blue rectangle, whereas the camera, placed outside of the vacuum vessel, to the right, faces the thruster exhaust and is focused on the thruster source. The cylindrical frame that refers to the plasma source is labeled $(\hat{\boldsymbol{r}}, \hat{\boldsymbol{\theta}}, \hat{z})$. The spatial coordinates of the probe system in the 2D plane, instead, are based on a polar frame $(\hat{\boldsymbol{\zeta}}, \hat{\boldsymbol{\alpha}})$, with the origin fixed at the thruster exit plane. Right: photograph of the experimental setup, showing the array of LPs and the CP.

4.2.1 Langmuir probes

The array of LPs comprises four (identical) uncompensated Langmuir probes. The reference probe is placed in a central position, whereas the other three probes are fixed 10 mm apart from the reference one, each aligned along a different direction of $(\hat{\boldsymbol{\zeta}}, \hat{\boldsymbol{\alpha}}, \hat{\boldsymbol{\theta}})$. The LPs consist of an alumina body with a cylindrical tungsten tip measuring 0.25 mm in diameter and 4 mm in length. Probes are left electrically floating and are connected to the recording instrument through coaxial cables to minimize signal noise. The time variation of the floating potential is recorded with a Keysight Infiniium Mixed Signal Oscilloscope with 4 active channels, 4 GHz of bandwidth, 10 GSa/s of sampling rate, and 8 bits of vertical resolution. For each measurement point, 5 subsequent scans of 0.1 s of duration are collected. Each scan is then divided in 20 non-overlapping segments, yielding a total of 100 snapshots. This allows for increased statistical significance for averaging purposes.

In this work, the measurement of the floating potential of the LPs is used since (i) no power supply is required, (ii) problems related to low-pass filtering introduced by the presence of shunt resistors are minimized, and (iii) it introduces lower disturbances in the plasma as probes are not biased. Floating potential measurements have already been used as a proxy for plasma potential fluctuations under the assumption of constant electron temperature over the (expected) fluctuation time and space scales [47, 49, 73, 132].

The use of an array of four LPs allows to reconstruct an estimate of the real wavenumber vector in space, the *sample local wavenumber* $\boldsymbol{\kappa}(f) = (\kappa_\zeta, \kappa_\alpha, \kappa_\theta)$ – with $f = \omega/2\pi$ the linear frequency – obtained by means of the Two-Points Power Spectral Density (PSD2P) technique [127, 128]. The PSD2P consists in cross-correlating the signal of the reference

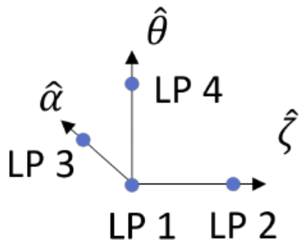

Figure 4.2: Schematic of the LP probe array, with the probe tips represented by blue dots and each probe labeled. The local reference frame $(\hat{\zeta}, \hat{\alpha}, \hat{\theta})$ is also drawn alongside in black, for clarity. The probes *LP 1* and *LP 2* are aligned along the direction $\hat{\zeta}$, which approximates at all times the parallel direction to the local magnetic field lines.

LP, labeled as *LP 1*, which is placed at the front in a central position, with the signals of the other three probes, each one displaced along a different direction of the local frame $(\hat{\zeta}, \hat{\alpha}, \hat{\theta})$ defined before. Namely, *LP 2* allows to obtain κ_ζ, *LP 3* is used to obtain κ_α, and *LP 4* yields κ_θ. **The separation distance between each probe tip and the reference tip, which is equal to 10 mm along each direction, allows for the resolution of wavenumbers in the range $[-314, 314]$ rad/m. A separating distance of 10 mm is carefully chosen in order to minimize the possibility for the sheaths of two different probes to interact, since it is much greater than the largest Debye length in the explored domain and for all operating conditions ($\lambda_D < 1.1$ mm).** A schematic of the LP tips, with their labels and the local reference frame, is drawn in Figure 4.2. The direction $\hat{\zeta}$, along which *LP 1* and *LP 2* are aligned, is meant to approximate at all times the parallel direction of the local magnetic field lines. The error for this approximation was found to be about 5 degrees at worst, at $\alpha = 30$ deg and $\zeta = 130$ mm.

4.2.2 Curling probe

A curling probe is used to measure the electron density number ($N_{e,CP}$) inside the plasma. The CP is a microwave resonant probe consisting of a spiral resonator whose resonance frequency depends on the relative permittivity of the medium in which the probe is immersed. When the probe is immersed in a plasma, its resonance frequency (f_r) increases with respect to its reference value in vacuum (f_0). The electron density n_e can then be directly inferred from the frequency shift using [179] as

$$n_e = \frac{4\pi^2 m_e \epsilon_0}{e^2}(1+\alpha)(f_r^2 - f_0^2), \tag{4.1}$$

where α is a calibration coefficient, m_e the electron mass, e the elementary charge, and ϵ_0 the vacuum permittivity. The CP used in this work is called CP700: it has a spiral resonator length of 110 mm and a diameter of 10 mm. This CP has a vacuum resonance frequency around 880 MHz and it enables accurate measurements of plasma densities in the range $\simeq 8 \times 10^7 - 10^{10}$ cm^{-3}. We note that these values are given in terms of raw densities, i.e., the measured values that are affected by the plasma sheath effect. All density measurements presented here are corrected for the presence of the plasma sheath in front of the probe as detailed in [180]. Uncertainties on the raw measured density values are estimated following the method detailed in [179].

The resonance frequency of the probe is measured every 5 μs, enabling a 200 kHz sampling frequency of the electron density measurement. The CP is placed roughly 2.5 cm downstream the *LP 1* and is integral with the LP array, as can be seen in Figure 4.1. This position is chosen to minimize possible CP perturbations on the LP tips. The CP measuring surface is oriented in such a way to maximize the possibility to capture both azimuthal and axial density oscillations.

4.2.3 High-speed camera

The high-speed camera is positioned outside of the vacuum vessel and is imaging the thruster from the far-end window of the vacuum vessel, directly in front of the plasma source. The model is a Phantom v711, 12 bit resolution, running at 210 kHz with a 128 × 128 pixels image. The camera is set with a 107 mm fixed focal lens with a large opening of 2.8. The focal point is set at the thruster backplate, with the depth of field being a few centimeters. Due to the mounting of the camera, the light collected is averaged along the line of sight. However, experiments led with the camera imaging the thruster with a 45 and a 90 degrees angle, looking through lateral ports of the vacuum vessel, showed that the light produced by the plasma is very faint except in the first 1 cm downstream from the backplate, due to the very low pressure and very low plasma density in the thruster plume. The camera is therefore imaging only this first centimeter of plasma even when facing the thruster. No optical filter is used and the light in all the camera spectral sensitivity is contributing to the analyzed signal.

The acquired movies are analyzed over the first 1000 frames, granting a frequency resolution range of $[0.42, 105]$ kHz. Time-averaging of the entire movie is first computed, and the resulting image is subtracted to each frame in order to isolate light fluctuations. The obtained frames are then analyzed using POD [109–112], previously employed to study plasma fluctuations in different plasma experiments [117, 181] and simulations [172]. This data-driven method allows to decompose a movie into its dominant spatial and temporal components (the POD modes), without any *a priori* assumption upon their shape. This only requires a small additional computational cost with respect to a Fourier decomposition. In the next sections, the computed modes contributing to the plasma fluctuations that will be displayed are only those with a relative energy content higher than 1.5%. The camera diagnostic also allows to verify that shifting the probes position in the thruster plume does not modify the observed plasma fluctuations.

4.2.4 Thruster operating parameters

Additionally, three thruster parameters are recorded to monitor its operation: the forward microwave power (P_{fwd}), the reflected microwave power (P_{ref}), and the thruster floating potential (U_p). The forward power is estimated using a directional coupler placed on the forward power line coming from the microwave power generator with a RF power detector diode. The power reflected from the thruster, which is typically between 1 and 10% the forward power, is sent to a dedicated power line terminated by a 50 Ω load using a circulator. The reflected power is evaluated on this line using a second directional coupler and a RF power detector diode. The model of the two RF detectors is a JFW-50D-052 diode, with a cut-off frequency well above the oscillation frequencies measured in this work. The power deposited in the plasma is computed as $P_d = P_{fwd} - P_{ref}$. The thruster outer conductor floating potential is measured directly through a voltage divider bridge. These three variables are simultaneously recorded with an 8-bit oscilloscope at 20 MHz acquisition rate.

4.3 Results

This section presents the time-resolved measurements collected with the three diagnostics. In the following, the nominal operating condition of the thruster is to be intended for $P_d = 30$ W of power deposited into the plasma, an injected mass flow rate of $\dot{m} = 1.4$ sccm, and a microwave driving frequency equal to $f_{mw} = 2.45$ GHz.

It is worth to note that time-averaged measurements of the plasma density, the electron temperature, and the plasma potential have been collected with the LPs operated in sweeping mode and with the CP at the same positions of the time-resolved measurements. A good agreement has been found with previous measurements on this thruster prototype [182, 183]. Those measurements are not shown here.

4.3.1 Thruster parameters

Figure 4.3 shows the power spectral density (PSD) of the signals recorded during the experimental campaign at (a) 1.4 sccm and (b) 1 sccm. The probe measurements are collected at $\zeta = 70$ mm and $\alpha = 0$ deg.

At $\dot{m} = 1.4$ sccm, all signals show a visible low-frequency peak around 9 kHz, as seen in Figure 4.3-(a). In addition, electron density, LP floating potential, and thruster floating potential display a second, higher-frequency peak at around 60 kHz. This indicates that two distinct plasma oscillations exist in the plume, which will be referred to in the remaining of the paper *low-frequency* and *higher-frequency* oscillations, respectively. In particular, a very good agreement in the value of the oscillation frequency and the PSD shape is observed among $N_{e,CP}$, U_p, and $V_{f,LP}$. The peak-to-peak amplitude of the oscillations is summarized in Table 4.1 for all signals. The relative amplitude of the electron density and the reflected power is comparable (22% and 20%, respectively), as is that of the thruster potential and the LP floating potential (10% and 8%, respectively). On the other hand, the relative amplitude of the forward power signal at 9 kHz is very small, with values well below 1%.

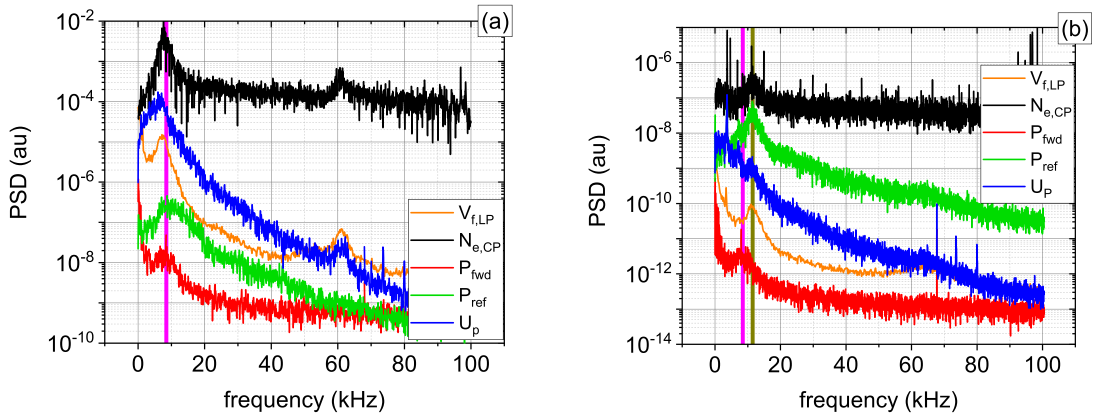

Figure 4.3: PSD of the five signals recorded during the measurement campaign: LP floating potential ($V_{f,LP}$, orange line), electron density measured with the CP ($N_{e,CP}$, black line), forward power to the thruster (P_{fwd}, red line), reflected power from the thruster (P_{ref}, green line), and thruster floating potential (U_p, blue line). All quantities are plotted in arbitrary units on the y-axis to aid visualization and avoid line overlapping. (a) 1.4 sccm, (b) 1 sccm.

Table 4.1: Peak-to-peak oscillation amplitude at 9 kHz of the quantities shown in Figure 4.3-(a) at 1.4 sccm. Each value is normalized by the respective mean value of the recorded time series.

measured quantity, A	pk-pk amplitude $\Delta A/\bar{A}$
P_{fwd}	$\leq 1\%$
P_{ref}	$\simeq 20\%$
U_p	$\simeq 10\%$
$N_{e,CP}$	$\simeq 22\%$
$V_{f,LP}$	$\simeq 8\%$

In order to answer the question about whether the observed low-frequency plasma oscillation at approximately 9 kHz is due to the forward power (i.e., it is introduced by the power supply) or it is induced by the plasma, we analyze their relationship more in detail.

First, forward and reflected power without plasma ignition were recorded. In such case, the microwave power reaches the coaxial thruster chamber: a small part is radiated from the thruster, while the remaining power is reflected back to the line and dissipated through a 50 Ω load. Results indeed indicate the existence of some power concentration at around 9 kHz in the PSD of the P_{fwd} signal. This frequency is close to the values of the low-frequency plasma oscillation obtained for 1.4 sccm (see the pink vertical line in Figure 4.3-(a)).

On the other hand, when different operating conditions are inspected, the low-frequency peak observed for the plasma related quantities is not at 9 kHz, as is shown for instance in Figure 4.3-(b) for $\dot{m} = 1$ sccm. In this case, the low-frequency oscillation peaks in correspondence to the gold vertical line, located at $\simeq 12$ kHz, whereas the peak of P_{fwd} remains at 9 kHz, highlighted once again by the pink vertical line. The dependency of the fundamental frequency of the low-frequency oscillation on the thruster operating conditions points in the direction of a plasma-driven oscillation. It appears however that the power supply employed in this work introduces a $\simeq 9$ kHz fluctuation of the input power due to ripple. At a flow rate of 1.4 sccm, the fundamental frequency of the low-frequency plasma-driven oscillation approaches 9 kHz, and a resonance may occur. Indeed, the largest amplitude of the low-frequency mode is experimentally observed for 1.4 sccm, which is the reason why this operating condition was taken as nominal throughout this study.

In conclusion we deduct from experimental evidence that the low-frequency oscillation observed is not induced by the power supply, but is rather plasma-driven. Nevertheless, it is likely that the oscillation interacts with the 9 kHz ripple of the power supply when the mass flow rate is equal to 1.4 sccm, and that the two resonate for this condition. Further measurements with different power supplies will be performed to assess the validity of this hypothesis.

4.3.2 Langmuir probes

Langmuir probe results are shown in Figure 4.4, where the PSD spectrum of the signal collected by the *LP 1* is shown at different angular positions α and at two different axial positions: (a) $\zeta = 70$ mm and (b) $\zeta = 130$ mm, for the nominal operating condition. Firstly, results show the predominant low-frequency oscillation around 9 kHz, consistently visible for all investigated positions. The higher-frequency oscillation is also detected falling in the 60–70 kHz range, generally possessing lower magnitudes with respect to the low-frequency one. Comparison of the spectra shows how both the strength and the dominant frequency of the 9 kHz $V_{f,LP}$ fluctuation remain roughly unaffected by the investigated spatial position. On the contrary, whilst the 60–70 kHz oscillation appears to consistently fall within the same range of frequencies, its intensity seems to have a dependency upon the angular position, getting slightly stronger for higher values of the coordinate α, but being generally visible everywhere.

Figure 4.5 shows the PSD of the *LP 1* signal when varying the thruster operating conditions, in terms of (a) mass flow rate, (b) power deposited in the plasma, and (c) microwave driving frequency. The LP array is located at $\zeta = 130$ mm and $\alpha = 20$ deg. Additionally, Figure 4.5-(d) shows the PSD spectra obtained from measurements collected on different days of testing to assess repeatability. The measurements in (d) are

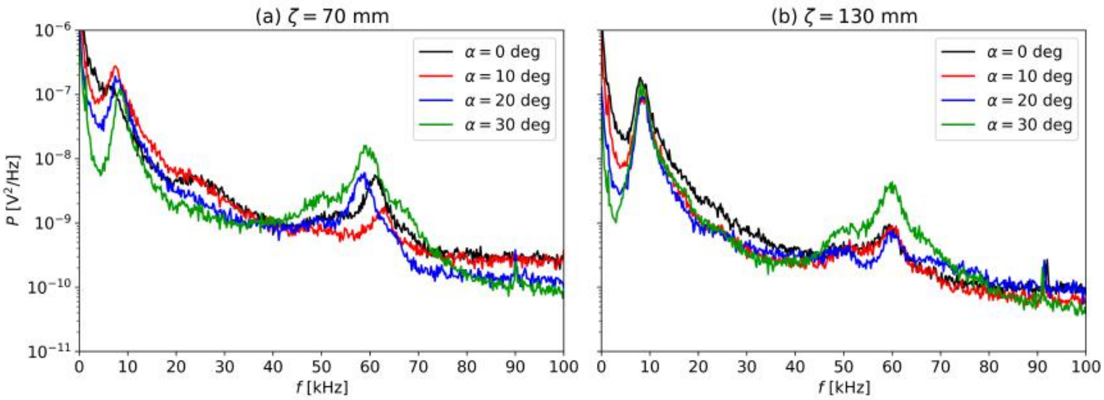

Figure 4.4: PSD of the *LP 1* signal collected at different angular positions, at (a) $\zeta = 70$ mm and (b) $\zeta = 130$ mm. For both (a) and (b), $\dot{m} = 1.4$ sccm, $P_d = 30$ W.

taken along the centreline, namely at $\zeta = 130$ mm and $\alpha = 0$ deg.

As shown in Figure 4.5-(a), the low-frequency oscillation is clearly visible with a well defined peak at 1 sccm, around 12 kHz, and at 1.4 sccm, around 9 kHz, for which the amplitude is highest. When the flow rate is increased beyond 1.4 sccm, the amplitude of this oscillation is seen to gradually decrease. More precisely, by means of previous acquisitions that will not be shown in this paper, this oscillation was detected from $\dot{m} = 0.8$ sccm up to roughly 1.6 sccm, always centered between 5 and 12 kHz. For $\dot{m} \geq 2$ sccm, the low-frequency oscillation tends to disappear and only a small plateau can be seen slightly below 10 kHz. The higher-frequency oscillation is generally visible at around 60, 45, 25 kHz when increasing the flow rate from 1 to 2.2 sccm, with varying amplitude.

Variations of the input power P_d, as displayed in Figure 4.5-(b), have a much milder effect on the observed dynamics. The dominant frequency of the low-frequency oscillation is slightly increased to 11 kHz when decreasing the power to 13 W. Conversely, for this same value of P_d, the amplitude of the high-frequency oscillation is reduced by around a third compared to the 30 W power level. For $P_d = 33$ W, the low-frequency oscillation is not changed, whereas the higher-frequency one shows a small shift of its dominant frequency.

Variations of the input microwave frequency appear to have a major impact on the intensity of both the low and higher-frequency oscillations, as shown in Figure 4.5-(c). Specifically, reducing the microwave frequency to 2.00 GHz does not massively change the frequency of the main low-frequency peak, which remains roughly in proximity of 9 kHz, but it increases its amplitude by at least two orders of magnitude. Five harmonics of the main frequency are also observed. The higher-frequency oscillation instead disappears entirely for this condition. On the other hand, increasing f_{mw} to 2.60 GHz has the opposite effect, remarkably damping the low-frequency oscillation in magnitude. The amplitude of the higher-frequency oscillation is significantly enhanced by approximately two orders of magnitude compared to the nominal 2.45 GHz case.

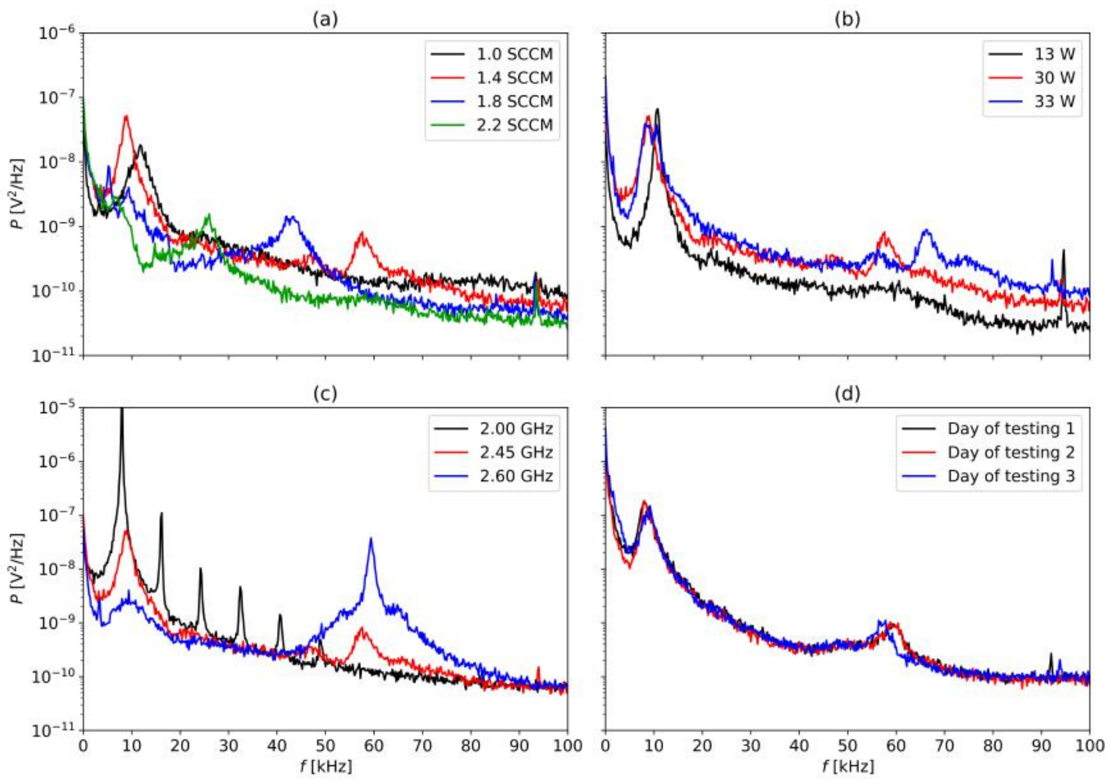

Figure 4.5: PSD spectra of the signal collected by the *LP 1* for variations, with respect to the nominal operating condition, of (a) mass flow rate, (b) power deposited in the plasma, and (c) driving frequency. All the scans in (a)–(c) are obtained at the same spatial position given by $\zeta = 130$ mm and $\alpha = 20$ deg. Lastly, (d) displays the repeatability of the measurements, for the nominal operating condition, by means of independent acquisitions performed during different days of testing, at $\zeta = 130$ mm and $\alpha = 0$ deg.

Finally, measurement consistency is assessed in Figure 4.5-(d), where the PSD extracted from the signals collected by the *LP 1* on different days of testing is illustrated. The operating condition is the nominal one, with the LP array located at $\zeta = 130$ mm and $\alpha = 0$ deg. PSD spectra show very good repeatability: the low and higher-frequency oscillations are visible at the same frequencies (at around 9 and 60 kHz, respectively) and with the same magnitude.

Application of the PSD2P technique allows for the computation of the experimental dispersion diagrams $\kappa - f$, providing further insight into the observed low and higher-frequency dynamics. These dispersion diagrams are shown in Figure 4.6 for all three spatial directions, with the LP array located at $\zeta = 130$ mm and $\alpha = 30$ deg, a position for which both the low and higher-frequency oscillations show large amplitudes, and for the nominal operating condition. The colorbar reports the value of the *magnitude-squared coherence* (MSC) $r(f)$ [184], which is computed along each direction. The dispersion diagrams display very high values of coherence in proximity to the characteristic frequencies at which the two main oscillations take place, namely around $f = 9$ kHz and 60 kHz, suggesting that a wave is present. Around those frequencies, where the MSC

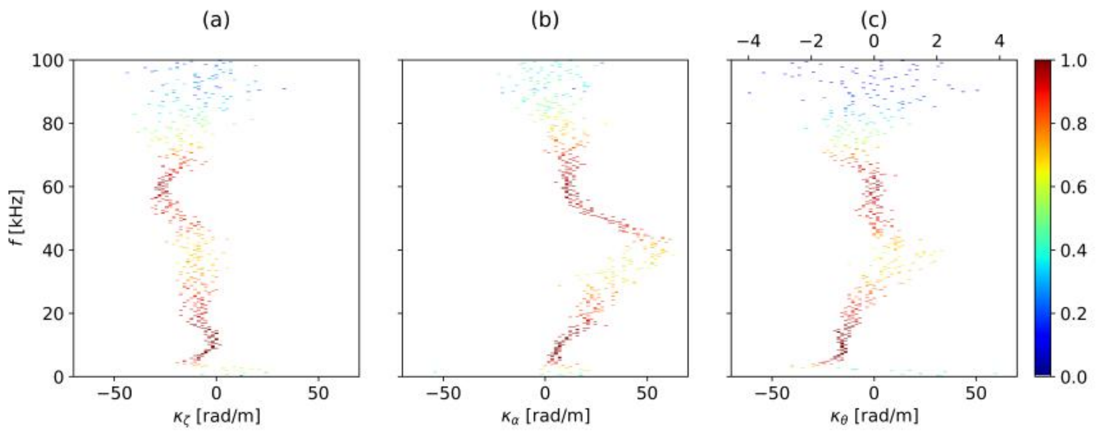

Figure 4.6: Experimental dispersion diagrams for the nominal operating condition, at $\zeta = 130$ mm and $\alpha = 30$ deg, obtained by means of the PSD2P technique. The three sample local wavenumber components $\kappa(f)$ are displayed, namely along the directions (a) $\hat{\boldsymbol{\zeta}}$, (b) $\hat{\boldsymbol{\alpha}}$, and (c) $\hat{\boldsymbol{\theta}}$. The colorbar represents the corresponding values of the MSC $r(f)$. An additional x-axis is drawn on top of panel (c) to report the normalized m modes. Note that the sampled wavenumbers span $[-314, 314]$ rad/m, but the plots are zoomed in the regions of interest.

peaks, the values of the sample local wavenumbers are small. Only the dispersion diagrams along the radial direction $\hat{\boldsymbol{\alpha}}$ and the azimuthal direction $\hat{\boldsymbol{\theta}}$ show a faint right-wise trend for frequencies roughly between 10 and 50 kHz, with the radial trend being slightly more pronounced. Those trends, however, are interrupted right before $\simeq 60$ kHz, where the MSC increases, and κ_α and κ_θ move back to values near the centre of the dispersion plots. Other spatial positions – not reported here for brevity – show comparable behaviors, with generally small values of the local wavenumbers for large values of the coherence.

The signal collected by the *LP 1* is further processed by means of the *bi-coherence analysis* [131]. The bi-coherence analysis provides with a normalized value $b(f_1, f_2)$ between 0 and 1, which estimates the quadratic non-linear interaction intrinsic to the data between a pair of modes at frequencies f_1 and f_2 and a mode at the sum-frequency $f_1 + f_2$. Within the scope of this work, the objective is to use this technique to identify pairs of interacting frequencies (namely, f_1 and f_2) in the context of three-wave coupling.

Figure 4.7-(a) displays the results obtained through application of the bi-coherence analysis for the nominal operating condition, the same as in Figure 4.6. For this case, the extracted values of b are small overall, indicating a generally low level of non-linear interaction. The highest contribution, around $\simeq 0.15$, is found at $(f_1, f_2) \simeq (60, 10)$ kHz, displaying a central region of quasi-null bi-coherence and two sideband regions with higher b, **the first one developing roughly from $f_1 \approx 40$ until 55 kHz, while the second from $f_1 \approx 60$ until 75 kHz, both along $f_2 \approx 10$ kHz**. Sideband structures are typical of signal modulation, which is in fact a type of quadratic non-linear interaction. Such sideband structures are also visible for some positions and/or operating conditions in the

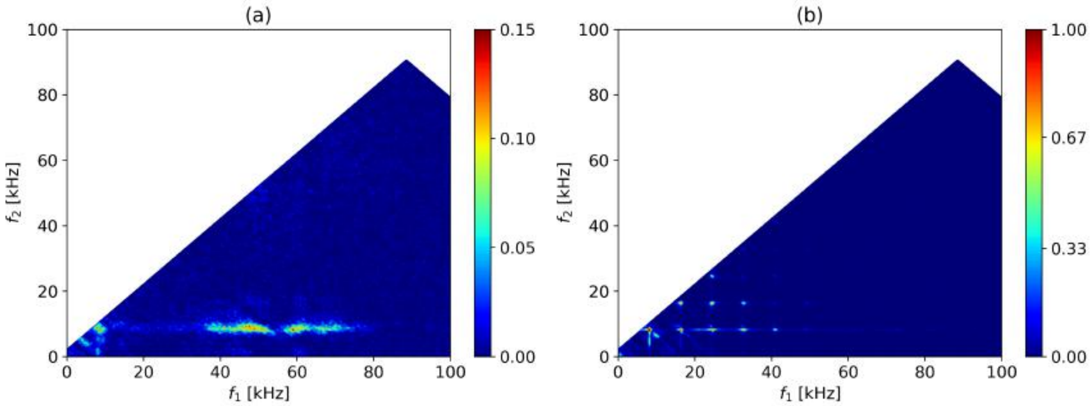

Figure 4.7: Bi-coherence diagrams for the signal collected by the *LP 1* in two different scenarios, namely for (a) ζ = 130 mm, α = 30 deg, $\dot{m}$ = 1.4 sccm, P_d = 30 W, f_{mw} = 2.45 GHz, and for (b) ζ = 130 mm, α = 20 deg, $\dot{m}$ = 1.4 sccm, P_d = 30 W, f_{mw} = 2.00 GHz. Note that the upper limits of the two colorbars are different.

PSD spectra of Figures 4.4 and 4.5, at the two sides of the fundamental frequency of the higher-frequency oscillation. This implies that the higher-frequency oscillation is undergoing modulation on behalf of the low-frequency one.

A much different scenario is recovered for the case depicted in Figure 4.7-(b), for which the overall values of bi-coherence are much higher. The inspected spatial position is ζ = 130 mm and α = 20 deg, while the operating condition is P_d = 30 W, $\dot{m}$ = 1.4 sccm, and f_{mw} = 2.00 GHz. This is the case showing strong harmonic generation for the low-frequency oscillation, as displayed in Figure 4.5-(c). This is confirmed by the strong, localized non-linear interaction detected at values of f_1 and f_2 corresponding to harmonics of the fundamental frequency of the low-frequency oscillation. This implies that the majority of their energy can be explained solely in terms of harmonic generation from the fundamental frequency. Again, this is in contrast with the previous case, where the lower magnitudes of the bi-coherence hinted at weak couplings or energy transfer explained by other processes or plasma instabilities.

4.3.3 Curling probe

Figure 4.8 shows the comparison of the PSD spectra of the CP electron density (black line) and the LP floating potential (orange line) recorded at ζ = 70 mm and (a) α = 0 deg and (b) α = 30 deg, at nominal operating condition. Globally, a good agreement is observed in the values of the low and higher-frequency oscillations (around 9 and 60 kHz) for the CP electron density and LP floating potential signals, especially on the axis (α = 0 deg, Figure 4.8-(a)). At α = 0 deg, the low-frequency magnitude is around 50× above the floor level, whereas the higher-frequency magnitude is around 4× above the floor level. Away from the axis, at α = 30 deg (see Figure 4.8-(b)), the low-frequency peak of the PSD has a lower magnitude (only 8× above the floor level *vs.* ≃ 50× above the floor level for the

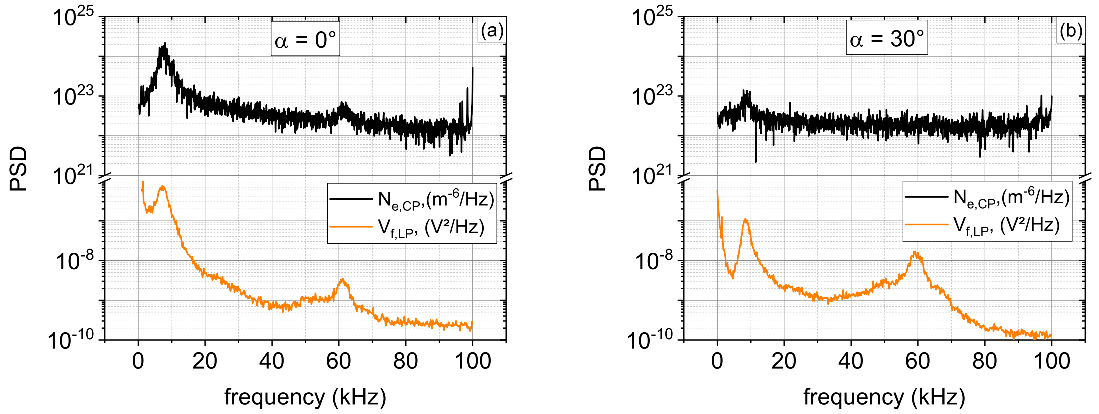

Figure 4.8: Computed PSD of the electron density measured with the CP (black line) and the LP floating potential (orange line) at ζ = 70 mm and (a) α = 0 deg and (b) α = 30 deg.

α = 0 deg case). Moreover, the higher-frequency peak is not detected with the density measurement performed with the CP. This is most likely due to the fact that the amplitude of the 60 kHz density oscillation at α = 30 deg is below the measurable range of the CP utilized in this work.

At α = 0 deg, the average electron density is $\simeq 8 \times 10^9$ cm^{-3} and the peak-to-peak amplitude of the low-frequency oscillation is $\simeq 1.3 \times 10^9$ cm^{-3}, yielding a ratio $\Delta N_{e,pk-pk}/\bar{N}_e \simeq 17\%$. When moving out of the centreline, at α = 30 deg, the average electron density and the peak-to-peak amplitude of the low-frequency oscillation are $\simeq 1.5 \times 10^9$ cm^{-3} and 10^9 cm^{-3}, respectively, which corresponds to $\Delta N_{e,pk-pk}/\bar{N}_e \simeq 70\%$. Assuming that the magnitude of the higher-frequency oscillation is consistently approximately 10× lower than that of the low-frequency one, as for the α = 0 deg case, then the (raw measured density) amplitude of the higher-frequency oscillation would be $\simeq 10^7$ cm^{-3}, well below the measurable density range of the probe.

Access to direct measurements of the electron density mean value and fluctuations amplitude is of particular interest when performing theoretical predictions of classical and anomalous transport coefficients [78]. For example, the relative density amplitude $\Delta N_e/\bar{N}_e$ can be used to estimate an effective electron resistivity related to cross-field particle transport.

Figure 4.9 shows (a) the absolute and (b) the relative peak-to-peak amplitude of the density fluctuations in time when moving farther away from the thruster for two angular positions, α = 0 deg and α = 30 deg, at nominal operating condition. The absolute density amplitude, shown in Figure 4.9-(a), globally decreases with distance to the thruster for the two angular positions. Moreover, for ζ < 12 cm it is larger on the axis than at α = 30 deg. For ζ > 12 cm the amplitude on the axis is comparable to that away from the axis. The relative density amplitude, shown in Figure 4.9-(b), is much larger at α = 30 deg than at α = 0 deg for all distances, with values around 70% and 20% at α = 30 deg and α = 0 deg, respectively. In addition, the relative amplitude decreases from 80% to 60% with the distance to the thruster in the α = 30 deg case, whereas at α = 0 deg it slightly

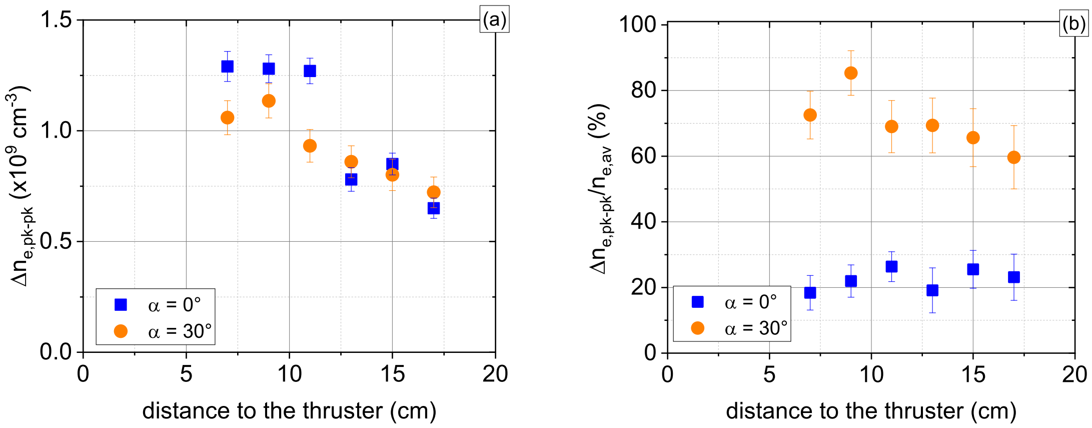

Figure 4.9: (a) Density oscillation absolute amplitude and (b) density oscillation amplitude normalized by the average density, at various distances from the thruster exit plane. For both (a) and (b), the blue scatter points represent measurement points along the thruster symmetry axis, whereas the orange scatter points represent off-axis measurements.

increases from 20% to 25%.

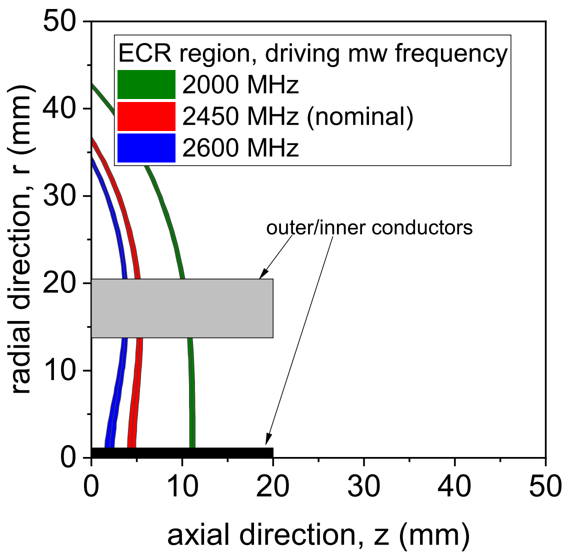

Figure 4.10: **ECR regions for the three driving microwave frequencies tested in this work: 2000, 2450 (nominal case), and 2600 MHz.**

Last, we show the influence of the microwave driving frequency on the amplitude and frequency values of the low-frequency density oscillation in Table 4.2. Globally, the amplitude of the density oscillations decrease when increasing the driving frequency value. When the microwave frequency is decreased from the nominal value (2450 MHz) to 2000 MHz, therefore moving the ECR region downstream inside the thruster source (see Figure 4.10), the absolute amplitude of the oscillation increases by 1.6× and the relative one by almost 4×. When the driving frequency is increased to 2600 MHz, corresponding to an ECR region much closer to the thruster backwall, as shown in Figure 4.10, the abso-

Table 4.2: Amplitude of the density oscillation for the three driving microwave frequencies analyzed in this study (2450 MHz is the nominal case). Data has been collected at $\zeta = 130$ mm and $\alpha = 0$ deg.

Driving frequency [MHz]	$\Delta N_{e,pk-pk}$ [$\times 10^9$ cm^{-3}]	$\Delta N_{e,pk-pk}/\bar{N}_e$ [%]
2000	1.3 ± 0.07	72 ± 5
2450	0.8 ± 0.05	19 ± 2
2600	0.5 ± 0.05	11 ± 1

lute amplitude decreases by 1.6× (which is the same amount by which it increases when moving to the 2000 MHz case) and the relative one is decreased by less than 2×.

4.3.4 High-Speed Camera

Firstly, the camera is used to verify that the probe system, comprised of the array of LPs and the CP, does not affect the measured plasma fluctuations. The camera measurements are performed both with the probes outside of the plasma, moving the mechanical arm on the far side of the plume, and with the probes immersed in the plasma, for each position of the probe setup. For fixed operating conditions, the plasma fluctuations collected by the camera are observed to be unaffected while the position of the set of probes is varied. This serves the purpose of verifying that the array of probes does not affect the visible plasma fluctuations, validating the fact that the evolution of the fluctuations observed with the probes can be attributed to local plasma behaviour and not to modification of the thruster operation.

Secondly, the movies collecting fluctuations of the light emitted by the plasma at the nominal operating condition are analyzed, in order to assess their geometrical shape. The first four dominant spatial modes obtained by POD analysis, labeled u_0 to u_3, are displayed with their relative energy contributions, from 77.4% to 2.5%, in Figure 4.11. The first POD mode is almost homogeneous over the thruster diameter and is strongly dominating the other three modes that are not spatially homogeneous. The dominant u_0 mode can be described as a global $m = 0$ mode. The POD modes u_1, u_2, and u_3 present both a radial and an azimuthal inhomogeneity and may be attributed to azimuthal $m = \pm 1$ modes.

Furthermore, the PSD of the temporal evolution of the four dominant POD modes is computed. Results are presented in Figure 4.12, demonstrating that the major spectral contributions captured by both the LPs and the CP can also be found with POD analysis. Additionally, this plot confirms the prevalence of mode u_0, showing a peak at 9 kHz that is one order of magnitude larger than the second largest peak reached by the mode u_1. **The peak captured around 60 kHz by the LPs and the CP is also present on the PSDs of modes u_3 and, with smaller magnitude, u_0. Conversely, it is not detected at all by modes u_1 and u_2.**

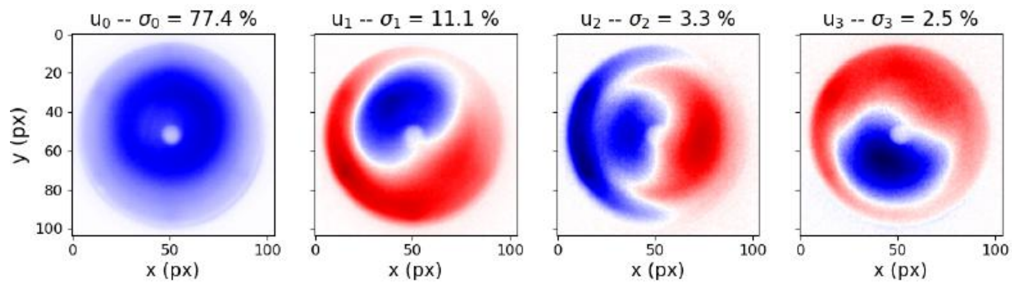

Figure 4.11: Dominant spatial modes obtained by means of the POD technique applied to the signal of the high-speed camera for the ECR thruster operated at nominal condition.

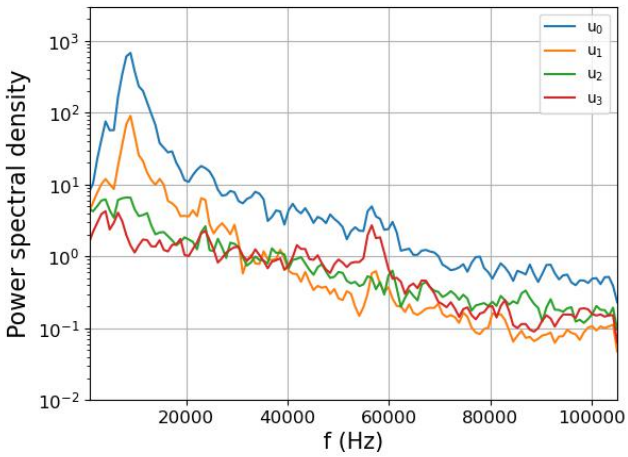

Figure 4.12: PSD of the temporal evolution of the four dominant modes obtained with the POD technique applied to the high-speed camera signal for the ECR thruster operated at nominal condition.

4.4 Discussion

Globally, results from the three independent diagnostics, namely an array of LPs, a CP, and a high-speed camera, evidence the presence of two plasma oscillations, at around 9 kHz and 60 kHz, in the plume and in the plasma source of the investigated ECR thruster prototype. In the following, we will discuss the two oscillations separately.

4.4.1 The low-frequency oscillation

The low-frequency oscillation was found to fall in a range of frequencies between 5 and 12 kHz, with an intensity mostly affected by changes in the mass flow rate and the microwave driving frequency (see Figure 4.5-(a) and (c)). POD analysis of the light captured by the camera suggested that this oscillation carries most of the energy, with a predominant $m = 0$ global mode structure (Figure 4.11). Indeed, the experimental dispersion diagrams shown in Figure 4.6 displayed a small propagation in space in correspondence to its fundamental frequency. In this case, the electron density was seen to oscillate with a peak to peak amplitude amounting to a significant fraction of its average value.

These observations suggest that this oscillation may be related to an ionization type of dynamics. Ionization processes have already been shown to induce low-frequency plasma oscillations in other electric propulsion devices, such as in Hall effect thrusters, in which they are often referred to as *breathing oscillations* [66, 67], in magnetic nozzle thrusters [80, 82], and more particularly in ECR thrusters [81]. In addition, this kind of oscillations has also been observed in other plasma sources, such as in ECR sources [169] and in hollow cathodes [170,171]. Breathing oscillations are often found to strongly modulate the plasma dynamics and are generally observed at multiple positions within the plume [125, 185]. Furthermore, they tend to have a global behavior, with little to no propagation [65, 172], and their characteristic frequencies fall in the 5–50 kHz range [173].

A simple model describing breathing oscillations is the predator-prey model, originally developed by Fife *et al.* [65] in the context of Hall thrusters, and later revisited in refs. [68, 69]. According to its simplest formulation, it relies on a global analysis of 0D continuity equations for ions and neutrals, localized within a confined ionization region of length L. The solution of this system of equations is a standing wave with an oscillating frequency, representing the hybrid residence time of ions and neutrals within the chamber, defined as

$$\omega = 2\pi f = \frac{\sqrt{v_n v_i}}{L}, \tag{4.2}$$

where v_i and v_n are the ion and neutral characteristic velocities in the ionization region, respectively. Neutrals are assumed to be at room temperature, yielding $v_n \approx 138$ m/s in the case of xenon. The ion velocity is inferred from previous measurements on a similar thruster prototype [182]: at 10 mm from the backplate and for different values of the mass flow rate, typical values of v_i are between 1700 and 2800 m/s. If the characteristic ionization length is taken equal to $L = 10$ mm [183], the theory predicts frequencies falling between 7 and 10 kHz, which are close to the values measured in this work for the low-frequency oscillation.

The variation of the forward power to the thruster does not seem to induce major effects other than slightly shifting its fundamental frequency. On the other hand, the variation of the driving microwave frequency impacts the amplitude of the low-frequency oscillation by several orders of magnitude, as displayed in Figure 4.5-(c) and reported in Table 4.2. One preliminary explanation for this strong shift in amplitude can be attributed to the fact that the ECR region moves along the chamber while the driving microwave frequency changes. For a visual representation of the position of the three ECR regions for the three driving frequencies tested in this work, refer again to Figure 4.10. The position of the ECR region can potentially have a non-negligible impact upon the ionization process and ultimately affect the corresponding ionization efficiency. This, in turn, may further support the theory attributing the low-frequency oscillation to an ionization-related process.

4.4.2 The higher-frequency oscillation

For what concerns the higher-frequency oscillation, it was shown in Section 4.3.2 how its intensity seemed to be slightly enhanced when moving towards the edge of the plume, but being this oscillation also detectable along the axis (see Figure 4.4) and in the thruster source (through the high-speed camera measurements, see Figure 4.12). Its fundamental frequency showed an important dependency on the injected mass flow rate, gradually moving to lower frequencies when increasing $\dot{m}$ (see Figure 4.5-(a)). The spatial structure identified by means of the PSD2P technique involved generally small values of the wavenumbers around 60 kHz, with some trends, though faint, along the radial and azimuthal directions. POD modes with noticeable energetic contributions at 60 kHz also exhibited some azimuthal and/or radial structure, but proper isolation of this oscillation was prevented by mode interplay. Finally, bi-coherence analysis underlined weak nonlinear interaction of the higher-frequency oscillation with the low-frequency oscillation in the form of signal modulation.

Several recent studies report the existence of oscillations in the peripheral region of various devices employing MNs. Notably, evidence of broadband oscillations with azimuthal propagation was reported by Hepner *et al.* [78] in an ECRT device with a design similar to the one employed in this study. The oscillation was attributed to a Lower-Hybrid Drift Instability, a collisionless, kinetic type of instability that takes place in the lower-hybrid frequency regime. Takahashi *et al.* [79] also reported azimuthally rotating oscillations in the periphery of a MN, with typical frequencies in the 40–50 kHz range, this time employing a Helicon Plasma Thruster. The oscillation was attributed to a magnetosonic wave, corresponding to a compressional Alfvén wave. Additional evidence of broadband azimuthal oscillations developing in the periphery of the plume of a Helicon Plasma Thruster, falling around 50 kHz, was reported in [186]. The oscillation was seen to possess features that are typical of a lower-hybrid type of wave. The characteristic frequencies reported in those studies are close to the characteristic frequency of the higher-frequency oscillation found in this work, typically around 60 kHz. The lower-hybrid frequency, instead, is typically found to fall a few times above that value, roughly between 200 and 300 kHz.

4.5 Conclusions

In this work, plasma oscillations in the MN of a coaxial ECRT device were experimentally detected and characterized. The experimental acquisitions were collected by means of three different diagnostics: an array of LPs, a CP, and a high-speed camera. All diagnostics collected data simultaneously.

The results obtained independently with the three diagnostics showed good agreement. The experimental findings allowed to detect two separate oscillating phenomena, one at low frequencies, typically below 15 kHz, and a second one taking place around

60 kHz. The dependency of these two oscillations on changes of the thruster operating condition and the probe position within the plasma plume was investigated.

The low-frequency oscillation was observed almost everywhere in the plume with similar intensity, displaying a fundamental frequency that, depending on the operating condition, always fell between 5–12 kHz. The oscillation was seen to possess a predominant $m = 0, -1$ azimuthal structure, and electron density was seen to fluctuate accordingly with a significant fraction of its average value. The higher-frequency oscillation was also seen almost everywhere, with a slight dependency on the inspected spatial position. Changes in the power deposited into the plasma did not affect, in a major fashion, the features of the observed oscillations. Conversely, variations of the mass flow rate and the microwave driving frequency did affect their strength and fundamental frequency in a remarkable way.

The possibility that the low-frequency oscillation be induced by an ionization instability was suggested and a plausible agreement of the physics observed experimentally with expected characteristic frequencies was found. Conversely, the higher-frequency oscillation was seen to fall in a range of frequencies that resembles existing evidence of various phenomena observed in other or similar devices [78, 79, 186]. Further analysis of the data and additional testing will be performed in order to confirm the validity of the formulated hypotheses and advance the understanding of the two detected oscillations.

5. CONCLUSIONS

Within this chapter, Section 5.1 draws the major contributions of this thesis, whereas Section 5.2 outlines potential future lines of research.

5.1 Main contributions

This dissertation analyzes plasma oscillations developing in the plumes of various devices employed for space propulsion. The investigated thrusters span from more mature technologies still offering room for open research topics, such is the case of Hall Effect Thrusters (HETs), to novel devices in which this type of investigation is relatively recent, like Helicon Plasma Thrusters (HPTs) and Electron Cyclotron Resonance Thrusters (ECRTs), both belonging to the category of Electrodeless Plasma Thrusters (EPTs) employing Magnetic Nozzles (MNs). Several diverse data-driven techniques are successfully employed to tackle the problem, from modal analysis to spectral description, depending on the type of data at hand and the intended objectives. Each chapter focuses on a different device.

Chapter 2 analyzes simulation data of a Stationary Plasma Thruster (SPT)-100-like HET. The 2D maps of the plasma density, the neutral density, the electron temperature, the plasma potential, and the axial ion current density are postprocessed through cross-application of Proper Orthogonal Decomposition (POD) and Higher Order Dynamical Mode Decomposition (HODMD) thanks to the large spatial resolution available by means of the simulations. Application of POD yields an energy-based decomposition, useful for noise filtering and dimensionality reduction, which is unable to successfully uncouple the different dynamics. Conversely, HODMD cleanly isolates the dominant oscillations in the 1-120 kHz range, namely the breathing and ion-transit time (ITT) modes, by decomposing the original data into non-orthogonal, dynamically relevant HODMD modes. Two clusters of such modes are identified for the two oscillations, which are eventually separately reconstructed. This allows to reveal a predominant standing wave structure of the breathing mode for plasma density, neutral density and ion current density inside the thruster, and an axially progressive-wave structure for the electron temperature and plasma potential in the near plume. Conversely, the ITT mode exhibits an essentially downstream traveling structure for all plasma variables. Results of the phase difference between plasma density and neutral density for the breathing mode agree well with the predator-prey model, whereas the ITT mode phase velocity corresponds with the average ion velocity in the acceleration region. Changes in the mass flow rate and discharge voltage are also discussed in order to inspect their impact upon the two observed oscillations. By decreasing the discharge voltage, the amplitude of the breathing oscillations weakens, becoming comparable to that of the ITT dynamics. HODMD retains more modes, resulting in more complicated oscillations. Conversely, increasing the mass flow rate lowers the number of modes needed to model them, and therefore suggests spectrally simpler oscillations. Otherwise, apart from a slight modification of the dominant frequencies of the two oscillation types, the spatial structure of the involved HODMD modes and the overall behavior of the discharge remain qualitatively the same in the explored parameter ranges. This chapter illustrates the significance of some modal analysis techniques, like HODMD, to isolate different oscillation mechanisms, while also highlighting the potential of data-driven techniques as a whole in the context of plasma flows relevant to electric propulsion. This provides an unprecedented look upon two fundamental oscillations that characterize Hall thrusters, allowing to separately visualize and characterize each one of them, and avoiding mixing of the two behaviors.

Chapter 3 moves onto the analysis of experimental data. Plasma oscillations $\leq$ 1 MHz in the MN of a HPT prototype are studied employing an array of three floating Langmuir probes (LPs), for two different values of xenon injected mass flow rate, namely 5 and 10 sccm. The LPs are displaced in space in order to reconstuct the wavevector of the waves in the parallel and azimuthal directions with respect to the magnetic field. For this purpose, a custom-made version of the Two-Points Power Spectral Density (PSD2P) algorithm is used, cross-correlating the signals collected by two different probes to extract an experimental sample of the local wavenumber, whereas coherence analysis allows to assess the statistical significance of the phase difference between the signals of the LPs. A low-frequency oscillation – around 4 kHz – appears in proximity of the thruster exhaust, displaying negligible propagation in space, and slightly enhanced when increasing the mass flow rate. This oscillation is likely the result of a breathing/ionization instability at the source, with the predator-prey model predicting comparable frequencies. Additionally, a broadband, azimuthally-propagating structure develops near the edge of the plume, extending to roughly $\simeq$ 200 kHz, possessing phase velocities in the 10^3–10^4 m/s range, near the ion sound velocity. High-coherence power peaks are found at $\simeq$ 50 kHz within this band, while weaker ones are found at $\simeq$ 100 kHz for some locations. The parallel wave number is small, and below ± 20 rad/m in the majority of the plume. The azimuthal dispersion diagrams show a clear, almost-linear trend along the diamagnetic direction for the 5 sccm case at mid-angle positions. The 50 kHz and the 100 kHz peaks, when visible, fall along the negative m_θ trend line, suggesting they are part of the same broadband spectrum; the 4 kHz, however, does not, reinforcing the idea that this feature may belong to a entirely different dynamics. For other positions farther away from the thruster centreline, and when the mass flow rate is increased to 10 sccm, the linear trend in the azimuthal direction is less clean, and the coherence decreases. Application of bi-coherence analysis allows to rule out phase coupling within the $<$ 200 kHz frequency range, but points at a parametric decay instability of the pump Helicon wave as a plausible explanation for the broadband, ion-acoustic-like spectrum. This second chapter aims to contribute to a better understanding and characterization of plasma oscillations taking place in EPTs that employ MNs, for which to this day a prevalent theory is still lacking. To achieve this, data-driven algorithms for spectral analysis are employed to both reveal the wave structure underlying the experimental data and assess hidden features of the data itself.

An additional effort in the same direction is represented by Chapter 4, in which an improved experimental setup based on the one described in Chapter 3 is employed to study oscillations in the MN of an ECRT device. For this campaign, four LPs are designed, now allowing to resolve the wavenumber along the perpendicular direction to the magnetic field as well, in addition to the ones along the parallel and azimuthal directions. Alongside the array of floating LPs, a Curling Probe (CP) allows to gather time-resolved measurements of the electron density, whereas a high-speed camera collects the fluctuations of the light emitted by the plasma in the source. Data of the LPs are postprocessed once again employing the PSD2P technique, whereas the high-speed camera imaging allows for the use of POD due to its larger spatial resolution. Additionally, the data collected by the LPs is further exploited to perform once again coherence and bi-coherence analysis. The study detects two different oscillations: one at frequencies near 9 kHz and a second one around 60 kHz, labeled low-frequency oscillation and higher-frequency oscillation, respectively. The study covers several spatial positions within the plume as well as various operating conditions, changing the xenon injected mass flow rate, the deposited power into the plasma and the driving frequency of the microwave generator. Both oscillations show their fundamental frequencies and amplitudes visibly affected by changes in the operating condition, mostly by the injected mass flow rate and the microwave driving frequency. The spatial position, on the contrary, does not have a major impact other than slightly enhancing the amplitude of the higher-frequency oscillation, and both oscillations are visible everywhere within the plume. The low-frequency oscillation, carrying more than 75% of the total energy, is observed to always fall between 5-12 kHz, with a spatial structure revealed by the LPs and the high-speed camera showing a predominant $m = 0, -1$ wave structure. The fluctuations induced on the electron density by this oscillation amount to a significant fraction of its average value, higher off-axis than on the thruster symmetry axis. Conversely, bi-coherence analysis suggests that the low-frequency oscillation modulates the higher-frequency one, and some inhomogeneities are detected along the radial and azimuthal directions in proximity of the fundamental 60 kHz frequency, and slightly below that. However, a clear identification of the features for the two oscillations is complicated by the existence of mode interplay, especially in the context of POD, as highlighted in Chapter 2. Similarly to Chapter 3, the possibility that the low-frequency oscillation be related to a predator-prey type of instability is explored. The frequencies predicted by this model are, in fact, comparable. Nevertheless, it must be noted that the low-frequency oscillation discussed in this chapter is remarkably visible everywhere within the plume, differently from the very low-frequency oscillation (at $\simeq$ 4 kHz) observed in Chapter 3, which is predominantly seen closest to the plasma source. Differences are found also for the higher-frequency oscillation detected within this chapter and the high-coherence peaks discussed in Chapter 3 (at $\simeq$ 50 kHz), albeit the two are characterized by similar fundamental frequencies. In fact, the oscillation of Chapter 3 is seen to display diamagnetic azimuthal propagation, which is not the case for the oscillation discussed within this chapter. **These discrepancies can potentially be**

explained by several factors, including the intrinsic different architecture of the two devices or the distinct plasma regimes they operate in, which, in turn, can be traced back to the differing operational conditions of the devices. Additionally, for the more specific case of the higher-frequency oscillation detected within this chapter and the high-cohernece peaks found at 50 kHz in Chapter 3, it is important to notice that the parametric-decay instability invoked to explain the latter ones is intrinsically linked to the existence of the pump Helicon wave.

5.2 Future lines of research

The primary objective of future developments is definitely the assessment of the overall effects that the observed oscillations have upon the propulsive performances of the devices studied within this work. It is a known fact that several types of instabilities may develop in axisymmetric $\boldsymbol{E} \times \boldsymbol{B}$ plasmas [35, 36], leading to localized oscillation modes and/or broadband turbulence, which can give rise to enhanced, or anomalous, cross-field transport. The topic of anomalous transport is currently an open question both in HETs and EPTs alike. Estimating the role that plasma oscillations may have in this context can be regarded as the ultimate goal of this types of studies and certainly represents a significant future research direction that can build upon the results of this thesis.

Nevertheless, in order to assess the induced cross-field anomalous transport and the overall impact that these oscillations may have on the thruster performances, it is surely beneficial to confidently formulate a prevalent theory of the various oscillations that arise within those devices. To advance towards this goal, it is useful to further clarify where the oscillations are generated, what type of structure they possess, or whether they are device- or operating condition-specific. While this objective is certainly more advanced in HETs due to their level of maturity, it is still far in the context of EPTs and, more specifically, MNs. To date, a number of oscillations with similar features have been detected in devices that employ MNs, from coherent, low-frequency oscillations [80–82] to higher-frequency, azimuthally rotating ones [78, 79], though authors identify different actors behind their development and, ultimately, their impact on cross-field anomalous transport.

Additional lines for future development include the design of an experimental setup to clarify ambiguities resulting from the application of the PSD2P technique in some cases. A main limitation of the two-probe coherence technique stems from the inability to tell apart multiple, interacting waves coexisting at nearby frequencies. If there are two or more waves of comparable amplitude at a given f, the phase difference between the two probes will be some form of average resulting from them. Employing a setup with a total of N probes lined in the same direction at non-commensurable distances would be needed to disambiguate among $N-1$ coexisting waves. Alternatively, one could employ a setup in which the probes can move independently in space. However, the technical complexities related to the installation of such setups are not negligible, while also inevitably adding further perturbations within the plasma.

A possible, further broadening of the experimental campaigns carried out in the context of this thesis may include the use of LPs to collect ion saturation current measurements rather than floating potential measurements. Indeed, measurements of ion saturation current can be directly related to the local ion density of the plasma, though the experimental setup is generally less immediate to put in place, necessitating the use of power supplies and shunt resistors, the latter ones that may introduce problems with low-pass filtering. Furthermore, immersing into the plasma probes biased negatively may also introduce a higher level of disturbance on the time-resolved behavior of the plasma.

Another key development which could provide additional insight into the physics observed is further comparison of experimental data with simulations, and vice versa. More specifically, it could also help to address and potentially disambiguate the intrinsic aforementioned limitations of the PSD2P technique. While this comparison is generally easier to perform in the context of HETs due to the substantial body of existing experimental data detailing the oscillations described within this thesis, this task becomes more challenging in the context of MN. Firstly, a simulation code capable of resolving the time-evolution of the plasma expansion in a MN would be required. Given that the oscillations studied in this work occur at relatively low frequencies (in the kHz range), a fully fluid code could suffice. However, the simulation would need to be three-dimensional in order to resolve the azimuthal direction alongside simultaneously resolving the plasma expansion along the nozzle.

Finally, the landscape of data-driven techniques is nowadays extremely wide, and the type of data collected during the development of this thesis may be well suited to the application of a number of various algorithms. This has already been investigated in, e.g., [187, 188]. Future work could rely on alternative, improved techniques, gathering further insight into the characterization of the plasma oscillations studied within this work.

BIBLIOGRAPHY

[1] Ahedo, E., “Plasmas for space propulsion,” *Plasma Physics and Controlled Fusion*, Vol. 53, No. 12, 2011, pp. 124037.

[2] Mazouffre, S., “Electric Propulsion for Satellites and Spacecraft: established Technologies and Novel Approaches,” *Plasma Sources Science and Technology*, Vol. 25, No. 3, 2016, pp. 033002.

[3] Morozov, A., Esipchuk, Y., Tilinin, G., Trofimov, A., Sharov, Y., and G.Y.Shchepkin, “Plasma accelerator with closed electron drift and extended acceleration zone,” *Soviet Physics-Tech. Physics*, Vol. 17, No. 1, 1972, pp. 38–45.

[4] Bugrova, A. I., “Physical processes and characteristics of Stationary Plasma Thrusters with closed electrons drift,” *22nd International Electric Propulsion Conference, Viareggio, Italy*, IEPC 91-079, 1991.

[5] Navarro-Cavallé, J., Wijnen, M., Fajardo, P., Ahedo, E., Gómez, V., Giménez, A., and Ruiz, M., “Development and Characterization of the Helicon Plasma Thruster Prototype HPT05M,” 36^{th} *International Electric Propulsion Conference*, No. IEPC-2019-596, Electric Rocket Propulsion Society, Vienna, Austria, 2019.

[6] Batishchev, O., “Minihelicon plasma thruster,” *IEEE Transactions on Plasma Science*, Vol. 37, No. 8, 2009, pp. 1563–1571.

[7] Takahashi, K., “Helicon–Type Radiofrequency Plasma Thrusters and Magnetic Plasma Nozzles,” *Reviews of Modern Plasma Physics*, Vol. 3, 2019, pp. 3.

[8] Packan, D., Elias, P., Jarrige, J., Merino, M., Sánchez-Villar, A., Ahedo, E., Peyresoubes, G., Holste, K., Klar, P., Bekemans, M., Scalais, T., Bourguignon, E., Zurbach, S., Mares, M., Hooque, A., and Favier, P., “The MINOTOR H2020 project for ECR thruster development,” 35^{th} *International Electric Propulsion Conference*, No. IEPC-2017-547, Electric Rocket Propulsion Society, 2017.

[9] Vialis, T., Jarrige, J., Aanesland, A., and Packan, D., “Direct thrust measurement of an electron cyclotron resonance plasma thruster,” *Journal of Propulsion and Power*, Vol. 34, No. 5, 2018, pp. 1323–1333.

[10] Peterschmitt, S. and Packan, D., “Impact of the Microwave Coupling Structure on an Electron-Cyclotron Resonance Thruster,” *Journal of Propulsion and Power*, Vol. 37, No. 6, 2021, pp. 806–815.

[11] Désangles, V., Packan, D., Jarrige, J., Peterschmitt, S., Dietz, P., Scharmann, S., Holste, K., and Klar, P. J., “ECRA Thruster Advances: 30W and 200W Prototypes Latest Performances,” *Journal of Electric Propulsion*, Vol. 2, No. 1, 2023, pp. 10.

[12] Zhurin, V., Kaufman, H., and Robinson, R., "Physics of closed drift thrusters," *Plasma Sources Science and Technolgy*, Vol. 8, 1999, pp. 1.

[13] Morozov, A. and Savelyev, V., "Fundamentals of Stationary Plasma Thruster Theory," *Reviews of Plasma Physics, Vol. 21*, Kluwer Academic, New York, 2000.

[14] "Beyond NERVA - Hall Effect Thrusters," https://beyondnerva.com/electric-propulsion/hall-effect-thrusters/, Accessed: 2020.

[15] Goebel, D. and Katz, I., *Fundamentals of Electric Propulsion: Ion and Hall Thrusters*, Jet Propulsion Laboratory, Pasadena, CA, 2008.

[16] Jahn, R., *Physics of Electric Propulsion*, Dover, 2006.

[17] Sengupta, A., Brophy, J., Anderson, J., Garner, C., Banks, B., and Groh, K., "An overview of the results from the 30,000 hr life test of deep space 1 flight spare ion engine," *40th AIAA/ASME/SAE/ASEE Joint Propulsion Conference and Exhibit*, 2004, p. 3608.

[18] Kamhawi, H., Soulas, G., Patterson, M., and Frandina, M., "NEXT ion engine 2000 hour wear test plume and erosion results," *AIAA Paper*, Vol. 3792, 2004.

[19] Karadag, B., Cho, S., and Funaki, I., "Thrust performance, propellant ionization, and thruster erosion of an external discharge plasma thruster," *Journal of Applied Physics*, Vol. 123, No. 15, 2018.

[20] Goebel, D. M., Polk, J. E., and Mikellides, I. G., "Ion thruster performance impacts due to cathode wear," *Journal of Propulsion and Power*, Vol. 27, No. 4, 2011, pp. 768–775.

[21] Gallagher, H., "Poisoning of LaB6 cathodes," *Journal of Applied Physics*, Vol. 40, No. 1, 1969, pp. 44–51.

[22] Avdienko, A. and Malev, M., "Poisoning of LaB6 cathodes," *Vacuum*, Vol. 27, No. 10-11, 1977, pp. 583–588.

[23] Bathgate, S., Bilek, M., and Mckenzie, D., "Electrodeless plasma thrusters for spacecraft: a review," *Plasma Science and Technology*, Vol. 19, No. 8, 2017, pp. 083001.

[24] Packan, D., Elias, P.-Q., Jarrige, J., Vialis, T., Correyero, S., Peterschmitt, S., Porto-Hernandez, J., Merino, M., Sánchez-Villar, A., Ahedo, E., Peyresoubes, G., Thorinius, A., Denis, S., Holste, K., Klar, P., Scharmann, S., Zorn, J., Bekemans, M., Scalais, T., Bourguignon, E., Zurbach, S., Azais, P., Habbassi, I., Mares, M., and Hoque, A., "H2020 MINOTOR: Magnetic nozzle electron cyclotron resonance thruster," 36^{th} *International Electric Propulsion Conference*, No. IEPC-2019-875, Electric Rocket Propulsion Society, Vienna, Austria, 2019.

[25] Glover, T., Chang, D., Franklin, R., Squire, J., Jacobson, V., Chavers, D., Carter, M., El-Genk, M., and Bragg, M., "Principal VASIMR results and present objectives," *AIP Conference Proceedings*, Vol. 746, AIP Publishing, Melville, NY, 2005, pp. 976–982.

[26] Chadwick, A. R., *Performance of alternative propellants in an inductive electric propulsion system*, Ph.D. thesis, 2017.

[27] Ahedo, E. and Merino, M., "Two-Dimensional Supersonic Plasma Acceleration in a Magnetic Nozzle," *Physics of Plasmas*, Vol. 17, No. 7, 2010, pp. 073501.

[28] Fruchtman, A., Takahashi, K., Charles, C., and Boswell, R., "A magnetic nozzle calculation of the force on a plasma," *Physics of Plasmas (1994-present)*, Vol. 19, No. 3, 2012, pp. 033507.

[29] Takahashi, K., "Magnetic Nozzle Radiofrequency Plasma Thruster Approaching Twenty Percent Thruster Efficiency," *Scientific Reports*, Vol. 11, No. 1, 2021, pp. 1–12.

[30] Correyero, S., *Physics of plasma plumes accelerated by magnetic nozzles: an experimental and theoretical research*, Ph.D. thesis, Universidad Carlos III de Madrid, Leganés, Spain, 2020.

[31] Taccogna, F. and Dilecce, G., "Non-equilibrium in low-temperature plasmas," *The European Physical Journal D*, Vol. 70, No. 11, 2016, pp. 251.

[32] Charoy, T., Boeuf, J. P., Bourdon, A., Carlsson, J. A., Chabert, P., Cuenot, B., Eremin, D., Garrigues, L., Hara, K., Kaganovich, I. D., Powis, A. T., Smolyakov, A., Sydorenko, D., Tavant, A., Vermorel, O., and Villafana, W., "2D axial-azimuthal particle-in-cell benchmark for low-temperature partially magnetized plasmas," *Plasma Sources Science and Technology*, Vol. 28, No. 10, 2019, pp. 105010.

[33] Sahu, R., Mansour, A., and Hara, K., "Full fluid moment model for low temperature magnetized plasmas," *Physics of Plasmas*, Vol. 27, No. 11, 2020, pp. 113505.

[34] Kolobov, V. and Godyak, V., "Electron kinetics in low-temperature plasmas," *Physics of Plasmas*, Vol. 26, No. 6, 2019.

[35] Koshkarov, O., Smolyakov, A., Raitses, Y., and Kaganovich, I., "Self-organization, structures, and anomalous transport in turbulent partially magnetized plasmas with crossed electric and magnetic fields," *Physical review letters*, Vol. 122, No. 18, 2019, pp. 185001.

[36] Kaganovich, I. D., Smolyakov, A., Raitses, Y., Ahedo, E., Mikellides, I. G., Jorns, B., Taccogna, F., Gueroult, R., Tsikata, S., Bourdon, A., Boeuf, J.-P., Keidar, M., Powis, A. T., Merino, M., Cappelli, M., Hara, K., Carlsson, J. A., Fisch, N. J.,

Chabert, P., Schweigert, I., Lafleur, T., Matyash, K., Khrabrov, A. V., Boswell, R. W., and Fruchtman, A., “Perspectives on Physics of ExB Discharges Relevant to Plasma Propulsion and Similar Technologies,” *Physics of Plasmas*, Vol. 27, No. 12, 2020, pp. 120601.

[37] Adam, J., Herón, A., and Laval, G., “Study of stationary plasma thrusters using two-dimensional fully kinetic simulations,” *Physics of Plasmas*, Vol. 11, 2004, pp. 295–305.

[38] Anders, A., Ni, P., and Rauch, A., “Drifting localization of ionization runaway: Unraveling the nature of anomalous transport in high power impulse magnetron sputtering,” *Journal of Applied Physics*, Vol. 111, No. 5, 2012.

[39] Cavalier, J., Lemoine, N., Bonhomme, G., Tsikata, S., Honoré, C., and Grésillon, D., “Hall thruster plasma fluctuations identified as the ExB electron drift instability: Modeling and fitting on experimental data,” *PoP*, Vol. 20, No. 8, 2013, pp. 082107.

[40] Sekerak, M. J., Longmier, B. W., Gallimore, A. D., Brown, D. L., Hofer, R. R., and Polk, J. E., “Azimuthal spoke propagation in Hall effect thrusters,” *IEEE Transactions on Plasma Science*, Vol. 43, No. 1, 2014, pp. 72–85.

[41] Tsikata, S. and Minea, T., “Modulated electron cyclotron drift instability in a high-power pulsed magnetron discharge,” *Physical Review Letters*, Vol. 114, 2015, pp. 185001.

[42] Carlsson, J., Kaganovich, I., Powis, A., Raitses, Y., Romadanov, I., and Smolyakov, A., “Particle-in-cell simulations of anomalous transport in a Penning discharge,” *Physics of Plasmas*, Vol. 25, No. 6, 2018.

[43] Boeuf, J.-P. and Smolyakov, A., “Physics and instabilities of low-temperature E x B plasmas for spacecraft propulsion and other applications,” *Physics of Plasmas*, Vol. 30, No. 5, 2023.

[44] Davidson, R. and Krall, N., “Anomalous transport in high-temperature plasmas with applications to solenoidal fusion systems,” *Nuclear Fusion*, Vol. 17, No. 6, 1977, pp. 1313.

[45] Burin, M., Tynan, G., Antar, G., Crocker, N., and Holland, C., “On the transition to drift turbulence in a magnetized plasma column,” *Physics of Plasmas*, Vol. 12, No. 5, 2005.

[46] Diamond, P. H., Itoh, S., Itoh, K., and Hahm, T., “Zonal flows in plasmaa review,” *Plasma Physics and Controlled Fusion*, Vol. 47, No. 5, 2005, pp. R35.

[47] Light, M., Chen, F. F., and Colestock, P., “Low frequency electrostatic instability in a helicon plasma,” *Physics of Plasmas*, Vol. 8, No. 10, 2001, pp. 4675–4689.

[48] Tynan, G., Burin, M., Holland, C., Antar, G., and Diamond, P., “Radially sheared azimuthal flows and turbulent transport in a cylindrical helicon plasma device,” *Plasma physics and controlled fusion*, Vol. 46, No. 5A, 2004, pp. A373.

[49] Yan, Z., Tynan, G., Holland, C., Xu, M., Müller, S., and Yu, J., “Shear flow and drift wave turbulence dynamics in a cylindrical plasma device,” *Physics of Plasmas*, Vol. 17, No. 3, 2010.

[50] Thakur, S. C., Brandt, C., Cui, L., Gosselin, J., Light, A., and Tynan, G., “Multi-instability plasma dynamics during the route to fully developed turbulence in a helicon plasma,” *Plasma Sources Science and Technology*, Vol. 23, No. 4, 2014, pp. 044006.

[51] Porkolab, M., “Parametric instabilities in a magnetic field and possible applications to heating of plasmas,” *Nuclear fusion*, Vol. 12, No. 3, 1972, pp. 329.

[52] Akhiezer, A., Mikhailenko, V., and Stepanov, K., “Ion-sound parametric turbulence and anomalous electron heating with application to helicon plasma sources,” *Physics Letters A*, Vol. 245, No. 1-2, 1998, pp. 117–122.

[53] Virko, V., Kirichenko, G., and Shamrai, K., “Parametric ion-acoustic turbulence in a helicon discharge,” *Plasma Sources Science and Technology*, Vol. 12, No. 2, 2003, pp. 217.

[54] Kline, J., Balkey, M., Keiter, P., Scime, E., Keesee, A., Sun, X., Hardin, R., Compton, C., Boivin, R., and Zintl, M., “Ion dynamics in helicon sources,” *Physics of Plasmas*, Vol. 10, 2003, pp. 2127.

[55] Aliev, Y. M. and Krämer, M., “Parametric instabilities in helicon-produced plasmas,” *Physics of plasmas*, Vol. 12, No. 7, 2005.

[56] Lorenz, B., Krämer, M., Selenin, V., and Aliev, Y. M., “Excitation of short-scale fluctuations by parametric decay of helicon waves into ion–sound and Trivelpiece–Gould waves,” *Plasma Sources Science and Technology*, Vol. 14, No. 3, 2005, pp. 623.

[57] Horton, W., “Drift waves and transport,” *Reviews of Modern Physics*, Vol. 71, No. 3, 1999, pp. 735.

[58] Garbet, X., “Turbulence in fusion plasmas: key issues and impact on transport modelling,” *Plasma physics and controlled fusion*, Vol. 43, No. 12A, 2001, pp. A251.

[59] Boeuf, J., “Tutorial: Physics and modeling of Hall thrusters,” *J. Applied Physics*, Vol. 121, No. 1, 2017, pp. 011101.

[60] Little, J. and Choueiri, E., “Critical Condition for Plasma Confinement in the Source of a Magnetic Nozzle Flow,” *IEEE Transactions on Plasma Science*, Vol. 43, No. 1, 2014, pp. 277–286.

[61] Moses, R., Gerwin, R., and Schoenberg, K., “Resistive plasma detachment in nozzle based coaxial thrusters,” *Proceedings Ninth Symposium on Space Nuclear Power Systems, Albuquerque, New Mexico, 1992*, AIP Conference Proceedings No. 246, 1992, pp. 1293–1303.

[62] Olsen, C. S., *Experimental characterization of plasma detachment from magnetic nozzles*, Rice University, 2013.

[63] Little, J. M. and Choueiri, E. Y., “Electron Demagnetization in a Magnetically Expanding Plasma,” *Physical review letters*, Vol. 123, No. 14, 2019, pp. 145001.

[64] Choueiri, E., “Plasma oscillations in Hall thrusters,” *Physics of Plasmas*, Vol. 8, No. 4, 2001, pp. 1411–1426.

[65] Fife, J., Martínez-Sánchez, M., and Szabo, J., “A Numerical Study of Low-Frequency Discharge Oscillations in Hall Thrusters,” *33rd Joint Propulsion Conference, Seattle, WA*, AIAA 97-3052, 1997.

[66] Boeuf, J. and Garrigues, L., “Low frequency oscillations in a stationary plasma thruster,” *J. Applied Physics*, Vol. 84, No. 7, 1998, pp. 3541–3554.

[67] Albarede, L., Mazouffre, S., Bouchoule, A., and Dudeck, M., “Low-frequency electron dynamics in the near field of a Hall effect thruster,” *Physics of Plasmas*, Vol. 13, 2006, pp. 063505.

[68] Barral, S. and Ahedo, E., “Low-frequency model of breathing oscillations in Hall discharges,” *Physical Review E*, Vol. 79, 2009, pp. 046401.

[69] Petronio, F., Alvarez Laguna, A., Bourdon, A., and Chabert, P., “Study of the breathing mode development in Hall thrusters using hybrid simulations,” *Journal of Applied Physics*, Vol. 135, No. 7, 2024.

[70] Hara, K., Sekerak, M. J., Boyd, I. D., and Gallimore, A. D., “Perturbation analysis of ionization oscillations in Hall effect thrusters,” *Physics of Plasmas*, Vol. 21, No. 12, 2014, pp. 122103.

[71] Bareilles, J., Hagelaar, G., Garrigues, L., Boniface, C., Boeuf, J., and Gascon, N., “Critical assessment of a two-dimensional hybrid Hall thruster model: Comparisons with experiments,” *Physics of Plasmas*, Vol. 11, No. 6, 2004, pp. 3035–3046.

[72] Barral, S., Makowski, K., Peradzynski, Z., and Dudeck, M., “Transit-time instability in Hall thrusters,” *Physics of Plasmas*, Vol. 12, 2005, pp. 073504.

[73] Kurzyna, J., Mazouffre, S., Lazurenko, A., Albarède, L., Bonhomme, G., Makowski, K., Dudeck, M., and Peradzyński, Z., “Spectral analysis of Hall-effect thruster plasma oscillations based on the empirical mode decomposition,” *Physics of Plasmas*, Vol. 12, 2005, pp. 123506.

[74] Lazurenko, A., de Wit, T., Cavoit, C., Krasnoselskikh, V., Bouchoule, A., and Dudeck, M., “Determination of the electron anomalous mobility through measurements of turbulent magnetic field in Hall thrusters,” *Physics of Plasmas*, Vol. 14, No. 3, 2007, pp. 033504.

[75] Charoy, T., Lafleur, T., Alvarez-Laguna, A., Bourdon, A., and Chabert, P., “The interaction between ion transit-time and electron drift instabilities and their effect on anomalous electron transport in Hall thrusters,” *Plasma Sources Science and Technology*, 2021.

[76] Gerwin, R. A., “Integrity of the plasma magnetic nozzle,” Tech. rep., NASA/TP2009-213439, 2009.

[77] Olsen, C., Ballenger, M., Carter, M., Chang Diaz, F., Giambusso, M., Glover, T., Ilin, A., Squire, J., Longmier, B., Bering, E., and Cloutier, P., “Investigation of Plasma Detachment From a Magnetic Nozzle in the Plume of the VX-200 Magnetoplasma Thruster,” *Plasma Science, IEEE Transactions on*, Vol. 43, No. 1, 2015, pp. 252–268.

[78] Hepner, S., Wachs, B., and Jorns, B., “Wave-driven non-classical electron transport in a low temperature magnetically expanding plasma,” *Applied Physics Letters*, Vol. 116, No. 26, 2020, pp. 263502.

[79] Takahashi, K., Charles, C., and Boswell, R. W., “Wave-driven electron inward transport in a magnetic nozzle,” *Scientific reports*, Vol. 12, No. 1, 2022, pp. 20137.

[80] Aanesland, A., Charles, C., Lieberman, M., and Boswell, R., “Upstream ionization instability associated with a current-free double layer,” *Physical review letters*, Vol. 97, No. 7, 2006, pp. 075003.

[81] Hepner, S. T., *The influence of instabilities on the electron dynamics of a Magnetic Nozzle*, Ph.D. thesis, Department of Aerospace Engineering, The University of Michigan, Ann Arbor, MI, 2022.

[82] Doyle, S. J., Bennet, A., Tsifakis, D., Dedrick, J. P., Boswell, R. W., and Charles, C., “Characterization and control of an ion-acoustic plasma instability downstream of a diverging magnetic nozzle,” *Frontiers in Physics*, Vol. 8, 2020, pp. 24.

[83] Singh, N., Rao, S., and Ranganath, P., “Waves generated in the plasma plume of helicon magnetic nozzle,” *Physics of Plasmas*, Vol. 20, No. 3, 2013.

[84] Lorente, L., Vega, J., and Velazquez, A., “Compression of aerodynamic databases using high-order singular value decomposition,” *Aerospace Science and Technology*, Vol. 14, No. 3, 2010, pp. 168–177.

[85] Lav, C., Sandberg, R. D., and Philip, J., "A framework to develop data-driven turbulence models for flows with organised unsteadiness," *Journal of Computational Physics*, Vol. 383, 2019, pp. 148–165.

[86] Holmes, P., Lumley, J. L., Berkooz, G., and Rowley, C. W., *Turbulence, coherent structures, dynamical systems and symmetry*, Cambridge University Press, 2012.

[87] Taira, K., Brunton, S. L., Dawson, S. T. M., Rowley, C. W., Colonius, T., McKeon, B. J., Schmidt, O. T., Gordeyev, S., Theofilis, V., and Ukeiley, L. S., "Modal analysis of fluid flows: an overview," *AIAA Journal*, Vol. 55, 2017, pp. 4013–4041.

[88] Hijazi, S., Stabile, G., Mola, A., and Rozza, G., "Data-driven POD-Galerkin reduced order model for turbulent flows," *Journal of Computational Physics*, Vol. 416, 2020, pp. 109513.

[89] van Milligen, B. P., Sánchez, E., Alonso, A., Pedrosa, M. A., Hidalgo, C., Martín de Aguilera, A., and López Fraguas, A., "The use of the biorthogonal decomposition for the identification of zonal flows at TJ-II," *Plasma Phys. Control. Fusion*, Vol. 57, 2015, pp. 025005.

[90] Taylor, R., Kutz, J. N., Morgan, K., and Nelson, B. A., "Dynamic mode decomposition for plasma diagnostics and validation," *Review of Scientific Instruments*, Vol. 89, 2018, pp. 053501.

[91] Jourdain, G., Eriksson, L.-E., Kim, S. H., and Sohn, C. H., "Application of dynamic mode decomposition to acoustic-modes identification and damping in a 3-dimensional chamber with baffled injectors," *Journal of Sound and Vibration*, Vol. 332, No. 18, 2013, pp. 4308–4323.

[92] Wang, J., Li, S., Chen, H., Yuan, Y., and Huang, Y., "Data-driven model predictive control for building climate control: Three case studies on different buildings," *Building and Environment*, Vol. 160, 2019, pp. 106204.

[93] Smarra, F., Jain, A., De Rubeis, T., Ambrosini, D., DInnocenzo, A., and Mangharam, R., "Data-driven model predictive control using random forests for building energy optimization and climate control," *Applied energy*, Vol. 226, 2018, pp. 1252–1272.

[94] Groun, N., Villalba-Orero, M., Lara-Pezzi, E., Valero, E., Garicano-Mena, J., and Le Clainche, S., "Higher order dynamic mode decomposition: From fluid dynamics to heart disease analysis," *Computers in Biology and Medicine*, Vol. 144, 2022, pp. 105384.

[95] Buczak, A. L., Koshute, P. T., Babin, S. M., Feighner, B. H., and Lewis, S. H., "A data-driven epidemiological prediction method for dengue outbreaks using local and remote sensing data," *BMC medical informatics and decision making*, Vol. 12, No. 1, 2012, pp. 1–20.

[96] Ryait, H., Bermudez-Contreras, E., Harvey, M., Faraji, J., Mirza Agha, B., Gomez-Palacio Schjetnan, A., Gruber, A., Doan, J., Mohajerani, M., Metz, G. A., et al., "Data-driven analyses of motor impairments in animal models of neurological disorders," *PLoS biology*, Vol. 17, No. 11, 2019, pp. e3000516.

[97] Yu, W., Wong, C. Y., Chavez, R., and Jacobs, M. A., "Integrating big data analytics into supply chain finance: The roles of information processing and data-driven culture," *International Journal of Production Economics*, Vol. 236, 2021, pp. 108135.

[98] Lin, E. M., Sun, E. W., and Yu, M.-T., "Behavioral data-driven analysis with Bayesian method for risk management of financial services," *International Journal of Production Economics*, Vol. 228, 2020, pp. 107737.

[99] Brunton, S. L. and Kutz, J. N., *Data-driven science and engineering: Machine learning, dynamical systems, and control*, Cambridge University Press, 2022.

[100] Rosolia, U., Zhang, X., and Borrelli, F., "Data-driven predictive control for autonomous systems," *Annual Review of Control, Robotics, and Autonomous Systems*, Vol. 1, 2018, pp. 259–286.

[101] Terragni, F., Bonilla, L., and Vega, J. M., "Uncovering spatiotemporal patterns in semiconductor superlattices by efficient data processing tools," *Physical Review E*, Vol. 104, No. 3, 2021, pp. 035303.

[102] Rapún, M.-L., Terragni, F., and Vega, J., "Adaptive sampling and modal expansions in pattern-forming systems," *Advances in Computational Mathematics*, Vol. 47, No. 4, 2021, pp. 48.

[103] Dahl, P. N., Kimber, A. M., and Jorns, B., "Data-driven scaling law for the extractor current of a capillary electrospray," *AIAA Propulsion and Energy 2019 Forum*, 2019, p. 3901.

[104] Jorns, B., "Predictive, data-driven model for the anomalous electron collision frequency in a Hall effect thruster," *Plasma Sources Science and Technology*, Vol. 27, No. 10, 2018, pp. 104007.

[105] Woods, J. M., Sercel, C. L., Gill, T. M., Viges, E., and Jorns, B. A., "Data-driven approach to modeling and development of a 30 kW field-reversed configuration thruster," *36th International Electric Propulsion Conference*, 2019, pp. 2019–717.

[106] Kleiber, R., Borchardt, M., Könies, A., and Slaby, C., "Modern methods of signal processing applied to gyrokinetic simulations," *Plasma Physics and Controlled Fusion*, Vol. 63, No. 3, 2021, pp. 035017.

[107] Xu, L., Eremin, D., and Brinkmann, R. P., "Direct evidence of gradient drift instability being the origin of a rotating spoke in a crossed field plasma," *Plasma Sources Science and Technology*, Vol. 30, No. 7, 2021, pp. 075013.

[108] Bayón-Buján, B. and Merino, M., "Data-driven sparse modeling of oscillations in plasma space propulsion," *Machine Learning Science and Technology (under review)*, 2024.

[109] Lumley, J. L., "The structure of inhomogeneous turbulent flows," *Atmospheric turbulence and radio wave propagation*, 1967, pp. 166–178.

[110] Sirovich, L., "Turbulence and the dynamics of coherent structures," *Q. Appl. Math.*, Vol. XLV, 1987, pp. 561–590.

[111] Berkooz, G., Holmes, P., and Lumley, J. L., "The proper orthogonal decomposition in the analysis of turbulent flows," *Ann. Rev. Fluid Mech.*, Vol. 25, 1993, pp. 539–575.

[112] Chatterjee, A., "An introduction to the proper orthogonal decomposition," *Current Science*, Vol. 78, 2000, pp. 808–817.

[113] Schmid, P. J., "Dynamic mode decomposition of numerical and experimental data," *Journal of Fluid Mechanics*, Vol. 656, 2010, pp. 5–28.

[114] Kutz, J. N., Brunton, S. L., Brunton, B. W., and Proctor, J. L., *Dynamic mode decomposition: Data-driven modeling of complex systems*, SIAM, 2016.

[115] Le Clainche, S. and Vega, J. M., "Higher order dynamic mode decomposition," *SIAM J. Appl. Dyn. Syst.*, Vol. 16, 2017, pp. 882–925.

[116] Tu, J. H., *Dynamic mode decomposition: Theory and applications*, Ph.D. thesis, Princeton University, 2013.

[117] Désangles, V., Shcherbanev, S., Charoy, T., Clément, N., Deltel, C., Richard, P., Vincent, S., Chabert, P., and Bourdon, A., "Fast camera analysis of plasma instabilities in Hall effect thrusters using a POD method under different operating regimes," *Atmosphere*, Vol. 11, 2020, pp. 518.

[118] Perales-Díaz, J., Domínguez-Vázquez, A., Fajardo, P., and Ahedo, E., "Simulations of driven breathing modes of a magnetically shielded Hall thruster," *Plasma Sources Science and Technology*, Vol. 32, No. 7, 2023, pp. 075011.

[119] Petronio, F., *Plasma instabilities in Hall Thrusters: a theoretical and numerical study*, Ph.D. thesis, Institut Polytechnique de Paris, 2023.

[120] Faraji, F., Reza, M., Knoll, A., and Kutz, J. N., "Dynamic mode decomposition for data-driven analysis and reduced-order modeling of E$\times$ B plasmas: I. Extraction of spatiotemporally coherent patterns," *Journal of Physics D: Applied Physics*, Vol. 57, No. 6, 2023, pp. 065201.

[121] Faraji, F., Reza, M., Knoll, A., and Kutz, J. N., "Dynamic mode decomposition for data-driven analysis and reduced-order modeling of E× B plasmas: II. Dynamics forecasting," *Journal of Physics D: Applied Physics*, Vol. 57, No. 6, 2023, pp. 065202.

[122] Le Clainche, S., Vega, J. M., and Soria, J., "Higher order dynamic mode decomposition of noisy experimental data: The flow structure of a zero-net-mass-flux jet," *Experimental Thermal and Fluid Science*, Vol. 88, 2017, pp. 336–353.

[123] Vega, J. M. and Le Clainche, S., *Higher order dynamic mode decomposition and its applications*, Academic Press, 2020.

[124] Mazouffre, S., Bourgeois, G., Dannenmayer, K., and Lejeune, A., "Ionization and acceleration processes in a small, variable channel width, permanent-magnet Hall thruster," *J. Phys. D: Appl. Phys.*, Vol. 45, 2012, pp. 185203.

[125] Young, C., Fabris, A. L., MacDonald-Tenenbaum, N., Hargus, W., and Cappelli, M., "Time-resolved laser-induced fluorescence diagnostics for electric propulsion and their application to breathing mode dynamics," *Plasma Sources Science and Technology*, Vol. 27, No. 9, 2018, pp. 094004.

[126] Conway, G. and Elliott, J., "Digital signal processing techniques for plasma dispersion curve measurements," *Journal of Physics E: Scientific Instruments*, Vol. 20, No. 11, 1987, pp. 1341.

[127] Beall, J., Kim, Y., and Powers, E., "Estimation of wavenumber and frequency spectra using fixed probe pairs," *Journal of Applied Physics*, Vol. 53, No. 6, 1982, pp. 3933–3940.

[128] Petronio, F., Charoy, T., Alvarez Laguna, A., Bourdon, A., and Chabert, P., "Two-dimensional effects on electrostatic instabilities in Hall thrusters. II. Comparison of particle-in-cell simulation results with linear theory dispersion relations," *Physics of Plasmas*, Vol. 30, No. 1, 2023.

[129] Petronio, F., Charoy, T., Alvarez Laguna, A., Bourdon, A., and Chabert, P., "Two-dimensional effects on electrostatic instabilities in Hall thrusters. I. Insights from particle-in-cell simulations and two-point power spectral density reconstruction techniques," *Physics of Plasmas*, Vol. 30, No. 1, 2023.

[130] Carter, G. C., "Coherence and time delay estimation," *Proceedings of the IEEE*, Vol. 75, No. 2, 1987, pp. 236–255.

[131] Kim, Y. C. and Powers, E. J., "Digital bispectral analysis of self-excited fluctuation spectra," *Physics of Fluids*, Vol. 21, 1978, pp. 1452–1453.

[132] Takahashi, K., “Thirty Percent Conversion Efficiency from Radiofrequency Power to Thrust Energy in a Magnetic Nozzle Plasma Thruster,” *Scientific Reports*, Vol. 12, 2022, pp. 18618.

[133] Achermann, P. and Borbély, A. A., “Coherence analysis of the human sleep electroencephalogram,” *Neuroscience*, Vol. 85, No. 4, 1998, pp. 1195–1208.

[134] Gee, K. L., Atchley, A. A., Falco, L. E., Shepherd, M. R., Ukeiley, L. S., Jansen, B. J., and Seiner, J. M., “Bicoherence analysis of model-scale jet noise,” *The Journal of the Acoustical Society of America*, Vol. 128, No. 5, 2010, pp. EL211–EL216.

[135] Domínguez-Vázquez, A., Pérez-Grande, D., Fajardo, P., and Ahedo, E., “NOMADS: Development of a versatile plasma discharge simulation platform for electric propulsion,” *Space Propulsion Conference 2016*, No. paper 2016-3124869, Association Aéronautique et Astronautique de France, Rome, Italy, May 2-6, 2016.

[136] Domínguez-Vázquez, A., Cichocki, F., Merino, M., Fajardo, P., and Ahedo, E., “2D and 3D Hybrid PIC/Fluid Modelling of Electric Thruster Plumes,” 35^{th} *International Electric Propulsion Conference*, No. IEPC-2017-209, Electric Rocket Propulsion Society, Atlanta, GA, 2017.

[137] Cichocki, F., Domínguez-Vázquez, A., Merino, M., and Ahedo, E., “Hybrid 3D model for the interaction of plasma thruster plumes with nearby objects,” *Plasma Sources Science and Technology*, Vol. 26, No. 12, 2017, pp. 125008.

[138] Domínguez-Vázquez, A., Cichocki, F., Merino, M., Fajardo, P., and Ahedo, E., “Axisymmetric plasma plume characterization with 2D and 3D particle codes,” *Plasma Sources Science and Technology*, Vol. 27, No. 10, 2018, pp. 104009.

[139] Domínguez-Vázquez, A., *Axisymmetric simulation codes for Hall effect thrusters and plasma plumes*, Ph.D. thesis, Universidad Carlos III de Madrid, Leganés, Spain, 2019.

[140] Domínguez-Vázquez, A., Zhou, J., Fajardo, P., and Ahedo, E., “Analysis of the plasma discharge in a Hall thruster via a hybrid 2D code,” 36^{th} *International Electric Propulsion Conference*, No. IEPC-2019-579, Electric Rocket Propulsion Society, Vienna, Austria, 2019.

[141] Biagi, S.F., “Cross sections extracted from PROGRAM MAGBOLTZ, VERSION 7.1 JUNE 2004,” June 2004, [Online; accessed 5-July-2021].

[142] Mitchner, M. and Kruger Jr., C., *Partially ionized gases*, John Wiley and Sons, Hoboken, NJ, 1973.

[143] Fife, J. M., *Hybrid-PIC modeling and electrostatic probe survey of Hall thrusters*, Ph.D. thesis, Massachusetts Institute of Technology, 1998.

[144] Parra, F. I., Ahedo, E., Fife, J. M., and Martínez-Sánchez, M., "A two-dimensional hybrid model of the Hall thruster discharge," *Journal of Applied Physics*, Vol. 100, No. 2, 2006, pp. 023304.

[145] Ahedo, E., Gallardo, J., and Martínez-Sánchez, M., "Effects of the radial-plasma wall interaction on the axial Hall thruster discharge," *Physics of Plasmas*, Vol. 10, No. 8, 2003, pp. 3397–3409.

[146] Sankovic, J. M., Hamley, J. A., and Hang, T. W., "Performance evaluation of the Russian SPT-100 thruster at NASA LeRC," *23rd International Electric Propulsion Conference*, IEPC 93-094, Seattle, WA, 1993.

[147] Mazouffre, S., Echegut, P., and Dudeck, M., "A calibrated infrared imaging study on the steady state thermal behaviour of Hall effect thrusters," *Plasma Sources Science and Technology*, Vol. 16, No. 1, 2006, pp. 13.

[148] Hagelaar, G., Bareilles, J., Garrigues, L., and Boeuf, J., "Role of anomalous electron transport in a stationary plasma thruster simulation," *Journal of Applied Physics*, Vol. 93, No. 1, 2003, pp. 67–75.

[149] Domínguez-Vázquez, A., Zhou, J., Sevillano-González, A., Fajardo, P., and Ahedo, E., "Analysis of the electron downstream boundary conditions in a 2D hybrid code for Hall thrusters," 37^{th} *International Electric Propulsion Conference*, No. IEPC-2022-338, Electric Rocket Propulsion Society, Boston, MA, June 19-23, 2022.

[150] Bayón-Buján, B., Bello-Benítez, E., Zhou, J., and Merino, M., "Data-driven analysis of a 2D-ExB kinetic simulation relevant to Hall thruster discharges," 38^{th} *International Electric Propulsion Conference*, No. IEPC-2024-640, Electric Rocket Propulsion Society, Toulouse, France, June 23-28, 2024.

[151] Ahedo, E. and Pablo, V., "Combined effects of electron partial thermalization and secondary emission in Hall thruster discharges," *Physics of Plasmas*, Vol. 14, 2007, pp. 083501.

[152] Maqueda, I., Escobar, D., and Ahedo, E., "Advances on a Hall thruster hybrid code," *30th International Electric Propulsion Conference, Florence, Italy*, IEPC 2007-066, 2007.

[153] Golub, G. H. and van Loan, G. T., *Matrix computations*, John Hopkins Univ. Press, 1996.

[154] Brunton, S. L., Brunton, B. W., Proctor, J. L., and Kutz, J. N., "Koopman invariant subspaces and finite linear representations of nonlinear dynamical systems for control," *PLoS ONE*, Vol. 11, 2016, pp. 0150171.

[155] Le Clainche, S. and Vega, J. M., Vol. https://github.com/LeClaincheVega/HODMD, 2017.

[156] Jovanović, M. R., Schmid, P. J., and Nichols, J. W., "Sparsity-promoting dynamic mode decomposition," *Physics of Fluids*, Vol. 26, No. 2, 2014, pp. 024103.

[157] Scharfe, M., Gascon, N., Cappelli, M., and Fernandez, E., "Comparison of hybrid Hall thruster model to experimental measurements," *Physics of Plasmas*, Vol. 13, 2006, pp. 083505.

[158] Wang, C., Wei, L., and Yu, D., "A Basic Predator-Prey Type Model for Low Frequency Discharge Oscilations in Hall Thrusters," *Contributions to Plasma Physics*, Vol. 51, No. 10, 2011, pp. 981–988.

[159] Choueiri, E. and Ziemer, J., "Quasi-steady magnetoplasmadynamic thruster performance database," *Journal of Propulsion and Power*, Vol. 17, No. 5, 2001, pp. 967–976.

[160] Garrigues, L., Heron, A., Adam, J., and Boeuf, J., "Hybrid and particle-in-cell models of a stationary plasma thruster," *Plasma Sources Science and Technology*, Vol. 9, 2000, pp. 219.

[161] Bouchoule, A., Philippe-Kadlec, C., Prioul, M., Darnon, F., Lyszyk, M., Magne, L., Pagnon, D., Roche, S., Touzeau, M., B'echu, S., et al., "Transient phenomena in closed electron drift plasma thrusters: insights obtained in a French cooperative program," *Plasma Sources Science and Technology*, Vol. 10, 2001, pp. 364.

[162] Vinci, A. E., Mazouffre, S., Gómez, V., Fajardo, P., and Navarro-Cavallé, J., "Laser-induced fluorescence spectroscopy on xenon atoms and ions in the magnetic nozzle of a helicon plasma thruster," *Plasma Sources Science and Technology*, Vol. 31, No. 9, 2022, pp. 095007.

[163] Lobbia, R. B. and Beal, B. E., "Recommended Practice for Use of Langmuir Probes in Electric Propulsion Testing," *Journal of Propulsion and Power*, Vol. 33, No. 3, 2017, pp. 566–581.

[164] Thompson, R. O., "Coherence significance levels," *Journal of the Atmospheric Sciences*, Vol. 36, No. 10, 1979, pp. 2020–2021.

[165] Mardia, K. V., Jupp, P. E., and Mardia, K., *Directional statistics*, Vol. 2, Wiley Online Library, 2000.

[166] Kim, Y. C. and Powers, E. J., "Digital Bispectral Analysis and Its Applications to Nonlinear Wave Interactions," *IEEE Transactions on Plasma Science*, Vol. 7, 1979, pp. 120–131.

[167] Elgar, S. and Guza, R., "Statistics of bicoherence," *IEEE Transactions on Acoustics, Speech, and Signal Processing*, Vol. 36, No. 10, 1988, pp. 1667–1668.

[168] Jiménez, P., Zhou, J., Navarro-Cavallé, J., Fajardo, P., Merino, M., and Ahedo, E., "Analysis of a cusped helicon plasma thruster discharge," *Plasma Sources Science and Technology*, Vol. 32, No. 10, 2023, pp. 105013.

[169] Lee, P.-W., Lee, S.-W., and Chang, H.-Y., "Undriven periodic plasma oscillation in electron cyclotron resonance Ar plasma," *Applied physics letters*, Vol. 69, No. 14, 1996, pp. 2024–2026.

[170] Goebel, D. M., Jameson, K. K., Katz, I., and Mikellides, I. G., "Potential fluctuations and energetic ion production in hollow cathode discharges," *Physics of Plasmas*, Vol. 14, No. 10, 2007.

[171] Georgin, M. P., Jorns, B. A., and Gallimore, A. D., "Correlation of ion acoustic turbulence with self-organization in a low-temperature plasma," *Physics of Plasmas*, Vol. 26, No. 8, 2019.

[172] Maddaloni, D., Domínguez-Vázquez, A., Terragni, F., and Merino, M., "Data-driven analysis of oscillations in Hall thruster simulations," *Plasma Sources Science and Technology*, Vol. 31, No. 4, 4 2022, pp. 045026.

[173] Giannetti, V., Saravia, M. M., Leporini, L., Camarri, S., and Andreussi, T., "Numerical and experimental investigation of longitudinal oscillations in Hall thrusters," *Aerospace*, Vol. 8, No. 6, 2021, pp. 148.

[174] Sakawa, Y., Joshi, C., Kaw, P., Chen, F., and Jain, V., "Excitation of the modified Simon–Hoh instability in an electron beam produced plasma," *Physics of Fluids B: Plasma Physics*, Vol. 5, No. 6, 1993, pp. 1681–1694.

[175] Tao, Y., R.W.Conn, Schmitz, L., and Tynan, G., "Ion flow in a strongly sheared electric field," *Physics of Fluids B*, Vol. 5, 1993, pp. 344–349.

[176] Carter, M., Baity Jr, F., Barber, G., Goulding, R., Mori, Y., Sparks, D., White, K., Jaeger, E., Chang-Diaz, F., and Squire, J., "Comparing experiments with modeling for light ion helicon plasma sources," *Physics of Plasmas*, Vol. 9, 2002, pp. 5097.

[177] Goldston, R. and Rutherford, P., *Introduction to Plasma Physics*, Institute of Physics Publishing, Bristol, 1995.

[178] Stix, T. H., *Waves in plasmas*, Springer Science & Business Media, 1992.

[179] Boni, F., Jarrige, J., Désangles, V., and Minea, T., "The curling probe: A numerical and experimental study. Application to the electron density measurements in an ECR plasma thruster," *Review of Scientific Instruments*, Vol. 92, No. 3, 2021, pp. 033507.

[180] Boni, F., Désangles, V., and Jarrige, J., "A sheath correction method for electron density measurements with the microwave resonant curling probe," *Plasma Sources Science and Technology*, Vol. 32, No. 9, 2023, pp. 095018.

[181] Vincent, S., Dolique, V., and Plihon, N., "Nonlinear interactions of ion acoustic waves explored using fast imaging decompositions," *Physics of Plasmas*, Vol. 30, No. 1, 2023.

[182] Correyero, S., Jarrige, J., Packan, D., and Ahedo, E., "Plasma beam characterization along the magnetic nozzle of an ECR thruster," *Plasma Sources Science and Technology*, Vol. 28, No. 9, 2019, pp. 095004.

[183] Boni, F., *Development of a microwave plasma diagnostic applied to electric propulsion systems*, Ph.D. thesis, Université Paris-Saclay, 2022.

[184] Welch, P., "The use of fast Fourier transform for the estimation of power spectra: a method based on time averaging over short, modified periodograms," *IEEE Transactions on audio and electroacoustics*, Vol. 15, No. 2, 1967, pp. 70–73.

[185] Dale, E. T. and Jorns, B. A., "Experimental characterization of Hall thruster breathing mode dynamics," *Journal of Applied Physics*, Vol. 130, No. 13, 2021, pp. 133302.

[186] Maddaloni, D., Navarro-Cavallé, J., Merino, M., and Terragni, F., "Experimental investigation of oscillations in a magnetic nozzle," 35^{th} *International Conference on Plasmas and Ionized Gases*, Egmond aan Zee, The Netherlands, July 914, 2023.

[187] Puerto-Sánchez, C., *Non-linear Data Analysis applied to Plasma Space Propulsion*, Bachelor's thesis, Universidad Carlos III de Madrid, 2021.

[188] Bajón-Buján', B., *Sparse Regression for the Breathing Mode Instability: Extracting Governing Equations from Hall Effect Thrusters Simulation Data*, Master's thesis, Universidad Carlos III de Madrid, 2023.